N 71 10405
CR 111099

Report J-910900-1

Results of Experiments to Simulate
Radiant Heating of Propellant in a
Nuclear Light Bulb Engine Using a
D-C Arc Radiant Energy Source

Contract SNPC-70

UA
U
A
UNITED AIRCRAFT CORPORATION

United Aircraft Research Laboratories

EAST HARTFORD, CONNECTICUT

United Aircraft Research Laboratories

U
UNITED AIRCRAFT CORPORATION
A

EAST HARTFORD, CONNECTICUT

Report J-910900-1

Results of Experiments to Simulate
Radiant Heating of Propellant in a
Nuclear Light Bulb Engine Using a
D-C Arc Radiant Energy Source

Contract SNPC-70

REPORTED BY *John F Klein*
John F. Klein

Ward C. Roman
Ward C. Roman

APPROVED BY *James W. Clark*
James W. Clark, Chief
Fluid and Systems Dynamics

DATE September 1970

NO. OF PAGES __99__   COPY NO. __26__

FOREWORD

An exploratory experimental and theoretical investigation of gaseous nuclear rocket technology is being conducted by the United Aircraft Research Laboratories under Contract SNPC-70 with the joint AEC-NASA Space Nuclear Propulsion Office. The Technical Supervisor of the Contract for NASA is Captain C. E. Franklin (USAF). Results of portions of the investigation conducted during the period between September 16, 1969 and September 15, 1970 are described in the following eight reports (including the present report) which comprise the required first Interim Summary Technical Report under the Contract:

1. Klein, J. F. and W. C. Roman: Results of Experiments to Simulate Radiant Heating of Propellant in a Nuclear Light Bulb Engine Using a D-C Arc Radiant Energy Source. United Aircraft Research Laboratories Report J-910900-1, September 1970. (present report)

2. Jaminet, J. F. and A. E. Mensing: Experimental Investigation of Simulated-Fuel Containment in R-F Heated and Unheated Two-Component Vortexes. United Aircraft Research Laboratories Report J-910900-2, September 1970.

3. Vogt, P. G.: Development and Tests of Small Fused Silica Models of Transparent Walls for the Nuclear Light Bulb Engine. United Aircraft Research Laboratories Report J-910900-3, September 1970.

4. Roman, W. C.: Experimental Investigation of a High-Intensity R-F Radiant Energy Source to Simulate the Thermal Environment in a Nuclear Light Bulb Engine. United Aircraft Research Laboratories Report J-910900-4, September 1970.

5. Bauer, H. E., R. J. Rodgers and T. S. Latham: Analytical Studies of Start-Up and Dynamic Response Characteristics of the Nuclear Light Bulb Engine. United Aircraft Research Laboratories Report J-910900-5, September 1970.

6. Latham, T. S. and H. E. Bauer: Analytical Studies of In-Reactor Tests of a Nuclear Light Bulb Unit Cell. United Aircraft Research Laboratories Report J-910900-6, September 1970.

7. Palma, G. E. and R. M. Gagosz: Optical Absorption in Transparent Materials During 1.5 Mev Electron Irradiation. United Aircraft Research Laboratories Report J-990929-1, September 1970.

8. Krascella, N. L.: Analytical Study of the Spectral Radiant Flux Emitted from the Fuel Region of a Nuclear Light Bulb Engine. United Aircraft Research Laboratories Report J-910904-1, September 1970.

Report J-910900-1

Results of Experiments to Simulate Radiant

Heating of Propellant in a Nuclear Light Bulb Engine

Using a D-C Arc Radiant Energy Source

TABLE OF CONTENTS

TABLE OF CONTENTS (Continued)

Results of Experiments to Simulate Radiant

Heating of Propellant in a Nuclear Light Bulb Engine

Using a D-C Arc Radiant Energy Source

SUMMARY

Experiments were conducted to simulate radiant heating of the propellant stream of a nuclear light bulb engine. The primary objective was to obtain high exit temperatures in the simulated propellant stream due to the absorption of large percentages of the incident thermal radiation. A high-power d-c arc was used as the radiant energy source and argon seeded with carbon particles was used to simulate the propellant. Unseeded buffer layers were used to prevent coating of the transparent duct walls. Methods were developed for introducing micron-sized carbon seeds into the central region of a three-stream flow in an annular duct to simulate the propellant stream.

The bulk temperature in the exhaust of a reference nuclear light bulb engine is expected to be 12,000 R. A long-range goal of the propellant heating experiments conducted in the laboratory is to obtain as high a value as possible of this bulk exit temperature in a configuration closely simulating that of the engine. The results of the first phase of these experiments indicate that simulated propellant bulk exit temperatures between approximately 3000 and 4000 R have been achieved. Based on thermocouple measurements at lower temperatures, it is inferred that local temperatures at points in the simulated propellant duct were substantially greater than the bulk temperatures. The maximum bulk exit temperatures achieved in the tests to date were primarily limited by the particular cooling configuration employed for the transparent wall adjacent to the radiation source and by partial vaporization of the foam material used at the propellant stream inlets.

By making modifications to the d-c arc radiant energy source and to the propellant heater configuration, it is estimated that propellant bulk exit temperatures approaching 6500 R can be achieved within the next year. This can be accomplished by integration of (1) an upgraded radiant energy source operating at higher powers for shorter run times with (2) an improved propellant duct inlet configuration employing upstream aerodynamic shear for improved deagglomeration of the carbon dispersion. No evidence has been found in tests to date of limitations which would prevent attainment of a bulk exit temperature equal to that in the reference engine after development of the required test equipment. Further development of high-temperature measurement techniques is required to accurately determine the heat content and local temperature of the hot, low velocity, seeded simulated propellant stream in future tests.

As part of this effort to obtain high exhaust temperatures, supporting research was conducted to increase the mass attenuation coefficient of the seeded stream, to determine the optical properties of particle clouds, to develop seeded stream and buffer layer injection geometries that minimize seed coating of the duct walls, and to develop high-temperature measurement techniques for use with particle-laden streams.

RESULTS AND CONCLUSIONS

1. Simulated propellant bulk exit temperatures between approximately 3000 and 4000 R were obtained using thermal radiation from a d-c arc source. Based on thermocouple measurements in tests at lower temperatures, it is inferred that local temperatures at points in the exhaust of the simulated propellant duct were substantially greater than the bulk exit temperatures.

2. Experiments were conducted in which up to 96 percent of the incident radiation was absorbed by the seeded simulated propellant stream. The absorption in tests reported earlier under this program was only 33 percent. Usually, less than 2 percent of the incident radiation was absorbed by seed material deposited on the propellant duct walls during the time the seeds flowed.

3. A propellant duct inlet configuration was developed which allowed several different seed and buffer layer injection geometries to be investigated. Results of cold-flow tests using a configuration with 0.394-in.-wide buffer layers and a 0.118-in.-wide central seeded stream indicated that essentially no wall coating occurred over the 5-in.-long test section length if the buffer layer and seeded stream injection average velocities were matched at 5.0 ft/sec.

4. Cold-flow experiments were conducted in which aerodynamic shear was used to deagglomerate the carbon dispersion. Passage of the carbon dispersion through sonic orifice configurations (hole diameters from 0.02 to 0.05 in.) resulted in mass attenuation coefficients -- averaged over the wavelength range from 0.22 to 2.3 microns -- up to approximately 16.3×10^3 cm^2/g. Injection configurations providing these high levels of mass attenuation coefficient were developed too late in the program to be incorporated in the propellant heating tests discussed above. In the above-mentioned tests, the mass attenuation coefficients were more like the values in tests reported earlier under this program -- on the order of 1000 cm^2/g.

5. A d-c argon arc radiant energy source operating at 1 atm was constructed to serve as the intense nonnuclear radiant energy source for hot-flow testing of the seeded simulated propellant stream. The source was made compatible with the propellant duct inlet configuration and supplied up to 20 kw of radiation incident on the seeded simulated propellant stream. For future tests, this source will be operated at higher powers for shorter run times (several seconds) and will provide greater than 100 kw of radiant energy.

6. Further development of measurement techniques to determine the heat content and local temperature of hot, low-velocity, seeded gas streams is required, particularly for use in the temperature range from 4000 to 7000 R. Possible techniques for consideration include shielded aspirating thermocouples, a fast-response-time calorimeter, and various types of sampling probes.

3

7. Continued research in the area of seeded simulated propellant heating in
laboratory experiments is required to reach bulk exit temperatures approaching
those expected in the nuclear light bulb engine (12,000 R). By using higher arc
powers and making use of the increased mass attenuation coefficients that have been
demonstrated, it should be possible to obtain significant increases in the bulk exit
temperatures relative to those reported herein. Current estimates indicate that bulk
exit temperatures approaching 6500 R are attainable within the next year. No evi-
dence has been found in tests to date of limitations which would prevent attainment
of a bulk exit temperature equal to that in the reference engine after development
of the required test equipment.

SECTION I

INTRODUCTION

An experimental and theoretical investigation of gaseous nuclear rocket technology is being conducted by the United Aircraft Research Laboratories (UARL) under Contract SNPC-70 administered by the joint AEC-NASA Space Nuclear Propulsion Office. The overall research program is directed toward investigating the feasibility of the nuclear light bulb engine. This report discusses that portion of the research program in which a seeded simulated propellant was heated to high temperatures by the absorption of thermal radiation.

Nuclear Light Bulb Concept and Reference Engine Configuration

The nuclear light bulb concept described in Refs. 1 and 2 is based on the principle of transfer of energy by thermal radiation from a fissioning gaseous nuclear fuel to seeded hydrogen propellant flowing through an annulus surrounding the nuclear fuel. Radiant energy is transferred through an internally cooled transparent wall which separates the nuclear fuel from the propellant stream. Figure 1(a) illustrates this principle of operation with a cross section of one unit cavity. The reference engine (Ref. 3) is formed by a cluster of seven such cavities to increase the effective radiating surface area of the nuclear fuel cloud. Figure 1(b) is a schematic of the d-c arc radiant energy source used in the propellant heating simulation tests. The significant dimensions of both the unit cavity and the propellant heating configuration are indicated. Figure 2 is a sketch showing additional detailed dimensions of one unit cavity of the reference engine. One-half of the rotationally symmetric cavity is shown. The propellant region is a divergent annulus 6 ft long with a 1.614-ft inside diameter. The annulus width increases uniformly from 0.104 ft at the inlet to 0.513 ft at the exhaust.

In the reference engine, approximately 98 percent of the total thermal radiation incident on the propellant stream is absorbed by the hydrogen propellant (Ref. 3). Hydrogen is essentially transparent to thermal radiation at the engine operating pressure of 500 atm and below a temperature of approximately 14,000 R. Therefore, a seed material must be added to the propellant stream to provide the required opacity. The ideal seed material would consist of nonreactive, high-melting-point, high-boiling-point, submicron-sized metal particles that exhibit good absorption characteristics in both the particle and vapor forms. Submicron-sized particles, low-ionization-potential metal vapors, and various polyatomic gases have been examined theoretically and experimentally as possible seed materials for the propellant stream (Refs. 4 through 12). Submicron-sized solid or liquid particles exhibit essentially continuous spectral absorption characteristics as contrasted with discrete spectral absorption characteristics exhibited by low-ionization-potential

metal vapors and polyatomic gases. Theoretical studies (Refs. 4 through 8) of the absorption properties of small solid particles have been based on the Mie theory (Ref. 13). This theory describes the spectral extinction, absorption, and scattering of radiation by spherical particles as functions of particle size, material properties, and the wavelength of the incident radiation. The results of these studies indicate that tungsten is attractive as a seed material because of its high melting point, high boiling point, and low reactivity with hydrogen. In the reference engine, nominal 0.05-micron-dia tungsten particles are assumed to be used as a propellant seed material.

In each unit cavity the inner wall of the propellant annulus is highly transparent. The outer wall is highly reflective to reduce the heat load to the moderator and to increase the effective radiant energy path length in the propellant region. A thin layer of unseeded gas flows adjacent to both the inner and the outer walls of the propellant region. These thin unseeded layers serve as buffer regions which prevent the degradation of the optical properties of the walls due to coating by the propellant seed. They also aid in keeping hot gases away from the walls, thus reducing the heat transfer to the duct walls.

For the reference engine, the radiant heat flux at the surface of the nuclear fuel is 177.8 kw/in.^{2}. This flux corresponds to an equivalent black-body radiating temperature of 15,000 R. The inlet conditions in the propellant region are a velocity of 35.5 ft/sec, a bulk temperature of 4,050 R, and an enthalpy of 1.55 x 10^4 Btu/lb. (Slightly lower values of this temperature and enthalpy are calculated for the most recent version of this reference engine -- see Ref. 14.) The corresponding exhaust conditions are a velocity of 23.7 ft/sec, a bulk temperature of 12,000 R, and an enthalpy of 1.033 x 10^5 Btu/lb. The hydrogen weight flow rate per unit cavity is 6.04 lb/sec. The seed weight flow rate is approximately 3 percent of the hydrogen weight flow rate. The hot propellant from the cluster of seven unit cavities exhausts into either a single common nozzle or a multiple nozzle system (Ref. 1).

Principal Objectives

The principal objectives of this portion of the overall research effort are:

(1) to experimentally demonstrate that large fractions of incident thermal radiation from a radiant energy source can be absorbed in a seeded simulated propellant stream to obtain high temperatures at the propellant stream exit; and

(2) to develop methods for deagglomerating and injecting micron-sized solid particle seeds into a simulated propellant stream which consists of three parallel flows (the central stream is seeded; the two adjacent unseeded streams act as buffer layers to prevent coating of the transparent walls).

Experimental Approach

The approach taken was to first conduct a preliminary series of cold-flow tests with modified versions of the propellant inlet geometry used in the initial propellant heating program described in Ref. 15. The results were used to test the hypotheses upon which a more advanced propellant inlet was based. The more advanced propellant inlet design incorporated replaceable parts to permit variations of the basic inlet design to be tested in cold-flow tests. In addition, the advanced configuration was designed to be compatible with the d-c arc radiant energy source.

Modifications were made to the d-c arc source used in the initial propellant heating program (Ref. 15). These permitted operation of the source at high powers in a geometry suitable for propellant heating tests. This source was used for the hot-flow tests reported herein.

Additional cold-flow tests were conducted to increase the mass attenuation coefficient of the carbon seed used as the simulated propellant stream. This was accomplished through application of aerodynamic shear to the flowing carbon dispersion. Success in this area was attained too far into the program for this technique to be incorporated in the d-c arc propellant heating tests. A simplified analytical heat transfer analysis of the simulated propellant stream, including the effects of reradiation from the hot propellant stream, was also conducted.

This report is divided into separate sections describing the principal equipment used, discussing the cold-flow tests, and discussing the hot-flow tests. Also included are four appendixes on the optical properties of particle clouds, on the calculation procedure for obtaining propellant stream bulk exit temperature, on flow visualization tests using a two-dimensional flow channel, and on special instrumentation tests using a plasma torch which are applicable to future propellant heating tests (Appendixes A through D, respectively).

SECTION II

DESCRIPTION OF PRINCIPAL EQUIPMENT

Figure 3 is a sketch of the basic d-c arc heater configuration with the simulated propellant heating assembly. Details of the propellant heating assembly are discussed in the following sections. The d-c arc heater was constructed in 1968 as part of a UARL Corporate-sponsored program. A block diagram of the primary electrical components of the d-c arc heater is shown in Fig. 4. The basic d-c arc heater consists of motor-generator power supplies, rheostat controls, starting controls, switchgear, a variable ballast resistor, current and voltage meters, and the d-c arc source. The arc power is supplied by two shunt-wound General Electric motor-generator sets rated at 250 kw each. The motor generators may be connected for either series or parallel operation. The d-c power output is varied using a remote-controlled rheostat. This permits the motor-generator field voltage to be preset prior to arc initiation, in addition to being varied during test operation.

A more detailed diagram of the d-c arc heater electrical circuit is shown in Fig. 5. Included are the circuitry for the motor generator sets, the d-c arc monitoring and control instruments, and the d-c arc starter system. All control units, including a remote start-stop control, are located on the arc control console, shown in Fig. 5.

Figure 6 shows the electrical operating characteristics of the d-c arc heater as used for the propellant heating tests reported herein. The tests employed an argon arc operating at approximately 1.0 atm pressure. For these tests, the motor-generator sets were connected in series. As shown in Fig. 6, the arc current and voltage ranged, respectively, from 295 to 850 amps, and from 122 to 175 volts d-c. The maximum total arc power for these tests was 148.75 kw. The fraction of the arc power available for heating the simulated propellant was relatively modest compared with the total power deposited in the d-c arc. This was because of the associated power losses to the cathode, anode, and other water-cooled components. Also, as shown in Fig. 3, the propellant stream is not exposed to the upper portion of the arc column. Modifying the arc configuration can serve to reduce some of these losses. For example, a more compact arc configuration, which operates for shorter test times (1 to 5 sec), could expose a larger fraction of the arc to the propellant stream and also reduce the losses to the water-cooled components. As reported in Ref. 15, d-c arc tests have been conducted, with equipment similar to that described herein, in which the arc current was greater than 1450 amps. The maximum total arc power in that series of tests was approximately 230 kw. For these shorter-time tests, the motor generators were operated in a series overload condition. The maximum rated power available from the motor-generator sets is 0.5 megw.

The operating range for which d-c arc stability can be attained (with their inherent nonlinear dependence between voltage and current) is restricted by configuration, circuit and flow considerations. The arc may also exhibit large variations in static voltage-current characteristics, depending on environmental conditions. From electrical circuit considerations, the arc circuit is stable provided $R_B + dV_A/dI_A > 0$, where R_B is the ballast resistance, V_A is arc voltage, and I_A is arc current. To satisfy this stability criterion, an air-cooled ballast resistor was added to the d-c power supply circuit (Fig. 5). A distinct advantage of d-c arc operation using motor-generator power supplies is the elimination of undesirable power supply ripple inherent in all moving-coil-transformer or saturable-reactor type power supplies.

<div align="center">D-C Arc Source Configuration</div>

Electrodes
_____

The basic d-c arc heater configuration (Fig. 3) consists of a vortex-stabilized d-c arc enclosed within concentric, water-cooled, fused silica tubes. The nominal dimensions of the inner fused silica tube were 1.26-in.-ID by 1.38-in.-OD, and those of the outer fused silica tube were 1.57-in.-ID by 1.69-in.-OD. The arc is established between a pin cathode and a hollow cylindrical anode. The cathode is a hemispherical-tipped, 2.0-percent thoriated-tungsten rod of 0.25-in. diameter. The cathode is recessed and silver-soldered into a water-cooled copper well. The vertical location of the cathode can be varied to optimize the location, size, operating temperature, and constriction of the cathode attachment spot. Experiments have indicated that the cathode operating temperature plays a role in achieving stable, uncontaminated, long-lifetime operation, particularly at high power levels. The cathode water-cooling flow rate, which also influences this condition, could also be varied. The cathode in the d-c arc heater configuration (Fig. 3) is raised up into the fused silica tube (1/2 in. above the seed injection annulus inlet plane), as opposed to being positioned at the lower end of the fused silica tube as in the tests discussed in Ref. 15. This new location helps to eliminate the difficulties encountered due to radiation heating of the "0"-ring seals at the lower end of the fused silica tubes. The new location also decreased the direct radiant heating on the stainless steel injectors of the propellant duct. This modification allows higher power arc operation with the propellant heating configuration than previously could be achieved. The cylindrical water-cooled copper anode (Fig. 3) contains a 0.5-in.-dia hole with rounded corners on its centerline. Recessed in the anode's outer periphery is a water-cooled magnetic field coil. The magnetic field coil is electrically connected in series with the arc. The interaction between the magnetic field generated by the coil and the arc current in the anode attachment region ($\overline{J} \times \overline{B}$ force) causes the arc anode attachment spot(s) to rotate rapidly. By magnetically driving the anode spot(s) at high speeds (approximately 2000 rev/sec) over the anode surface, the very high heat load in the anode spot region is spread

over a significantly larger area. This permits the high-velocity water-cooling flowing meridionally within the anode coolant passage to remove the heat more effectively. This magnetically augmented water-cooled anode is capable of operation at current levels of approximately 1500 amp. The average lifetime of the anode is several hours.

Arc Flow System

Vortex Injectors

The arc column is stabilized by the vortex flow which is introduced into the plenum surrounding the cathode assembly (Fig. 3). The vortex generator injection assembly has four equally spaced vertical stainless steel tubes through which argon gas flows. Each of these tubes has four 0.015-in.-dia holes, spaced 0.118 in. apart. In addition to desirable arc column characteristics, the argon provides a nonoxidizing environment which minimizes erosion of the tungsten cathode. The angle of vortex injection can be varied from full radial (coaxial flow parallel to discharge axis) to full tangential (vortex flow) during arc operation by a variable-speed servo-motor drive and gear assembly. This permits establishing the optimum vortex geometry for a particular power level and vortex tube length-to-diameter ratio. The optimum condition is when the discharge axis is steady and colinear with the axis of the fused silica tube surrounding the discharge. The vortex generator is connected to the lower end of the inner fused silica tube through a convergent nozzle section. Argon weight flow rates up to 0.024 lb/sec were used in the vortex generator.

Locator

The transition of the arc from the positive column to the anode region occurs at the water-cooled copper locator (Fig. 3). The locator helps confine the arc to the centerline of the fused silica tube. It also acts as an interface between the plasma column of the test section and the top of the d-c arc heater. The convergent-divergent shape of the locator helps minimize anode erosion by directing the arc column into the center of the anode. The inner diameter of the locator was chosen as 5/8 in. to minimize constriction effects on the arc column (these, in turn, may set up undesirable jets due to magnetic pinch effect). The locator design incorporated improved shielding for the "O"-ring seals at the upper end of the fused silica tubes. The cathode and anode were electrically isolated from the components of the propellant heating test equipment and from the table which supported the configuration.

Arc Starting System

The arc was initiated by employing a secondary tungsten-tipped stainless steel anode (0.25-in.-dia rod, 30.25 in. long) which initially made contact with the cathode tip, and was then rapidly withdrawn (approximately 10 ft/sec) upward through

the primary anode. In this way, the arc was drawn vertically upward until it reached the level of the primary anode (see Fig. 5). Arc transfer from the secondary anode to the primary anode was accomplished as the secondary anode continued upward to its fully retracted position. The starting system was actuated by a two-way pneumatic cylinder. The starting sequence was synchronized such that withdrawal of the secondary anode lagged the main arc power initiation by approximately 0.5 sec. This fully established the arc prior to rapidly drawing apart the electrodes. During the starting sequence, an air-cooled ballast resistor was used to limit the arc current to approximately 50 amp. The current-limiting technique was used to reduce contamination of the test-section walls due to tungsten sputtering caused by a sudden high-current arc, or the contamination which would be given off had an exploding wire starting technique been employed. After the arc transfers from the secondary to the primary anode, less ballast resistance is present in the arc circuit (see Fig. 5).

Gas and Water Cooling Systems

The gas and water cooling systems for the d-c arc heater are shown schematically in Fig. 7. A centrifugal-type water pump, rated at 180 psi and 150 gpm, supplied the water-cooling for the propellant duct walls, locator, and exhaust gas calorimeter (discussed in the following subsection). A reciprocating-type water pump rated at 450 psig and 20 gpm supplied the water-cooling for the anode, cathode, and magnetic field coil. The water-coolant lines were connected from the individual pump manifolds to the various elements of the test equipment by high pressure, electrically nonconducting flexible nylon hose. The water-coolant flow rate to each element was controlled by means of separate valves. The low pressure return lines fed into rotameters to permit determination of the coolant flow rate through each element. After flowing through the rotameters, all coolant flows were connected to a common water exhaust manifold and drain. The temperature of the water entering the water-flow system was monitored by a thermocouple located at the inlet manifold. The temperature of the water leaving each element was monitored by separate thermocouples located close to the exhaust of each element. Copper/Constantan thermocouples were used to measure all water temperatures.

Argon for the d-c arc vortex generator and the simulated propellant stream was provided from separate high pressure supplies. The argon vortex generator supply consisted of two argon bottles (245 scf each) manifolded together. The argon supply for the simulated propellant flows consisted of eleven argon bottles (245 scf each) manifolded together. The argon flow rates were monitored using rotameters. The d-c arc heater vent was connected to a 1500 cfm axial fan which was located directly above the test section. Figure 8 is a photograph of the test configuration. Illustrated are the major arc components, the water-cooling and gas connections, the propellant duct, and the exhaust vent. The vortex control system is shown in the lower right-hand corner of Fig. 8.

The test stand (see Fig. 8) allows easy removal and attachment of the various arc components and the numerous propellant stream feed lines (seed and buffer). Vertical adjustments can be made to permit location of the 5-in.-long test section in different positions relative to diagnostic equipment located outisde of the test chamber (e.g., radiometer and cameras).

Diagnostic Equipment

Radiation Measurements

The power radiated from the plasma column was measured using a radiometer incorporating a BaF_2 thermopile detector. As discussed below, this radiometer was calibrated by three methods. For the tests reported herein, total radiation measurements were obtained in the wavelength range of 0.25 to 1.3 microns. A sketch of the radiometer optical system is shown in Fig. 9. The radiometer was positioned such that the arc column was viewed through a 1.0-in.-wide by 0.75-in.-high aperture located 8.0 in. from the test section. The 0.234-in. by 0.234-in. BaF_2 thermopile element was located 39.4 in. from the test section centerline. This optical system allowed the radiometer to view a 1.0-in.-high by 1.26-in.-wide section of the region within which the plasma column was located. The diameter of the plasma column was about 0.75 in. Thus, the plasma column did not completely fill the 1.26-in. width of the viewing area. The center of the region viewed was about 2.5 in. above the cathode tip (see Fig. 3).

The radiometer was calibrated with a standard lamp (General Electric DXW quartz-iodine tungsten filament lamp) of known spectral characteristics. The 1.0-in.-long filament of the lamp was positioned in a location equivalent to the position of the test section centerline in Fig. 9, within the 1-in.-high view of the radiometer.

Because of the uncertainties involved in calculating the total radiant heat flux incident on the seeded propellant stream from radiometer measurements at one isolated point, a series of tests was conducted in which the propellant stream was simulated by a blackened surface surrounding the d-c source. The total radiant heat deposited at this surface was measured and compared with that determined from radiometer measurements. An uncooled copper cylinder (6.0 in. long) was located concentric with the source axis and was instrumented with several thermocouples. Both shielded (ungrounded) and exposed-junction chromel/alumel thermocouples were used. Locations were selected at the central portion and extremities of the cylinder to permit a check on the thermal response and spatial temperature distribution. To minimize the amount of heat convected away from the cylinder to its surroundings, thereby reducing the measured temperature rise, layers of asbestos insulation and teflon strips were located around the outer periphery and top of the cylinder. To reduce stray reflections from the inner surface of the cylinder, the entire inside surface was coated with carbon residue from an acetylene flame. The change in cylinder temperature during a run was determined from the thermocouple

output voltage. Due to the effects of the initial low-current starting sequence, which lasted approximately 0.8 sec, two separate thermocouple readings were taken to determine the heat flux to the cylinder inner surface during operation with the main arc current. First, only the starting sequence was operated; then, in the second test, the high-current data were taken. The difference of the two readings is proportional to the cylinder heat load during operation with the main arc current.

The copper cylinder was located 0.39 in. from the outer fused silica tube (1.75-in.-OD) and was separated from the source by two fused silica tubes and an annulus of cooling-water 0.10 in. thick. The energy conducted and convected from the source to the copper cylinder was neglected. Therefore, the values obtained from the copper cylinder data should approximate those obtained from calculations using the radiometer. The results indicated reasonably good agreement between radiometer measurements and measurements obtained using the transient calorimetric technique (use of uncooled copper sleeve of known dimensions and mass in the propellant duct). The total radiated power determined from radiometer measurements of a portion of the test section (see Fig. 3) was approximately 10 to 20 percent greater than that obtained from the copper sleeve measurements.

To have another independent check on the radiated power incident on the propellant duct test section, a series of tests was conducted in which a known concentration of an organic water-soluble dye (nigrosine) was added to the coolant fluid of the outermost set of fused silica tubes (Fig. 3). The total radiation absorbed in the water-dye coolant was then measured. Taking the estimated losses into account, the results compared favorably with both the radiometer measurements and the copper-sleeve calorimetric measurements. The results were also consistent with estimates of the expected behavior of the arc for the given test conditions. These alternate and independent measurements of the total radiated power incident on the propellant duct test section provided verification of the radiation attenuation measurements and data reduction procedures used later in hot-flow tests.

The d-c arc propellant heater configuration was operated steady-state at total radiation levels incident on the 5.0-in.-long propellant duct test section of slightly greater than 20 kw. Depending on the arc current, argon weight flow rate, and vortex injection angle, the percentage of total arc power radiated per unit length ranged from about 50 to 70 percent.

A series of tests was conducted to determine the fraction of radiation absorbed in the cooling-water and fused silica tubes surrounding the d-c source. These tests were conducted at power levels which permitted long run times. For the test geometry shown in Fig. 3, a 0.099-in. annulus of cooling water surrounded the arc discharge. The results indicated that, with approximately 30 kw of d-c power deposited into the source within the test section, less than 1 kw was deposited into the cathode cooling water. About 6 kw was deposited into the locator and 8 kw was deposited into the annular cooling water flowing between the concentric fused silica tubes.

The total radiation per inch of arc length in the test section was measured using a radiometer. The measurements indicate that approximately 9 kw was radiated through the water-cooled test section. When the outer annulus of water coolant was removed, the radiometer measurements indicate that approximately 11 kw was radiated through the test section for the same 30-kw input power.

The percent of total radiation passing through the cooling water and fused silica tubes surrounding the d-c arc, in various wavelength bands, was measured using a radiometer. The resulting spectral distribution is shown in Fig. 10. The total power to the d-c arc was 35 kw. The arc pressure was about 1.0 atm with an argon vortex flow of 0.018 lb/sec. This is typical of the type of spectral distribution incident on the simulated propellant stream. However, for tests at higher power the spectrum may shift toward the ultraviolet. The transmission characteristics of the filters used with the radiometer to obtain the above spectral characteristics are shown in Fig. 11. The transmission characteristics of a 0.099-in.-thick water layer are also shown.

Calorimetry

One of the methods used (for some tests) to determine the propellant bulk exit temperature was based on calorimetry. A water-cooled calorimeter was used to cool the seeded simulated propellant stream after it left the test section. The calorimeter was located directly above the test section and below the arc anode assembly as shown in Figs. 3 and 8. After passing through the test section and calorimeter, the simulated propellant stream was ducted to an exhaust hood through eight copper exhaust vent tubes (see Fig. 8). A detailed sketch of the calorimeter and its surrounding components is shown in Fig. 12. The calorimeter cooling coils were fabricated using 0.1875-in.-dia copper tubing. Copper wire with a 0.04-in.-dia was wound around the copper cooling coils to provide the desired spacing between the coils. Because of the close proximity of other parts to the hot simulated propellant exhaust, not all of the energy in the propellant exhaust was absorbed in the calorimeter. Therefore, the change in energy content of the cooling water for the locator, the two water-cooling annuli, and the calorimeter had to be accounted for in the calorimetric determination of the simulated propellant bulk exit temperature. The temperature change of the simulated propellant gases exhausting to the vent was also measured. All the water-cooling temperatures were measured using copper/constantan thermocouples. The gas exit temperature was measured using a chromel/alumel thermocouple. The various exhaust temperatures were first measured with only argon flowing through the test section. They were remeasured after equilibrium was reached while the seeds were flowing through the test section. To account for possible heat sinking and transient effects, time was allowed for each of the various sensors to come to complete steady-state readings for each test condition. Equilibration of the water-cooling temperatures typically took about 15 sec. The results of the simulated propellant bulk exit temperature determinations by calorimetry are discussed in Section IV.

Thermocouples

Measurements of the local temperature in the simulated propellant exhaust were made using thermocouples. Figure 12 shows schematically the location of the thermocouples. The thermocouples could be introduced into the exhaust either axially or radially as shown in Fig. 12. During most tests only one thermocouple was used.

Chromel/alumel thermocouples with the following types of thermocouple junctions were used: exposed welded, eroding, shielded aspirating, and right-angle. An exposed junction tungsten/tungsten 26 percent rhenium was also used. Figure 13 is a photograph of these thermocouples, showing the approximate size of each and the stem type; a close-up view of each thermocouple junction is shown in Fig. 14. The sheaths of the chromel/alumel thermocouples were made of 1/8-in.-dia tantalum, with stem lengths ranging from 6 in. to 12 in. The thermal elements were insulated from each other and from the sheath with magnesium oxide. The calibrated range of the chromel/ alumel thermocouples was up to 2500 R. The exposed junction type thermocouple (Figs. 13 and 14) had the elements welded together and exposed directly to the gas stream. The elements of the eroding junction type thermocouples (Figs. 13 and 14) are two 0.02-in.-thick ribbons insulated from each other. Upon exposure to a hot impinging gas stream (such as a hot particle-laden flow), the junctions erode, causing thin strips of metal to bridge the gap between the elements forming the thermocouple junction. This type of design allows continuous monitoring of the temperature while the junction is being eroded. Thus, the life of the thermocouple in this environment is considerably longer than that of thermocouples with other type junctions. The shielded aspirating type thermocouple (Figs. 13 and 14) had an exposed junction type thermocouple enclosed within a 1/16-in.-OD shield to reduce possible errors in the measured temperature due to the location of the thermocouple in a radiation field. The thermocouple junction was located about 3/16 in. from the open end of the shield. The shield had four 1/64-in.-dia holes 1/4 in. back from the tip of the shield to allow the hot gas to flow up inside the shield past the thermocouple junction and out through the holes. The fourth type of chromel/alumel thermocouple used was a right-angle type (Figs. 13 and 14). The thermal junction is at right angles to the longitudinal axis of the probe. The thermal element consists of ribbons electrically welded together at the sensing tip. The ribbons in the vicinity of the thermal junction are parallel to the direction of the gas flow and extend from the thermocouple stem. Both of the elements near the thermocouple junction are heated directly by the gas stream, thereby reducing the effects of conduction on the thermocouple measurement.

The tungsten/tungsten 26 percent rhenium thermocouple (Fig. 13) had a 1/8-in.-OD by 6-in.-long molybdenum stem. The thermal elements were insulated from each other and the stem by thorium oxide. The calibrated range of this type thermocouple was up to 4500 R. The thermal junction was exposed, with the elements welded together. The exposed element of this type thermocouple was very fragile. The results and discussion of the application of these types of thermocouples to the measurement of the simulated propellant local exit temperature are given in Section IV.

The response time of the thermocouples as used in tests reported herein was about 18 sec.

Recording Equipment

The output of the thermocouples for the water and gas exit temperatures and the output of the radiometer were recorded on strip chart recorders. The cooling water and argon gas flow rates were measured using rotameters. The d-c current, voltage, and motor-generator field voltage were displayed on meters on the control console. Still photographs of selected tests were taken with a Polaroid camera. High-speed motion pictures of a few tests were taken with a HyCam 16-mm camera, operating at several speeds between 200 and 1000 frames/sec.

Seed Dispersal System

Figure 15 is a schematic diagram of the simulated propellant flow system and high-pressure seed dispersal system. This system provides the required flows of seeds, carrier gas, and buffer gas. Carbon seed material having a nominal diameter of 0.012 microns was used in these tests instead of tungsten as considered for the nuclear light bulb engine because its optical characteristics over the size range of interest are well known. In addition, carbon seed is readily available, inexpensive, and easier to handle than tungsten. Argon was used as the seed carrier and buffer gas in all tests. The seed dispersal system consists of a 5.0-in.-ID by 11.75-in.-deep, high-pressure (3000 psig), stainless steel canister. However, for the tests reported herein, the canister maximum pressure was considerably lower than 3000 psig. Carbon particles were placed in the canister (approximately 2/3 full). The carbon was dispersed within the canister by rotating agitator blades located in the upper portion of the canister. The agitator blades were driven at a rotational speed between 214 rpm and 2140 rpm using a variable-speed motor. Argon was passed through the canister, entraining dispersed carbon particles with it. The argon entering through the top face of the canister also helped to agitate the carbon powder through aerodynamic forces. The ratio of total argon weight flow rate to carbon weight flow rate was varied by allowing some of the total argon carrier flow to bypass the canister (see Fig. 15). The carbon weight flow rate could also be varied by changing the rotational speed of the agitator blades. The seeded argon flow line was connected to the plenum of the seeded gas injection duct in the stimulated propellant flow chamber. For the typical carbon seed weight flow rates used in the tests, the capacity of the canister was sufficient to permit total test times of approximately 5 min before the carbon supply was depleted. Two argon flow lines for the separate buffer layers were also connected to their respective plenums in the simulated propellant flow chamber. Individual pressure regulators, pressure gauges, control valves, and flow metering equipment were used for each system. Argon flow rates were measured with rotameters.

SECTION III

DISCUSSION OF COLD-FLOW TESTS

Objective

The objective of cold-flow tests is to develop a flow configuration suitable for heating a gas seeded with sub-micron particles to a high temperature by the absorption of thermal radiation. The desired flow configuration consists of a seeded gas stream flowing in an annular duct, as in the reference nuclear light bulb engine. The seeded gas stream is separated from the duct walls by buffer layers of unseeded gas. The buffer layers prevent coating of the walls by the seed material. Development of a seed dispersal system (Section II) and improvement of the carbon seed mass attenuation coefficient are also important aspects of the cold-flow tests.

Preliminary Tests

The results of experiments discussed in Ref. 16 indicated that the use of porous foam across the inlet region of the propellant duct is one method that could help minimize the amount of seed deposition on the duct walls. The porous foam reduces the velocity gradients at the boundaries between the three flows, helping to reduce turbulent spreading of the central seeded stream toward the duct wall. Another method for minimizing the seed deposition on the duct wall is to increase the buffer layer thickness. The combined effect of these methods was investigated using a configuration similar to that used in the initial propellant heating tests and shown in Fig. 36 of Ref. 15. This configuration has two 0.117-in.-wide buffer layers and a 0.039-in.-wide seed injection annulus. For this particular configuration, the foam had no beneficial effect on the coating of the walls by the carbon seed material. Seeds were deposited at distances greater than approximately 0.5 in. downstream of the foam.

The duct geometry was modified such that the width of the inner buffer layer was increased to 0.234 in. (the outer buffer and seed annulus dimensions remained at 0.117 and 0.039 in., respectively). In tests without foam at the duct inlet, the inner wall remained clear for a distance of about 3.0 in. When foam was placed in the duct inlet, this distance was increased to approximately 5.0 in. The wall adjacent to the 0.117-in.-wide buffer layer became coated as above in both cases. The duct geometry was modified again such that the outer 0.117-in.-wide buffer layer was increased in width to 0.176 in. Without foam, the 0.176-in.-wide buffer layer kept the wall clean for about 0.75 in. With foam in the inlet regions of the ducts, the wall adjacent to the 0.234-in.-wide buffer layer was clean for

5.5 in., and adjacent to the 0.176-in.-wide buffer layer, the wall was clean for
1.5 in. The cleanliness of the walls was determined by visual inspection. The
stream velocities for these tests were matched at about 15 ft/sec.

The results of these preliminary tests indicated that for thick buffer layers
(0.234 in. and 0.176 in.) the use of porous foam across the inlet plane resulted
in reduced wall coating, while for thin buffer layers (0.117 in.) the foam had no
noticable effect on wall coating.

Tests with Improved Inlet Design

An improved propellant duct inlet geometry, shown in Fig. 16, was designed and
fabricated for use with the d-c arc source. The inlet is axisymmetric. This geo-
metry was designed to provide improved flow characteristics over that used in the
initial propellant heating tests reported in Ref. 15. It employs improved inlet
aerodynamics and porous foam material in various locations to aid in distributing
the flow uniformly and to smooth velocity gradients. In addition, the stainless
steel inserts separating the seed duct from the buffer ducts were tapered to knife
edges (approximately 7-deg half-angle).

The buffer and seed flows are each introduced into the assembly through six
0.25-in.-dia inlet ports equally spaced around the circumference of the inlet
housing (Fig. 16). The propellant duct width, the buffer layer widths, and the
seed annulus width can be varied by replacing the parts labelled 1, 2, 3, and 4 in
Fig. 16 and by using different-sized outer fused silica tubes. This configuration
can be used for hot tests with the d-c arc. Porous foam material was placed in
various locations (denoted by X, Y, and Z in Fig. 16) to provide flow uniformity
and to smooth the velocity profiles at the propellant duct inlet plane. Figure 17
is a photograph of the disassembled inlet.

A series of cold flow tests were conducted with a configuration having 0.394-
in.-wide buffer layers along both the inner and outer fused silica tube walls and
a 0.118-in.-wide seeded-gas injection annulus. In these tests, the buffer layers
and seeded gas injection velocity were each 5.0 ft/sec at the inlet plane to the
test section (location Z in Fig. 16). The Reynolds number based on the propellant
duct width was 2700 and the pressure in the propellant duct was 1.0 atm.

During some tests, quantitative measurements were made of the wall coating
which occurred. A tungsten filament lamp was located coaxially within the inner-
most tube (see Fig. 18(a)). A radiometer located outside the test section was used
to measure the light transmitted through the test section before, during, and
after seeds flowed. Tests were conducted with and without foam at the exit plane
(position Z). Light attenuation of up to 90 percent was measured with a return to
within 2 percent of the clean wall condition after the seeds had been passed through

the test section. Figure 18(b) is a typical radiometer trace from a test with
45 ppi (pores per linear inch) foam placed in locations X, Y, and Z. The seed flow
was steady with an attenuation of about 50 percent. After about 110 sec, the seed
flow was increased, with a resulting attentuation of about 85 percent. The seed
flow was then turned off and the light transmitted returned to its value at the
start of the run. This value was approximately 98 percent of the transmission
with clean walls. It also should be noted that, because of the presence of
streamers in the flow (discussed in following paragraphs), the radiometer attenu-
ation measurements represent average values. The radiometer was exposed to an area
that includes several streamers; therefore, the attenuation within each streamer
was greater than that determined from the radiometer data (see discussion in
Appendix C).

Figure 18 illustrates the results obtained during a test at a low seed flow
rate. Figure 18(a) is a photograph showing streamers in the seeded gas flow.
Tests were conducted to determine the origin of these streamers and to eliminate
them if possible. The seeded-gas inlet was tested without the fused silica walls,
buffer flows, or foam across the exit plane (location Z in Fig. 16). No streamers
were observed under these conditions. It was concluded that the seed inlet itself
was not the source of the streamers. The effect of foam of various porosities
located in position Z (Fig. 16) was investigated by visual observation. The
porosity of the foam ranged from 20 ppi to 80 ppi. Streamers were observed during
all tests. The foam with large pores produced coarse streamers and the foam with
small pores produced very fine streamers. However, the foam with small pores
showed noticable accumulation of the carbon seed in the foam. For this reason,
this foam was not used with this configuration in the hot-flow tests. The accumu-
lation of seed particles within the foam might possibly be reduced by filtering or
by improved deagglomeration of the particle stream.

Further tests were conducted without foam across the exit plane but with foam
at locations X and Y. The flow in the test section was not as free of disturbances
as it was with foam at the exit plane and streamers were again observed. The
porosity of the foam located in position Y (see Fig. 16) was also found to influence
the size of the streamers produced. Large streamers were produced when large pore
size was used. When the foam in position Y was moved down in the inlet so that its
upper surface was as far from the inlet plane as possible (about 1.5 in.), the
streaming effect was reduced. Foam with fine pore size in this position further
reduced the streaming effect.

It was concluded that the streaming effect which was caused by foam at the
inlet plane of the test section might be reduced to an acceptable level with further
improvements of the inlet geometry. These conclusions are supported by the results
of the tests using a two-dimensional propellant duct configuration discussed in
Appendix C.

A second series of cold-flow tests were conducted using the inlet configuration shown in Fig. 16. In these tests, the orientation of the configuration was changed so that the flow was horizontal rather than vertical. This permitted simulation of the orientation of the propellant duct used in the 1.2-megw r-f induction heater (see Ref. 17). The buffer layers were 0.394 in. wide, as in the d-c arc radiant energy source tests, and the seed injection annulus was 0.118 in. wide at the inlet plane. The average velocities of the three flows were again matched; the velocities at the inlet plane ranged from 5 to 15 ft/sec. Settling out of large agglomerates was noted. This resulted in a light coating of the lower portion of the outer duct wall and the upper portion of the inner duct wall. For a stream velocity of 10 ft/sec, the start of the coating due to settling was approximately 7 in. downstream of the foam at the inlet plane. The particles that settled out represented a small fraction of the total carbon weight flow. The settling out might be eliminated by improved deagglomeration of the particle cloud (i.e., reduction of particle size) and/or removal of the large agglomerates.

A series of cold-flow tests was conducted to investigate the characteristics of propellant ducts having thinner buffer layers than those used above. Thinner buffer layers are desirable because they offer the opportunity to achieve higher propellant bulk exit temperatures. If the same amount of thermal radiation is absorbed by the seeded portion of the propellant stream, then the bulk exit temperatures will be higher when the unseeded buffer layer mass flow (and, hence, the total propellant stream mass flow) is reduced. The primary problem that must be overcome is that the thinner buffer layers must still prevent coating of the propellant duct walls by carbon seeds.

Tests were conducted using an inlet configuration similar to that shown in Figs. 16 and 17. The widths of the inner buffer layer inlet annulus, the seeded stream annulus, and the outer buffer layer annulus were 0.236 in., 0.059 in., and 0.236 in., respectively. The corresponding dimensions of the configuration used in the cold-flow tests above were 0.394 in., 0.118 in., and 0.394 in. Tests were conducted with and without porous foam material across the inlet plane (Fig. 16). The average velocities of the seed and buffer flows ranged from 5 to 15 ft/sec and were matched at the inlet plane of the test section. The results indicated that, with the best foam configuration, the transparent duct walls coated lightly up to a certain axial location downstream of the inlet plane. Beyond this point, rapid transition to a very dark coating occurred. Under the best conditions, the location of this transition varied from 3 to 5-1/2 in. downstream of the inlet plane. In general, the performance of the configuration having 0.236-in.-thick buffer layers was not as good as the performance with thicker buffer layers (0.394 in.) under similar flow conditions.

Based on the results of these cold-flow tests, propellant heating using the d-c arc radiant energy source was conducted using two 0.394-in.-wide buffer layers and a 0.118-in.-wide seed annulus with porous foam (45 ppi) located in the positions labelled X, Y, and Z in Fig. 16. Further efforts to reduce the streamer effect

noted above were not made. It was considered more desirable to proceed with the simulated propellant heating tests rather than continue work on reducing the streamer effect.

Average Mass Attenuation Coefficient Tests

The purpose of these tests was to increase the mass attenuation coefficient of carbon-argon dispersions for use in simulated propellant heating tests. These tests were conducted concurrent with the hot-flow simulated propellant heating tests discussed in the next section. However, the final results were not available until after the hot-flow tests were completed. Therefore, for the cold-flow tests discussed in this section and the hot-flow tests discussed in the next section, no measures were taken to increase the mass attenuation coefficient of the carbon seed. The mass attenuation coefficient can be increased by reducing the size of the carbon agglomerates. This size reduction can be accomplished by the application of aero-dynamic shear to the flowing dispersion (Refs. 11 and 12). For tests discussed in Refs. 11 and 12, the mass attenuation coefficient was measured at specific wave-lengths covering a range from about 0.06 to 0.8 microns. The wavelength average mass attenuation coefficient as discussed here was measured over a wide wavelength range of about 0.22 to 2.3 microns.

The attenuation of a beam of radiation passing through a particle cloud can be described by

$$\frac{I}{I_0} = \exp\left[-\rho_s \beta \ell\right] = \eta_T \tag{1}$$

where I_0 is the intensity of the incident beam, I is the intensity of the transmitted beam, ρ_s is the dispersed seed density, β is the mass attenuation coefficient and ℓ is the radiation path length through the cloud. The ratio I/I_0 is the fraction of the radiation transmitted, η_T. The fraction of the radiation absorbed, η_A, is $1-\eta_T$. A more complete discussion of this relationship and the optical properties of particle clouds is given in Appendix A.

With these objectives in mind, tests were conducted in which the particle clouds were subjected to aerodynamic shear to reduce the size of the large agglomerates. Aerodynamic shear was provided by passing seeded gas through an orifice made by drilling various-sized holes in thin sheet metal (0.007-in. thick). Each orifice tested had a single hole of the desired size in the orifice plate.

Figure 19 is a sketch of the test arrangement. The dispersed carbon flowed between a tungsten ribbon lamp and a radiometer. The radiometer viewed the flowing carbon through a collimating tube such that a beam about 1/8-in. in diameter was viewed across the exit plane of the seed duct. The radiometer was located such

that the beam viewed as close to the exit plane as possible. This was done so that very little spreading of the seeded exhaust jet could occur before reaching the beam. The beam width through the dispersed carbon was assumed to be equal to the 0.426-in.-ID of the copper tube. The seeded gas exhausted into an exhaust vent located directly above the test equipment. The orifice holder was 5 in. below the carbon exit plane. The seeded gas flowed from the seed dispersal chamber through a mixing chamber to the orifice (see Fig. 19). The system for flowing argon to the seed dispersal chamber was similar to that used for the propellant heating tests. The ratio of total argon weight flow rate to carbon weight flow rate was varied by allowing some of the argon carrier gas to bypass the dispersal chamber. The carbon seed was dispersed in the chamber by the aerodynamic forces exerted by the bleed flow through the dispersal chamber. The weight of carbon seed used during each test was determined by weighing the seed canister before and after each test. A light-weight dispersal system was developed specifically for these tests so that the amount of carbon used during each test could be accurately determined. The system is capable of operation at pressures up to 400 psi.

Figure 20(a) summarizes the test conditions, argon flow rates, orifice diameters, and orifice pressure drops employed in the tests. The argon flow rate was selected to be the same as flowed through one of the six inlet feed lines for the seeded gas stream of the propellant heating configuration. The propellant heating configuration is discussed in the following section. The carbon seed dispersion was subjected to increasing shear by reducing the orifice size while maintaining about the same argon flow rate, thus increasing the pressure drop across successive orifices.

Figure 20(b) shows a data trace from the radiometer for one of these tests. Data traces of this type were used to calculate the mass attenuation coefficient (assumed constant for each test). The total amount of carbon used during each test was expressed in terms of an integral of the data trace. This integral was expressed in terms of mass attenuation coefficient and equated to the measured weight change. The value of the mass attenuation coefficient was calculated from the resulting expression. Appendix A discusses this calculation procedure in more detail.

Figure 21 is a plot of the effect of orifice pressure drop on the mass attenuation coefficient. The mass attenuation coefficient is shown to increase from values between 1025 and 2261 cm^2/g with no orifice to values between 5010 and 16,362 with a pressure drop of about 400 psi. Because of the time averaging procuedure used to calculate these data and the assumed constant value of β during each test (see Appendix A), the calculated values in Fig. 21 may be lower than the maximum values of β that were actually present during the tests.

Figure 22 shows electron photomicrographs of three samples taken from the flowing carbon dispersion after various amounts of aerodynamic shear had been applied to them. The samples were taken by passing an electron microscope grid through the flowing dispersion at a position about 1.0 in. above the exit plane

(Fig. 19). Figure 22(a) is a sample taken with no orifice present. In Figs. 22(b) and 22(c), the dispersion passed through 0.040-in.-dia and 0.020-in.-dia orifices, respectively. The sequence of photographs shows a trend toward decreasing agglomerate size. The size of the particles shown in Fig. 22(c) is about the same as those shown in Refs. 11 and 12 and is about the same as the nominal particle diameter of 0.012 in.

Values of dispersed carbon mass attenuation coefficient of up to 50,000 cm^2/g have been reported in Refs. 11 and 12. However, these were over a limited wavelength range (0.1 to 0.6 microns) in the region at which the mass attenuation coefficient for micron-sized particles is a maximum with respect to the wavelength of the absorbed radiation. The wavelength-average mass attenuation coefficient reported here includes the attenuation of long wavelength light (> 1.0 microns). This has the effect of lowering the average value of mass attenuation coefficient over the wide wavelength range. This accounts in part for the average value being lower than the values of Refs. 11 and 12.

Figure 23 shows the fraction of the incident radiation absorbed, η_A, versus the seed density parameter, $\rho_s \ell$, with β as a parameter. The fraction absorbed during these tests ranged from about 0.97 to 0.04, with many of the β values equal to or greater than the values of 5000 cm^2/g used for the reference nuclear light bulb design. For a few tests, both the seed density parameter and the value of β were about the same as for the nuclear light bulb engine.

It remains to be seen whether or not particle reagglomeration will cause the mass attenuation coefficient to decrease as the seeded gas flows through a complicated passage such as the propellant heating inlet geometry. However, these data show that the potential exists for an increase in β by a factor of 5 or more relative to the values that existed in the hot-flow experiments reported in the next section.

SECTION IV

DISCUSSION OF HOT-FLOW TESTS

Objectives

The objectives of the hot-flow tests are to absorb as much as possible of the radiation incident on the propellant stream and to use this absorbed energy to attain a high simulated-propellant exit temperature. Ideally, these tests should be conducted in a geometry similar to the propellant duct of a nuclear light bulb engine (see Fig. 2). In addition, the geometry used should provide minimum seed deposition on the transparent wall of the simulated-propellant duct.

Test Configuration

Figure 3 is a sketch of the basic d-c arc radiant energy source and propellant heater assembly used in the tests. The d-c arc source is described in Section II. The configuration for which the buffer layers reduced the simulated-propellant duct wall coating to a minimum in the cold-flow tests (Section III) was used for the hot-flow tests. The propellant duct consists of an annulus formed by two sets of concentric, water-cooled, fused silica tubes (see Fig. 16). The inner diameter of the annulus was 1.69 in., the outer diameter was 3.54 in., and the duct test section length was 5.0 in. The seed flow was introduced into the test section through a 0.118-in.-wide annular slot. The buffer layers of unseeded argon were introduced on both sides of the central seeded stream through 0.394-in.-wide annulii. After passing through the 5-in., test section, the simulated propellant stream was ducted through an exhaust system at atmospheric pressure (see Fig. 3). For hot-flow tests, a water-cooled exhaust calorimeter was installed directly above the exit of the test section. For some of the tests the calorimeter was used to measure the power absorbed in the seeded simulated propellant exhaust. In addition, various types of shielded and unshielded thermocouples were positioned immediately downstream of the 5-in. test section and centrally located in the annulus for measuring local temperatures. To aid in smoothing the velocity profiles and to provide improved flow uniformity at the propellant duct test section inlet plane, porous foam material (45 ppi) was placed at the locations designated X through Z in Fig. 16.

Cold-flow tests using the above inlet geometry indicated negligible wall coating when the buffer layer and seed gas injection velocities were matched at 5.0 ft/sec at the propellant duct test section inlet plane. Consequently, in the hot-flow tests, the average velocities of three parallel streams at the test section inlet plane were approximately 5.0 ft/sec. The completely assembled hot-flow geometry was tested

cold before use with the d-c arc heater. Figure 24 is a photograph of one of these tests. The test conditions were as described above. The porous foam at location Z in Fig. 24 is shown. The seeded gas flow is seen separated from the outer propellant duct wall by a layer of unseeded argon.

Test Procedures

D-C Arc

The following sequency of events was used during a typical test: (1) start motor-generators, (2) turn on all diagnostic and recording equipment, and set the zero-references, (3) turn on exhaust vent systems, cooling water, and gas flow and adjust to the desired operating conditions, (4) index the auxiliary starting electrode until it contacts the cathode, (5) activate the auxiliary starter system, (6) record all data at a particular test condition, and (7) turn off arc power after completion of run.

Simulated Propellant Flow

The argon flow rates for the two buffer flows and the seed carrier flow were turned on and adjusted. The seed carrier flow was initially set for full argon carrier bypass of the high-pressure seed canister (see Fig. 15). The agitator blades were started rotating, and the argon was then bled through the chamber to initiate the carbon seed flow to the test section. At the end of the test the argon bypass valve was opened and the flow through the canister turned off.

Test Sequence

For each test, preparations for starting the d-c arc were made (steps 1-4 above). The gas flows for the simulated propellant stream were turned on and adjusted. The recording equipment was activated, and the d-c arc started. After steady-state conditions were reached, the measurements of the water and gas inlet and exit temperatures, the radiation to the radiometer, and the arc current and voltage were recorded (the "before" condition). Then the seed flow was started and adjusted for the desired level of attenuation. After steady-state conditions were reached, the test conditions were again recorded (the "during" condition). The seed flow was then stopped and again recordings were made when steady-state conditions were reached (the "after" condition). This procedure was used for the tests where all the above data were recorded. As discussed in the following subsection, for some tests, only radiation attenuation measurements were made before, during, and after seeds were flowing. The average carbon seed weight flow rate was estimated by measuring the total test time during which seeds were flowing, and by weighing the carbon in the seed dispersal system before and after the test was conducted. The argon weight flow was 0.030 lb/sec (see Table I) and seed

weight flow was estimated to range between 5 and 16 percent of the argon weight flow (a value of 10 percent, or 0.003 lb/sec, was used in reducing the data).

Results of Hot-Flow Propellant Heating Experiments

Radiation, Thermocouple and Calorimeter Measurements

Hot-flow tests were conducted at increasing d-c arc radiant energy levels, and increasing simulated propellant radiation attenuation levels. High-speed color movies of several hot-flow tests were also taken to provide information on the hot-flow fluid mechanics phenomena. Analysis of portions of the film indicated distinct axial streamer formation and some axial acceleration as the streamers flowed upward. In all the hot-flow tests, an aperture was placed between the radiometer and test section. The radiometer viewed a 1.0-in. x 1.26-in. rectangular area of the test section location about 2.5 in. downstream of the inlet foam (see Figs. 3 and 9). Figure 25 illustrates the results from one typical hot-flow propellant heating test. Figure 25(a) is a sequence of photographs of the test section and d-c arc source taken before, during, and after the seeded stream was flowing. All the photographs were taken using Polaroid Type 57 (ASA 3000) film at f/32 aperture setting and 1/200-sec shutter speed with a 3.0 neutral density filter. Streamers noted in the cold-flow tests are barely visible in the middle photograph.

Figure 25(b) is the corresponding radiometer trace. The percent radiation transmitted is determined by the ratio of the total radiation transmitted through the test section with seeds flowing divided by the total radiation transmitted through the test section without seeds flowing. As indicated in Figure 27(b) the seed flow was initiated approximately 10 sec after the arc was initiated. The seed flow was then adjusted for approximately 35-percent radiation transmission as measured by the radiometer. After about 68 sec, the seed flow was turned off and the radiometer trace returned to within 1 percent of the value at the start of this test. In hot-flow tests, the percent radiation transmitted through the seeded simulated propellant in the test section ranged from 5 percent (a large amount of absorption) to 95 percent. After the tests with large seed flow rates, the radiation transmitted through the test section returned to within 2 percent of the initial value. The fluctuations in the radiometer output as illustrated in Figure 25(b) during seed operation was typical of the test results and are attributed to fluctuations in the seed flow.

Figure 25(c) shows the test conditions and results corresponding to the photographs and radiometer trace in Figs. 25(a) and (b). The local temperature measured using an aspirating radiation-shielded type chromel/alumel thermocouple (see Figs. 13 and 14) was 1930 R at a point approximately mid-radius in the propellant duct exit. This thermocouple was in the axial position (see Fig. 12).

The bulk temperature at the propellant duct exit determined from calorimetric measurements (including the exhaust gas calorimeter, exhaust vent, and other associated water-cooled components) was 1169 R (see Section II for calorimeter description). This is about 40 percent less than the local temperature measured with the thermocouple at a point halfway across the propellant annulus at the exit plane. The local temperature distribution across the exit plane of the propellant duct is not known and may not necessarily be symmetric. Therefore, the temperature measured by the thermocouple is not necessarily the maximum local temperature in the seeded propellant stream. The value of the bulk temperature at the propellant duct exit for this case, as determined from the radiation attenuation measurements, was 1335 R. This is in reasonable agreement with the calorimetric measurement (1169 R).

Figure 26 shows the calorimetric energy balance corresponding to the test conditions shown in Fig. 25(c). The power distributions before, during and after seeds were flowing are shown for the various components included in calorimetric determination of the simulated propellant bulk exit temperature. The change in power with seeds flowing for the various components is also shown. The absorbed power change of the components which contact the hot propellant stream is approximately balanced by the decrease in radiation transmitted through the simulated propellant duct to the radiometer.

Figure 27 summarizes data from the hot-flow propellant heating tests. The propellant stream bulk exit temperature at the end of the 5-in. test section is shown versus the total radiation incident on the propellant stream in the test section. The solid lines are lines of constant fraction of the total incident radiation that is transmitted through the seeded propellant stream.

Limitations in Measurement Techniques

It is important to understand the uncertainties in the data shown in Fig. 27 resulting from limitations of the measurement techniques available when these tests were made. At temperatures up to about 2000 to 2500 R, the radiometer, exhaust-gas calorimeter, and thermocouple measurements bore a consistent relation to each other. At higher temperatures, the thermocouples and exhaust-gas calorimeter could no longer be used. Attempts were made to use tungsten/tungsten-rhenium thermocouples (rated for usage up to about 4600 R); however, no meaningful measurements could be obtained, due in part to their brittleness and inability to remain intact in the particle-laden stream (some chemical reaction with the hot carbon particles may have also introduced errors). Several other thermocouples, including an eroding-junction type, were also tried (see Fig. 13). The exhaust-gas calorimeter was also unusable at these higher temperatures because the arc could be operated only for short run times (less than 15 sec) due to fused silica tube cooling limitations; hence, insufficient time was available during a run for complete steady-state conditions to be reached. Further development of these measurement techniques is needed for future propellant heating tests where higher temperatures are expected. A preliminary investigation aimed at development of improved measurement techniques

for hot argon streams seeded with carbon particles was initiated. The results of these preliminary tests are discussed in Appendix D.

Temperature Calculations, Comparisons, and Sources of Possible Error

In view of the measurement technique limitations at the higher temperatures, all data in Fig. 27 were reduced using the radiometer measurements. Referring to Fig. 27, measurements to determine the total radiation incident on the propellant stream were relatively straightforward; hence, the locations of the data point along the abscissa are believed to be quite accurate. The locations along the ordinate --- the propellant bulk exit temperature --- were calculated in the following manner. First, the total amount of radiation absorbed in the simulated propellant stream was determined from the radiometer measurements at the location shown in Fig. 3 with or without the seeds flowing. It was assumed that the fraction of radiation absorbed was constant over the entire 5-in. test section. Losses due to absorption in the fused silica tubes and in the cooling water were taken into account, and it is believed that the resulting values of radiation absorbed in the propellant stream were fairly accurate. Next, a propellant bulk temperature rise was calculated, assuming that the enthalpy increase was equal to the absorbed radiation minus an estimate of heat lost to the duct walls (3 to 5 percent of the absorbed radiation for these tests).* The calculation neglected losses due to reradiation from the hot propellant. It did, however, take into account the variation of the specific heat of carbon with temperature (from about 0.12 at the inlet temperature to about 0.48 Btu/(lb-deg R) at 4000 R; the corresponding increase in the total specific heat of all argon and carbon flowing in the propellant duct is about 20 percent). This calculated bulk temperature rise was then added to the inlet temperature (530 R) to obtain the propellant bulk exit temperature shown on Fig. 27. As indicated by the symbol key, different symbols indicate various ranges of radiation transmitted. Several other assumptions of secondary importance were made, all of which were "pessimistic" (leading to underestimation of bulk temperature) in nature.** This procedure, then, was used in plotting the data shown with open symbols and calculating the lines of constant fraction of radiation transmitted.

Calculations of the bulk exit temperature were made using a simplified computer model of the heated flow in the duct from the inlet to the exit with an estimate of the reradiation lost from the simulated propellant stream. It is assumed in this

---

* This calculation probably overestimated the heat lost to the walls since the temperature in the flow at the wall was assumed to be the bulk temperature.

**One assumption was that reradiation from the propellant did not affect the radiometer measurement used to determine the amount of incident radiation absorbed by the propellant. This assumption is reasonable considering all factors (the temperature at the station where the radiometer measurements are made, the spectral distribution of the reradiation, the fused-silica and cooling water cut-offs, etc.)

model that the propellant stream reradiates like a black body at the local bulk temperature. As in the previous calculation, an estimate of the convective heat loss to the duct walls was included, assuming that the temperature in the flow at the wall was the local bulk temperature. Specific results for the three highest power data points are shown by the solid symbols in Fig. 27. A more detailed discussion of the way in which the simulated propellant bulk exit temperature was determined from the radiometer measurements is given in Appendix B. Insufficient information is presently available to evaluate the accuracy of this reradiation correction. There are two reasons why this correction might be too large. First, the effect of the reflectivity of the lower part of the calorimeter housing which shrouds the upper portion of the test section (see Fig. 3) on the bulk exit temperature was not included in the above calculations. This reflectivity would result in a decrease in the net radiation loss from the propellant and an increase in the propellant stream exit temperature above that is shown in Fig. 27 (solid symbols). Second, the seed weight flow rate may have been greater than 10 percent of the argon weight flow rate for the tests with low transmission through the seeds. This could produce a large number of optical path lengths in the propellant stream. This would mean that the effective reradiating temperature might be considerably less than the bulk temperature, which would also result in an overestimate of the radiation correction. However, it is possible that the temperature of the seeded portion of the stream is greater than the bulk temperature; this would lead to an underestimation of radiation losses and an overestimation of convected bulk temperature. In separate tests discussed in Appendix D, measurements were made on a seeded stream in which the resulting equivalent black-body radiating temperature was about the same as the bulk temperature.

Based on the results presented in Fig. 27 and the previous discussion, it is concluded that the highest propellant bulk exit temperatures achieved were between approximately 3000 to 4000 R. Based on thermocouple measurements at lower temperatures, it is inferred that local temperatures in the duct are substantially higher than the bulk temperatures.

Figure 28 shows a plot of the local simulated propellant exit temperature measured by thermocouple versus the radiation incident on the propellant stream. The upper bound for thermocouple measurements indicated by the dashed line on Fig. 27 is shown here for comparison. The very high data point is a value for which a high radiation error is suspected; therefore, the line is drawn as shown. Figure 29(a) is a plot of the local temperature measured by the thermocouple versus the radiation absorbed by the propellant stream. The solid line corresponds to the variation of calculated bulk exit temperature with radiation absorbed. The location of this line was calculated in the same manner used for the determination of the bulk exit temperature based on the radiometer measurements discussed above. The results show that the temperatures corresponding to points with η_T less than 0.20 fall below the bulk temperature while those with larger fractions of radiation transmitted correspond to those data points above the bulk temperature.

Local temperature measurements are difficult using thermocouples in a high-temperature, low velocity seeded gas stream. These difficulties are further aggravated by the partial exposure of the thermocouple to a high intensity radiation field. The radiation effect is further complicated by the fact that the presence of streamers and fluctuations in the seed flow could change the local seed density near the thermocouple during each test.

Figure 29(b) summarizes the factors that may affect temperature measured using thermocouples. The low velocity gas stream results in a thermal boundary layer which causes the temperature at the thermocouple junction to differ from that of the free-stream gas temperature T_W. Coating of the thermocouple by solid seed particles changes the heat transfer to the thermocouple. In particular, coating of the thermocouple junction alters the response time and the accuracy of the thermocouple temperature measurement. Carbon coating of the thermocouple junction would probably cause the temperature indicated by the thermocouple to be lower than the local gas temperature, and would also cause an increase in response time. Various amounts of thermocouple coating were observed to have occurred during the simulated propellant heating tests. As shown in Fig. 29(a) for the tests with low radiation transmission (heavy seed flow), the thermocouples read lower than the bulk temperature. Perhaps for these tests the error caused by seed coating was large enough to cause the low measurements. The immersion length of the thermocouple stem into the gas stream also affects the accuracy of the thermocouple measurement. For a gas as hot as the simulated propellant stream, heat conduction along the stem can cause large errors in the local temperature measurements by thermocouple. This type of error would cause a low thermocouple reading. Stem heat conduction errors can be reduced by having a long stem immersion length (L/D > 40); for this reason, the axial thermocouple was used in most of the tests (see Fig. 12).

The exposure of the thermocouple junction to radiation also causes an error in the gas temperature measured by the thermocouple. The error caused by radiation heat transfer is complicated by the effect of reradiation from the thermocouple to its surroundings, and by the effect that seed coating would have on the absorption and emmission characteristics of the thermocouple. Figure 30 illustrates the effect of radiation on the thermocouple measurement. It will help to put the results shown in Fig. 30 in perspective by discussing some of the limiting values that the ordinate of the graph could have for various seeded gas optical thicknesses and radial positions. For a uniform temperature, optically thin (approaching transparent) flowing gas transmitting radiation, the temperature remains uniform (neglecting boundary layer effects) as it flows through the radiation field. At the other extreme an optically thick gas has a linear temperature profile, highest on the side with the incident radiation and lowest on the side away from the incident radiation. Returning to Fig. 30 for the optically thin case ($\eta_T \rightarrow 1$) the ordinate should approach zero as the fraction transmitted (abscissa) approaches 1. This is because any local measurement will approach the bulk temperature, since in the limit, the temperature is uniform. For the optically thick case ($\eta_T \rightarrow 0$), if the lowest temperature is taken to be 530 R it can be shown that the ordinate could range from about -0.85, if the thermocouple measured the local temperature on

the unheated side, to about +1.125, if the thermocouple measured the local tempera-ture on the heated side of the seeded stream. Therefore, an envelope containing all possible points on this plot would converge toward zero at $\eta_T = 1.0$ from either +1.125 or -0.85 and $\eta_T = 0$. The trend of the points is clearly not toward zero as $\eta_T \rightarrow 1.0$ as it should be ideally. This is interpreted as being due to increasing radiation errors as the transmission of the simulated propellant stream increases. The important point from Fig. 30 is the consistent trend. The location of the points at low and intermediate transmission is plausible in light of the above discussion. The entire set of thermocouple data is subject to all the errors dis-cussed; however, the radiation error seems to become dominant as the transmission increases.

Figure 31 is a comparison of the simulated propellant bulk exit temperature measured by the calorimeter with the calculated bulk exit temperature. These data are plotted versus the radiation absorbed as measured by the radiometer. Most of the bulk temperatures as measured by the calorimeter are below the solid curve. The agreement is fairly good; most of the points fall within 25 percent of their calculated curve. The calorimeter is subject to losses by conduction and convection. Also the thermocouples measuring the water cooling exit temperatures were located as close to the exit of the calorimeter as was practical.

However, in some cases several feet of connecting hose was present between the thermocouple and the calorimeter elements water cooling exit. Thus, some energy could be lost in these hoses, resulting in the low temperatures obtained.

Figure 32 is a plot of the fraction of the radiation attenuated by the sim-ulated propellant stream versus the radiation attenuation parameter . The fraction of the radiation absorbed ranges from 0.96 to 0.03. The design value for the nuclear light bulb engine, as shown as the solid triangular symbol, is 0.95. The radiation attenuation parameter was calculated from the relationship shown in Fig. 32.

Summary and Conclusions

In terms of the objectives of this portion of the program, the propellant heating results using the d-c arc source are encouraging. Simulated propellant bulk exit temperatures in the range of 3000 to 4000 R have been obtained, with the buffer layer flows successfully minimizing the coating of the duct wall by the carbon seed. The maximum power at which the arc was operated in these tests was determined by partial vaporization of the foam at the inlets and by cooling limita-tions on the fused silica tube adjacent to the arc column. For future tests, the arc source will be operated at higher power for shorter run times (several seconds) and will provide greater than 100 kw of radiant energy. By using higher arc powers and making use of the increased mass attenuation coefficients that have been demon-strated, it should be possible to obtain significant increases in the bulk exit temperatures relative to those reported herein. Current estimates indicate that bulk exit temperatures approaching 6500 R are attainable within the next year.

Further development of measurement techniques to determine the heat content and local temperature of hot, low velocity, seeded gas streams is required, particularly for use in the temperature range from 4000 to 7000 R. Possible techniques for consideration include shielded aspirating thermocouples, a fast response-time calorimeter, and various types of sampling probes. No evidence has been found in tests to date which would prevent attainment of a bulk exit temperature equal to that in the reference engine after development of the required test equipment.

REFERENCES

1. McLafferty, G. H.: Investigation of Gaseous Nuclear Rocket Technology --
    Summary Technical Report. United Aircraft Research Laboratories Report
    H-910093-46, prepared under Contract NASw-847, November 1969.

2. McLafferty, G. H.: Survey of Advanced Concepts in Nuclear Propulsion. Journal
    of Spacecraft and Rockets, Vol. 5, No. 10, October 1968.

3. McLafferty, G. H. and H. E. Bauer: Studies of Specific Nuclear Light Bulb
    and Open-Cycle Vortex Stabilized Gaseous Nuclear Rocket Engines. United
    Aircraft Research Laboratories Report F-910093-37, prepared under Contract
    NASw-847, September 1967. Also issued as NASA CR-1030.

4. Krascella, N. L: Theoretical Investigation of the Absorption and Scattering
    Characteristics of Small Particles. United Aircraft Research Laboratories
    Report C-910092-1, prepared under Contract NASw-847, September 1964. Also
    issued as NASA CR-210.

5. Krascella, N. L.: Theoretical Investigation of the Absorptive Properties of
    Small Particles and Heavy-Atom Gases. United Aircraft Research Laboratories
    Report E-910092-7, prepared under Contract NASw-847, September 1965.

6. Marteney, P. J., N. L. Krascella and W. G. Burwell: Experimental Refractive
    Indices and Theoretical Small-Particle Spectral Properties of Selected Metals.
    United Aircraft Research Laboratories Report D-910092-6, prepared under
    Contract NASw-847, September 1965.

7. Marteney, P. J. and N. L. Krascella: Theoretical and Experimental Investigations
    of Spectral Opacities of Mixtures of Hydrogen and Diatomic Gases. Air Force
    Systems Command Report RTD-TDR-63-1102, prepared by United Aircraft Research
    Laboratories under Contract AF 04(611)-8189, November 1963.

8. Krascella, N. L.: Tables of the Composition, Opacity, and Thermodynamic
    Properties of Hydrogen at High Temperatures. United Aircraft Research
    Laboratories Report B-910168-1, prepared under Contract NAS 3-3382,
    September 1963. Also issued as NASA SP-3005.

9. Lanzo, C. D. and R. G. Ragsdale: Experimental Determination of Spectral and
    Total Transmissivities of Clouds of Small Particles. NASA Technical Note
    D-1405, September 1962.

10. Lanzo, C. D. and R. G. Ragsdale: Heat Transfer to a Seeded Flowing Gas from
    an Arc Enclosed by a Quartz Tube. NASA Technical Memorandum X-52005, June 1964.

REFERENCES (Continued)

11. Marteney, P. J.: Experimental Investigation of the Opacity of Small Particles. United Aircraft Research Laboratories Report C-911092-2, prepared under Contract NASw-847, September 1964. Also issued as NASA CR-211.

12. Williams, J. R., J. R. Clement, A. S. Shenoy and W. L. Partain: The Attenuation of Radiant Energy in Hot Seeded Hydrogen - An Experimental Study Related to the Gaseous Core Nuclear Rocket. Quarterly Status Report No. 2, NASA Research Grant NGR-11002-068, prepared by Georgia Institute of Technology, February 1969.

13. Mie, G.: Annalen der Physik, Vol. 30, 1919.

14. Bauer, H. E., R. J. Rogers and T. S. Latham: Analytical Studies of Start-Up and Dynamic Response Characteristics of the Nuclear Light Bulb Engine. United Aircraft Research Laboratories Report J-910900-5, prepared under Contract SNPC-70, September 1970.

15. Roman, W. C., J. F. Klein and P. G. Vogt: Experimental Investigation to Simulate the Thermal Environment, Transparent Walls and Propellant Heating in a Nuclear Light Bulb Engine. United Aircraft Research Laboratories Report H-910091-19, prepared under Contract NASw-847, September 1969.

16. Johnson, B. V.: Exploratory Experimental Study of the Effects of Inlet Conditions on the Flow and Containment Characteristics of Coaxial Flows. United Aircraft Research Laboratories Report H-910091-21, prepared under Contract NASw-847, September 1969.

17. Roman, W. C.: Experimental Investigation of a High Intensity R-F Radiant Energy Source to Simulate the Thermal Environment in a Nuclear Light Bulb Engine. United Aircraft Research Laboratories Report J-910900-4, prepared under Contract SNPC-70, September 1970.

18. Aden, A. L.: Electromagnetic Scattering from Spheres with Sizes Comparable to the Wavelength. Journal of Applied Physics, Vol. 22, No. 5, May 1955.

19. Van der Hulst, H. C.: Light Scattering by Small Particles. John Wiley and Sons, New York, 1957.

20. Williams, J. R., A. S. Shenoy, W. L. Partain and J. D. Clement: Thermal Radiation Absorption by Particle-Seeded Gases. AIAA Paper No. 70-838, presented at Fifth Thermophysics Conference, Los Angeles, California, June 29 - July 1, 1970.

21. McLafferty, G. H.: Studies of Coolant Requirements for the Transparent Walls of a Nuclear Light Bulb Engine. United Aircraft Research Laboratories Report F-110224-6, March 1967.

35

REFERENCES (Continued)

22. Hirschfelder, J. O., C. F. Curtiss and R. B. Bird: Molecular Theory of Gases and Liquids. John Wiley & Sons, Inc., London, 1954.

LIST OF SYMBOLS

A	Area, ft^2
$b_{a,\lambda}$	Monochromatic mass absorption coefficient, cm^2/g
$b_{e,\lambda}$	Monochromatic mass extinction coefficient, cm^2/g
$b_{s,\lambda}$	Monochromatic mass scattering coefficient, cm^2/g
$\bar{b}_a$	Total absorption coefficient, cm^2/g
C_p	Specific heat of simulated propellant mixture, Btu/lb
H	Width of propellant duct, ft
H_p	Simulated propellant enthalpy, Btu/sec or kw
I_A	Arc current, amp
I_λ	Monochromatic intensity, kw/cm^2 - ster
$I_{o,\lambda}$	Incident monochromatic intensity, kw/cm^2 - ster
$K_{a,\lambda}$	Monochromatic absorption coefficient, cm^{-1}
$K_{e,\lambda}$	Monochromatic extinction coefficient, cm^{-1}
K_λ	Monochromatic attenuation coefficient, cm^{-1}
$K_{s,\lambda}$	Monochromatic scattering coefficient, cm^{-1}
L	Axial length along propellant duct, ft
ℓ	Radiation path length, cm
$\dot{M}_A$	Argon weight flow rate, lb/sec or g/sec
$\dot{M}_p$	Total simulated propellant weight flow, lb/sec or g/sec
P_o	Orifice pressure drop, psi
Pr	Prandtl number, dimensionless
Q_A	Total radiation absorbed by propellant stream, Btu/sec or kw

LIST OF SYMBOLS (Continued)

Q_I	Total radiation incident on propellant stream, Btu/sec or kw
Q_R	Power radiated, Btu/sec or kw
Q_{RR}	Heat reradiated, Btu/sec or kw
Q_W	Heat loss to propellant duct wall, Btu/sec
R/R_W	Dimensionless radial position
Re	Reynolds number, dimensionless
r	Seed diameter, cm
St	Stanton number, dimensionless
T	Time, sec
T_B	Bulk temperature, deg R
T^*_{BB}	Equivalent black body radiating temperature, deg R
T_{CAL}	Simulated propellant bulk exit temperature using calorimeter, deg R
T_E	Simulated propellant bulk exit temperature using radiometer, deg R
T_G	Gas temperature, deg R
T_L	Local temperature, deg R
$T_{p,ns}$	Temperature measured with optical pyrometer without seeds, deg R
$T_{p,s}$	Temperature measured with optical pyrometer with seeds, deg R
T_{TC}	Local simulated propellant exit temperature, deg R
T_W	Wall temperature, deg R
V_A	Arc voltage, v

LIST OF SYMBOLS (Continued)

Z   Axial position, ft

β Total absorption coefficient determined from experiments, cm^2/g

Δw Seed weight change, g

η_A Fraction of radiation absorbed, dimensionless

η_T Fraction of radiation transmitted, dimensionless

λ Wavelength, microns

ρ_A Argon density, g/cm^3

ρ_S Seed density, g/cm^3

σ Stefan-Boltzman constant, $Btu/sec\text{-}R\text{-}ft^2$

APPENDIX A

OPTICAL PROPERTIES OF PARTICLE CLOUDS

In traversing an absorbing-scattering medium, such as a cloud of particles, a beam of radiant energy is attenuated due to absorption and scattering. Absorption is the removal of energy from the beam by dissipative processes within the medium. Scattering in this discussion includes the combined processes of reflection, refraction, and diffraction.

The fractional decrease in the intensity of a monochromatic beam, I_λ, is proportional to the distance traveled by the beam, $d\ell$, or

$$\frac{d I_\lambda}{I_\lambda} = - K_\lambda \cdot d\ell \qquad (A-1)$$

In the absence of scattering, the constant K_λ is defined as the attenuation coefficient, $K_{a,\lambda}$; in the absence of absorption it is defined as the scattering coefficient, $K_{s,\lambda}$. If both absorption and scattering take place in the medium, then the K_λ is defined as the total attenuation and extinction coefficient, $K_{e,\lambda}$ and is equal to the sum of $K_{s,\lambda}$ and $K_{a,\lambda}$.

The characteristics of an absorbing and scattering medium can be expressed in terms of the monochromatic mass extinction coefficient $b_{e,\lambda}$, where $b_{e,\lambda}$ is the sum of $b_{a,\lambda}$ and $b_{s,\lambda}$, the monochromatic mass absorption and scattering coefficients, respectively. Equation (A-1) can be integrated if the medium is homogeneous:

$$I_\lambda = I_{0,\lambda} \exp \left[-\rho_S (b_{a,\lambda} + b_{s,\lambda}) \ell \right] \qquad (A-2)$$

where $I_{0,\lambda}$ is the intensity of a beam of radiation incident on the particle cloud, I_λ is the intensity of the beam of radiation leaving the particle cloud (in the same direction as $I_{0,\lambda}$), ρ_S is the density of the dispersed seed material, and ℓ is the radiation path length through the cloud.

Particles of different sizes have different values of scattering and absorbing properties at the same wavelength of radiation, and the same size particles have varying properties for each wavelength of radiation. The attenuation of radiation by solid particles may be calculated theoretically using Maxwell's equations. The solution depends on the following dimensionless quantities: the ratio of the characteristic particle dimension to the wavelength of the radiation, the complex refractive index, and the particle shape. The rigorous solution of Maxwell's

equations for the case of a plane wave incident on a homogeneous spher was obtained by Mie (Ref. 13). A transformation of the basic Mie equations to a form suitable for machine calculations is given in Ref. 18. This transformation was used in Ref. 4 to calculate the optical properties for spherical particles as a function of the radiation wavelength and particle radius for fifteen types of small spherical particles.

Materials such as tungsten and carbon are of interest as seed materials in the nuclear light bulb engine research program. Experimental measurements of the absorption and scattering characteristics of clouds of these materials have been reported in Refs. 9 through 12.

In the absence of optical interference between particles, the monochromatic mass absorption coefficient and the monochromatic mass scattering coefficient are the sum of the contributions of particles of a given size; therefore,

$$\overline{b}_{a,\lambda} = \frac{1}{\rho_s} \int_0^\infty \rho_s(r) b_{a,\lambda}(r)\, dr \tag{A-3}$$

and

$$\overline{b}_{s,\lambda} = \frac{1}{\rho_s} \int_0^\infty \rho_s(r) b_{s,\lambda}(r)\, dr \tag{A-4}$$

where $\rho_s(r)$ is the density of particles of radius r and $b_{a,\lambda}(r)$ and $b_{s,\lambda}(r)$ are the monochromatic mass absorbing and scattering coefficients for each size particle. The conditions under which optical interference between particles can be neglected has been cited as a center-to-center separation distance on greater than three particle radii (Ref. 19).

The monochromatic extinction of a cloud of different-sized particles can be expressed as

$$I_\lambda = I_{0,\lambda} \exp\left[-\rho_s\, b_{e,\lambda}\, \ell \right] \tag{A-5}$$

The total extinction can be expressed as

$$I = \int_0^\infty I_{0,\lambda} \exp\left[-\rho_s \overline{b}_{e,\lambda}\, \ell \right] d\lambda \tag{A-6}$$

As discussed previously, the loss of radiant energy from a beam of radiant energy transmitted through a medium is equal to sum of losses due to absorption and scattering. If the radius of particles in the medium are of the order or larger than the wavelength of the light passing through the medium, most of the radiation is scattered in the forward direction (Ref. 20). This scattered radiation can be considered to be part of the radiation actually transmitted. Thus, the attenuation is primarily due to absorption within the medium, and

$$I = \int_0^\infty I_{0,\lambda} \exp\left[-\rho_s b_{a,\lambda} \ell\right] d\lambda \qquad (A-7)$$

If $b_{a,\lambda}$ is independent of wavelength, then Eq. (A-7) can be integrated to obtain

$$\frac{I}{I_0} = \exp\left[-\rho_s \overline{b}_a \ell\right] \qquad (A-8)$$

For the tests discussed in Section III, which were directed at increasing the mass attenuation coefficient β, Eq. (A-8) was used to calculate β from the measurements made. The measurements were of the ratio I/I_0, the seed density ρ_s and the path length ℓ. I/I_0 was obtained by measuring the radiation reaching a radiometer with and without seeds flowing (Fig. 3). Refer to Section III for a discussion on the test setup. The path length was assumed to be the width of the seed flow duct.

Figure 20 is a typical data trace of the light transmitted to the radiometer. The fluctuation of the trace was accounted for in the following manner: (1) it was assumed that the value of β was constant during each test, that the seed volume flow rate was the same as the argon volume flow rate, and that the seed flow was homogeneous; (2) subject to these assumptions, fluctuations in the data trace are due only to changes in seed density. The seed density as a function of time is then

$$\rho_s(t) = \ln\left[\frac{I(t)}{I_0}\right] \frac{1}{\ell\beta} \qquad (A-9)$$

This can be related to the total amount of seed and the β to be solved for, yielding the following expression:

$$\beta = \frac{\dot{M}_A}{\Delta W \ell \rho_A} \int_0^t \ln\left[\frac{I(t)}{I_0}\right] dt \qquad (A-10)$$

where $\dot{M}_A$ is the argon carrier weight flow (held constant during each test), ΔW is the mass of seed used, ρ_A is the argon density, and t is the test time. The integral was evaluated numerically using Simpson's rule, and the value of β calculated. As discussed in Section III, the maximum value of β was 16,362 cm^2/g.

APPENDIX B

CALCULATION OF SIMULATED PROPELLANT
STREAM BULK EXIT TEMPERATURE

As discussed in Section IV of this report, the response of the thermocouples and the calorimeter was not fast enough to be compatible with high-power, short-run-time operation of the d-c arc. High power testing with long run times (greater than 6 sec) was not possible without risk of damage to the test equipment, due to water-cooling limitations of the inner fused silica walls (see Fig. 3). Accordingly, for the high power tests, the amount of power deposited in the simulated propellant stream was determined from radiation attenuation measurements. As shown in Fig. 3, the radiometer viewed a 1.0-in.-high by 1.26-in.-wide portion of the test section. The center of this viewed portion was 2.5 in. from the beginning of the 5-in.-long test section. Based on the radiation calibration measurements, the total radiation incident on the simulated propellant stream was measured with the radiometer before seeds were flowing, while seeds were flowing, and for most tests, after seeds were flowing. The amount of radiation attenuated by the propellant stream, η_A, was obtained from these radiometer measurements. The radiation attenuation can be attributed to absorption, since particle clouds similar to those used as the simulated propellant have been shown to scatter light mainly in the forward direction (Refs. 19 and 20).

Interpretation of the radiation attenuation measurements is complicated by the presence of streamers of dense seed flow separated by regions of lighter seed flow (Fig. 18). The radiometer measurements, therefore, yield an average value of η_T in the region viewed. For the tests with heavy seed flows, fractions absorbed of up to 0.96 were obtained. This corresponds to an average optical thickness of about 3 for the simulated propellant stream. Due to the presence of streamers, this means that there must have been regions of much higher optical thickness ($\gg 3$) within the streamers, while between them there were regions of lower optical thickness. For very heavy seed flows (large η_A), it was observed that the propellant flow was made up of wide streamers, with narrow regions of lighter seed flow separating them. Therefore, under the conditions of heavy seed flow, most of the radiation transmitted through the simulated propellant probably came through in the narrow regions of lighter seed flow, while the regions of heavy seed flow attenuated essentially all the radiation incident on them.

If the cloud of particles in the simulated propellant stream was homogeneous, one would expect the absorption by the seeded gas to decrease as the flow was heated, because thermal expansion would cause the gas and seed density to decrease. However, in accordance with the above discussion, it appears that the simulated propellant stream was not homogeneous and that most of the transmission through the simulated propellant was in the regions of lighter seed flow. In this case the effect of expansion of the gas due to heating might decrease the local seed density.

But since it was very high to begin with in the streamers, this expansion may not have increased the transmission through the streamers appreciably. Thus, the total change in transmission of the simulated propellant, due to density changes, is dependent upon how much of the seed flow is filled with streamers. The concern about the possible decrease of absorption due to thermal expansion of the heated gas is greatest for those tests in which large temperature rises occurred. However, the largest temperature rises were obtained for tests with heavy seed flows (large attenuation) and, therefore, heavy streamers. In light of the above discussion, the attenuation measured at the central portion of the propellant duct is considered to be representative of the average attenuation along the entire test-section length.

The measured attenuation was used to calculate the amount of radiation absorbed by the propellant stream. The amount of radiation absorbed was calculated by expressing the attenuation as a fraction of the incident radiation absorbed, η_A, and multiplying the total measured radiation incident on the propellant stream η_A. The simulated propellant stream temperature rise was then calculated based on this amount of total radiation absorbed. Of the radiation absorbed, some serves to increase the enthalpy of the simulated stream, some is lost to the propellant duct walls, and if the temperature is high enough, some is lost be reradiation from the propellant stream. The simulated propellant exit temperature was calculated by two methods. The first method included only the effects of the absorbed radiation on the simulated propellant enthalpy rise and an estimate of the heat loss to the duct walls. The second method included an estimate of the energy lost by reradiation. The heat lost to the duct walls was calculated using a relationship similar to that used to calculate the heat load to the propellant duct walls of the nuclear light bulb reference engine (Ref. 21). The relationship used was

$$Q_W = \frac{2L}{H} \dot{M}_p C_p St \left(T_B - T_W\right) \tag{B-1}$$

where Q_W is the heat lost to the duct walls, L is the axial length, H is the duct width, $\dot{M}_p$ is the total simulated propellant weight flow, C_p is the specific of the simulated propellant mixture, St is the Stanton number, T_B is the simulated propellant bulk temperature, and T_W is the duct wall temperature (assumed constant at 525 R). In Eq. (B-1) the variation of the fluid properties with temperature was accounted for in calculating the Stanton number. The Stanton number was obtained using the following correlation which is the same as that used in Ref. 20:

$$St = \frac{0.023}{(Pr)^{0.66} (Re)^{0.2}} \tag{B-2}$$

where Pr is the Prandtl number and Re is the Reynolds number. The total enthalpy rise of the simulated propellant stream is

$$H_p = \dot{M}_p C_p (T_I - T_E) \tag{B-3}$$

The heat absorbed is equal to the sum of Q_W and H_p:

$$Q_A = Q_W + H_p \tag{B-4}$$

The heat absorbed was assumed to be deposited uniformly along the duct length. The duct was divided into 100 equal-length intervals along its axial length and Eq. (B-4) was applied to each interval. The bulk exit temperature for each interval was calculated; this exit temperature was then taken as the inlet temperature of the next interval. In this way, the temperature rise of the simulated propellant was calculated as it flowed down the duct. The solid curve on Fig. 33 shows the result of this calculation for the highest power data point of the tests reported in Section IV.

When reradiation correction is included, Eq. (B-4) becomes

$$Q_A = Q_W + H_p + Q_{RR} \tag{B-5}$$

where Q_{RR} is the energy reradiated by the simulated propellant stream. The actual amount of the reradiation depends on the particle size, shape, and temperature. An upper bound on this reradiation can be obtained by treating the propellant as reradiating like a black body. Then Q_{RR} is

$$Q_{RR} = \sigma A T^4 \tag{B-6}$$

where σ is the Steffan-Boltzmann constant, A is the radiating surface area, and T is the black-body radiating temperature. The black-body radiating temperature was taken as the local simulated propellant bulk temperature. This is another assumption that serves to overestimate reradiation because, for the tests where reradiation might be important, the majority of the gas had optically thick streamers in it. For an optically thick gas, the effective reradiating temperature is lower than the bulk temperature. The radiating surface was assumed to be 0.078 in. from the outer duct wall. The results of the calculated temperature rise with reradiation correction is shown in Fig. 33 as the dashed line. The effect of reradiation is partially counteracted by the presence of reflecting metal parts outside the simulated propellant duct over its last 1.625 in. (see Fig. 3). The presence of these reflecting metal parts was not considered in the calculation of the reradiation. The actual simulated propellant bulk exit temperature lies between these two limits, between the temperatures

calculated as discussed above. More research is required to develop techniques by which simulated propellant bulk exit temperature can be measured. Some tests directed at further understanding of the difficulties encountered for measuring the simulated propellant exit temperatures are discussed in Appendix D.

APPENDIX C

SUPPORTING FLOW VISUALIZATION TESTS USING A TWO-DIMENSIONAL CHANNEL*

Supporting experiments were conducted using a two-dimensional channel to investigate the effectiveness of porous foam as a flow straightener. The test configuration consisted of a two-dimensional duct in which the entrance region is divided into three sections. A diagram of the duct is shown in Fig. 34(a). The duct had a 1-in. by 3-in. cross section and was 18 in. long. The entrance region had three plenum chambers as shown in Fig. 34(a). Porous foam was placed above the entrance region. A mixture of cigar smoke (particles ranging in size from 0.01 to 0.10 micron) and argon was injected into the central chamber and pure argon was injected into the outer (buffer) chambers.

Figure 34(b) presents photographs in which cigar smoke was injected into the central chamber at velocities of 2 and 9 ft/sec. In both photographs a clear region exists between the smoke and wall. (The change in smoke intensity along the length is due to non-uniform lighting.)

Because smoke photographs can be misleading, quantitative results were obtained using carbon dioxide in the central chamber. A series of gas samples were taken across the duct at axial locations 1.0 and 15 in. above the foam. The samples were analyzed with a mass spectrometer to determine the relative fractions of carbon dioxide and argon. Data from tests in which the stream velocities were 9 ft/sec are shown in Fig. 35. The results indicate that considerable diffusion of the carbon dioxide occurred either within the foam or immediately downstream of the foam, as evidenced by the initial width of the central stream tube.

Concentration distributions calculated from laminar diffusion theory are also shown in Fig. 35. The laminar diffusion coefficient used in the calculations was 0.022 in.^{2}/sec (Ref. 22). The curves indicate the diffusing effect equivalent to that calculated for about 15 in. of duct length occurred in the foam. The carbon dioxide then diffused at a rate about three times that expected based on the laminar diffusion calculations. This implies the effective diffusion coefficient was about three times larger than that used in the calculations. This is good agreement considering the uncertainty in the diffusion coefficient data. The results imply therefore that the flow downstream of the foam is not highly turbulent.

Additional flow visualization experiments were conducted with the two-dimensional duct shown in Fig. 36. As discussed above, good separation of the three equal-velocity streams (the two buffer-gas streams with a stream containing smoke in between) was observed when porous foam was placed above the entrance region.

---

* Tests conducted by A. E. Mensing.

Tests were subsequently conducted employing a stream containing carbon particles instead of smoke. Visual observations showed the appearance of many streamers in the particle-laden stream similar to those described in SECTION III. Streamers had not been observed in previous tests using smoke, apparently because visual observations with smoke do not provide sufficient details of the flow pattern.

Additional tests to investigate the streaming effect were then conducted with the two-dimensional duct using water colored with dye. In these tests, a layer of porous foam was placed across the entrance region just downstream of the duct dividers (see Fig. 36(a)). Only the central water stream was colored with dye. Photographs of this configuration are presented in Fig. 36(b). It is evident from the side view photograph in Fig. 36(b) that substantial streaming of the dye occurred. Foams of different porosity were placed over the inlet and, although the foams with the smaller pores resulted in smaller-sized streams, the streamers could not be totally eliminated. It was evident that the streamers were being caused by the foam.

Another inlet configuration was constructed to provide improved flow conditions at the entrance of the two-dimensional duct, thus eliminating the need for foam downstream of the inlet. A sketch of this configuration is shown in Fig. 37. The inlet area of each of the three streams was increased by a factor of ten and a gradual reduction in area was maintained up to the test section. A layer of porous foam was placed just downstream of the water inlets to break up the entering jets (see Fig. 37).

Photographs of the flow patterns obtained in these tests are presented in Fig. 38. Tests were conducted at several stream flow rates corresponding to different Reynolds numbers. (The characteristic length was taken to be the width of the duct, i.e., 1.0 in.) At a Reynolds number of 540 (photographs shown in Fig. 38(a)) the flow appeared laminar, good separation existed between the three streams, and no streaming was evident (compare Figs. 38(a) and 36(b) which were at approximately the same conditions). As the Reynolds number was increased, waves were noted in the flow (see Figs. 38(b) and (c)). Further increases in Reynolds number resulted in the wakes breaking into turbulence. The waves could be caused by the wakes shed from the splitter plates dividing the three channels, or by imperfect matching of the velocities of the three streams. The waves shown in Fig. 38(c) did not extend uniformly across the width of the channel. It appears that the end-wall boundary layers (i.e., the boundary layers on the 1.0-in.-wide sides) also have some effect on the flow in the duct.

Tests employing water and dye in the two-dimensional channel have confirmed that (1) the existence of the streamers is associated with the foam across the inlet and (2) a laminar flow of the three streams can exist for appreciable distances provided care is taken to eliminate turbulence in the entrance region.

APPENDIX D

RESULTS OF SPECIAL INSTRUMENTATION TESTS

Introduction

The primary objective of this study was to further evaluate the use of calorimetric, optical, and thermocouple techniques for measurement of the simulated propellant exit temperatures (local and bulk). A secondary objective was the development of a plasma torch to provide a controlled, continuously flowing, simulated propellant stream at bulk exit temperature between approximately 2000 and 12,000 R for use in instrumentation tests.

In the seeded simulated propellant heating tests described in SECTION IV of this report, energy was added to the propellant stream principally through radiation absorption. In the case of the plasma torch experiments described here, convective heating was the dominant mode of heat addition to the seeded simulated propellant. The seed material employed was the same type carbon particles used in the propellant heating tests discussed in SECTION IV. Bulk temperatures between approximately 5000 and 16,000 R was obtained at the torch exit plane. By diluting the hot gas (argon) downstream of the torch exit plane with additional argon, bulk temperatures between 2000 and approximately 3100 R were obtained. The design and operation of the plasma torch permitted extremely long test times compared with the shorter test times (less than 1 min) used in the d-c arc tests.

Plasma Torch System

Figure 39 is a schematic of the plasma torch system. The system consists of the plasma torch, d-c power supply, high-frequency starter, control console, seed dispersal system, and gas and water cooling systems. The torch is a modified 50-kw commercial plasma torch (Thermal Dynamics Model H-50). The d-c power supply (discussed in SECTION II) provided the electrical power to the torch electrodes through internally water-cooled power cables. A high-frequency starter was constructed to provide a safe and reliable starting capability. The control console used in the d-c arc radiant energy source tests reported in Section II was used in these tests. The console contained all necessary control operating components, electrical meters, power-supply controls, starter controls, and associated flow metering systems. A continuous record of the voltage drop from torch anode to cathode was recorded on a strip-chart recorder. Cooling water from the laboratory supply was used. The high-pressure seed dispersal system (see Figs. 39 and 14) was connected to injectors located in the test chamber assembly to provide the flow of argon gas and carbon seeds required for the tests.

Figure 40 is a sketch of the plasma torch tip assembly and associated calorimeters, water-cooled copper cylindrical test chamber and diagnostic tools employed (radiometer system, optical pyrometer system, and radial scanning thermocouple device). The central, water-cooled, hemispherically tipped, 0.312-in.-dia tungsten cathode (containing about 2 percent thorium to improve its electron-emitting properties) was located at the entrance of the water-cooled copper anode. The distance between the cathode and the anode could be varied by means of an adjusting screw. The cathode was positioned by first bringing it into contact with the anode and then retracting it about 0.01 in. away. Argon gas was fed axially through the annulus between the two electrodes, and thus through the arc whose current path was between the cathode tip and a circular region down the anode nozzle. Care was taken in the concentric alignment of the cathode relative to the anode as this minimized electrode erosion at high-power operation. It also helped to provide more stable arc operation. Alignment corrections were made by means of the adjusting screws. The alignment was checked using the high-frequency starter spark which was struck from the cathode to the anode while a small amount of argon purge flowed through the torch. When the arcs were uniformly distributed around the annulus, the alignment was judged to be correct. In all tests, argon at atmospheric pressure was used in the plasma torch cathode chamber, as the diluent to control bulk temperature, and as the seed carrier gas.

Ignition of the torch was accomplished with a remote starter button which energized the high-frequency (15 kHz) and high-voltage (18 kw peak-to-peak) arc starter with the main power supplies set for a current of about 150 amp. Once ignition occurred, the argon gas flow was adequate to blow the discharge into the nozzle portion of the copper anode and distribute it over a wider surface area. After completion of this starting sequence, the arc current (controlled by the rheostat control) and the argon gas weight flow rate (controlled by valves and monitored by rotameters) were adjusted to values desired for the test conditions.

Test Chamber and Exhaust Gas Calorimeter

The test chamber and the exhaust gas calorimeter located downstream of the test chamber are also shown in Fig. 40. The test chamber consists of a 1.5-in.-ID water-cooled copper tube (blackened on the inside surface) approximately 4 in. long. The operating pressure inside the test chamber was approximately 1.0 atm. Four copper diluent and seeded-gas injectors (0.065-in.-ID) were mounted in two diametrically opposed pairs with their tips extending 0.25 in. into the test chamber. They were located 0.6 in. above the exit plane of the torch. These copper injectors were soldered into the copper test chamber wall. The test section station, i.e., the location at which thermocouple radial traverses were made in addition to radiometer and optical pyrometer measurements, was located 3 in. downstream of the torch exit plane (see Fig. 40). The water-cooling coils of the test chamber ended about 1.0 in. upstream of the test section station. No special thermal insulation was applied to the outer periphery of the test chamber or exhaust gas heat exchanger.

To permit viewing at the test section station, a viewing tube and aperture assembly was attached to the test chamber (Fig. 40). A 0.325-in.-ID collimating tube, 11.25-in. long, was soldered into a port of the test chamber at the test section station. The inside of the tube was blackened to reduce stray reflections. A 0.125-in. aperture was attached to the extreme end (away from the test chamber) of the tube. A lithium fluoride window was attached to the tube directly behind the aperture. A specially constructed radiometer, similar to that discussed in Section II but employing a LiF_2 window, was located adjacent to the aperture. The total distance between the thermopile element and the centerline of the cylindrical test chamber was 13.0 in. The output of the radiometer system was displayed on a strip-chart recorder.

A 0.127-in.-dia port was located approximately 30 deg away from the axis of the optical viewing tube. This permits thermocouples with 0.125-in. stem diameters to be inserted into the test chamber at the test section station. A radial traversing mechanism was fabricated which permitted the thermocouples to be indexed into the test chamber. The output from the thermocouple was displayed on a strip-chart recorder.

Attached to the top of the test chamber was a water-cooled copper-brass cylindrical calorimeter (Fig. 40). The calorimeter was about 1 ft long and was positioned with its axis approximately 45 deg to that of the test chamber. The seed-laden argon exhaust leaving the calorimeter was routed into the exhaust hood vent system described in SECTION II. A chromel/alumel thermocouple was located in the exhaust gas line immediately downstream of the heat exchanger. It was installed to permit about a 5-in. immersion length into the exhaust gas exit line, thus minimizing possible errors due to heat conduction through the stem.

Measurement Techniques and Calibration Results

To investigate the bulk temperature ranges obtainable using the plasma jet torch, a separate series of tests was conducted using basically the configuration shown in Fig. 40, but prior to installation of the seed injectors and with the ports at the test section station plugged. The results are shown in Fig. 41. This illustrates the range of bulk temperatures achievable with the plasma torch in relation to the total power input and argon gas weight flow rate to the torch assembly only (no diluent or seeded gas addition downstream of the torch exit plane). The open symbols correspond to the ordinate on the left (total electrical power input to the torch divided by the argon gas weight flow rate from the torch). For reference, the 500-amp torch operating condition corresponds to about 10,500 R bulk temperature near the plasma torch exit plane. The bulk temperatures were calculated for argon based on a constant specific heat. The solid symbols in Fig. 41 correspond to the ordinate shown at the right. In this case, the total power in the plasma exhaust at the test section station, as determined from the exhaust gas calorimeter measurements, was used. The displacment of the solid symbol data below

that of the open symbols provides an indication of the overall efficiency of the plasma torch in converting electrical input power into argon gas energy content.

To permit an estimate of the amount of radiation from the plasma jet which escapes vertically at the test chamber, a test was conducted using a radiometer-mirror optical system and a standard tungsten filament lamp. The configuration was similar to that shown in Fig. 39. The inside of the test chamber was blackened and a mirror was located above the exit plane of the test chamber and set at an angle of 45 deg to the exit plane. A radiometer was located to permit viewing down the test chamber through the mirror. The plasma torch was then operated at the 500-amp test condition and the other operating parameters shown in the notes in Fig. 42. The data indicated that less than 5 percent of the total power deposited into the plasma was lost due to radiation escaping vertically through the test chamber. This is reasonable based on the bulk temperatures of the plasma torch. In contrast to the d-c arc radiant energy source tests where the thermocouples were exposed to relatively high radiation levels, the tests conducted with thermocouples using the plasma torch should not have the high associated radiation errors involved.

Test Results

Local Temperature Measurements

The test results for the plasma jet torch operating at the 500-amp condition are summarized in Fig. 42. Refer to Fig. 40 for details of the test configuration. The operating test conditions are shown in the notes in Fig. 42. Figure 42 shows the radial variation of the local temperature, T_L, as measured by a platinum/platinum 10-percent rhodium exposed junction thermocouple, for the three cases of no seeds, light seed flow, and heavy seed flow. Thermocouple measurements were made from the test chamber centerline to the dimensionless radial position corresponding to 0.75. At values beyond this location, leakage occurred around the convergent tip of the thermocouple stem and the access port. This affected the thermocouple reading and local flow pattern. These data show the effects of light and heavy seed flows on the local temperature levels and their radial profile trends. It is important to point out that the test chamber and seed distribution within the test chamber using the plasma torch configuration is not the same as that used with the d-c arc radiant energy source. In the d-c arc radiant energy source tests, the seeds were injected vertically through a central annulus and then passed through layers of foam prior to reaching the test section. Buffer layers also were successfully employed to maintain the seeds off the test chamber walls. In the case of the plasma torch configuration, the seeds were injected radially into the main stream with no use of buffer layers. In addition, no foam material was used anywhere in the test chamber.

The temperatures measured indicate a relatively flat profile in the central region of the test chamber. Two values are indicated for the no-seed case at the

centerline location. The higher temperature of 3340 R corresponds to a measurement made with a clean thermocouple junction (no carbon seed coating). Since it was believed that the coating of carbon which builds up on the junction may affect the temperature measurement, this additional data point was taken for reference. All remaining data points shown on Fig. 42 were taken with the thermocouple coated with carbon seed material as acquired during actual test operation.

To verify the accuracy of the platinum/platinum 10-percent rhodium thermocouple, a separate series of calibration tests were completed. The actual thermocouple used was calibrated in a furnace of known temperature and against a chromel/alumel thermocouple of similar design when both were exposed to the same temperature. The results indicate about a 5-percent difference in the temperature readings between a clean platinum/platinum 10-percent rhodium thermocouple and one that has been exposed to a series of hot seed tests, the former being higher. Apparently the layer of carbon accumulated on the surface of the thermocouple junction acts as an insulator. In addition, some chemical reactions may have taken place between the hot carbon stream and the bead junction. All data shown in Fig. 42 were obtained after sufficient time had elapsed for all systems to come to steady-state conditions.

The addition of a light flow of carbon seeds resulted in a decrease in local temperatures, as shown by the middle curve in Fig. 42. The local temperature at the centerline of the test chamber decreased approximately 10 percent. When a heavy flow of carbon seeds was used, this drop changed to about 30 percent. A significant increase in the heat capacity due to the addition of carbon particles resulted in the decreases in the local temperatures measured as seeds were added. Unfortunately, an accurate determination of the carbon seed weight flow rate could not be made in these tests; thus, an estimate based on prior cold and hot flow seed test results was used. These temperature drops are roughly equal to the temperature drops calculated using estimated values of C_p for the argon/carbon mixture.

Calorimetric Measurements

Based on the calorimeter measurements with no seeds flowing, the bulk temperature was calculated to be 3067 R. This calculation was based on a constant specific heat of argon of 0.125 Btu/lb-deg R. This bulk temperature appears high relative to the local temperature profile.

Consideration was given to all apparent reasons that could account for the difference between the T_L profiles and T_B as measured by the calorimeter. A completely satisfactory single explanation was not found. However, several factors may have contributed to this difference. The argon flow rates used were quite low for the flow metering equipment employed in these tests. Therefore, an error in determining the argon weight flow rate would result in a significant change in the calculated bulk temperature. The rotameters as used are subject to about 10 percent error at the low-scale range. Local temperature measurements could not be made close to the wall; a significant portion of the main flow was directed out the

thermocouple port when the thermocouple junction was moved near the wall boundary. Secondary flow patterns exist near the wall; associates with these may be temperatures higher than those at mid-radius, particularly in the case with seed flow. It is possible that these secondary flows of recirculating hot carbon particles together with the increased volume effect at the larger radius, may result in increased bulk temperatures based on the integrated local values. The short immersion length of the platinum/platinum 10-percent rhodium thermocouple (and associated conduction errors) may also have affected the local temperature recorded off-axis. Ideally, a long-stem thermocouple (immersion length greater than 20) located colinear with the test chamber axis should be used. The calculated bulk temperature based on calorimetric measurements with seeds flowing is also uncertain due to the heavy accumulation of seeds in the calorimeter (difficult to avoid under heavy seed flow conditions) and the uncertain carbon seed weight flow rate.

Until the extent of these possible errors can be assessed, the type of agreement shown in Fig. 42 will have to be accepted with this type of instrumentation.

Optical Measurements (Radiometer and Pyrometer)

In addition to the calorimeter and local temperature measurements, the reradiation from the hot seeded stream was also measured using both a radiometer and an optical pyrometer. These results, along with the bulk temperature calculated from the calorimetric measurements, are also shown in Fig. 42.

Using the radiometer and view port system discussed previously, measurements were made of the levels of reradiation obtained from a heavy flow of seeds. Calculations based on the radiant energy flux measurements indicate an equivalent black-body radiating temperature of 2650 R. The lower T_L profile that resulted with a heavy flow of seeds is what would be expected on the basis of increasing C_p for the argon/carbon mixture.

The temperature measured using the optical pyrometer in place of the radiometer are also shown in Fig. 42 for the no-seed and light-seed cases. The pyrometer measurements also indicated what was expected -- for two streams at about the same temperature, reradiation from the seeded stream was higher than that from the unseeded stream. For an estimated carbon seed weight flow rate of approximately 2×10^{-3} lb/sec, the calculated bulk temperature for this test is approximately 2530 R. This value is in reasonable agreement with the 2650 R equivalent black-body radiating temperature obtained from the radiometer measurements. Thus, the results indicate that the radiant heat flux emitted from the seeded gas approaches that of the black-body radiant heat flux corresponding to the bulk gas temperature.

It is important to emphasize that the results obtained here were under better controlled conditions than those in the d-c arc propellant duct. Until a more exact determination of the carbon seed weight flow rate and distribution is made, no further conclusions can be made relative to the seeded stream opacity and its

effect on the radiant heat flux emitted from the seeded gas. In the future, work should concentrate on better determination of seed flow rate using an on-line technique.

Summary

As a result of these experiments, an assessment of the operating characteristics of the plasma torch system has been obtained. The system has been operated at bulk temperatures (based on calorimetric measurements) well into the range of seeded simulated propellant temperatures of current interest in the hot-flow tests using the d-c arc radiant energy source. Radial temperature profiles were measured for two conditions of seed weight flow rates and for the no-seed case. Reradiation measurements from the hot carbon seeded stream were obtained, as were optical pyrometer measurements of both the seeded and unseeded simulated propellant stream.

On the basis of these limited tests, it is concluded that calorimetric methods can be used to obtain bulk exit temperatures, provided run times are sufficient to reach equilibrium conditions and provided accumulation of seeds in the calorimeter can be prevented. The optical measurement techniques (radiometer and optical pyrometer) compared favorably in these tests with a calculated bulk temperature based on an estimated seed flow rate. Final judgment of the accuracy of these methods requires further testing with a more satisfactory method than is presently used for estimating seed flow rate. The measured reradiation from the seeded gas in these tests was in fairly good agreement with the reradiation expected based on the calculated bulk temperature. Finally, it is apparent that thermocouples can be successfully used to measure local temperatures in seeded streams up to perhaps 3000 R. At higher temperatures, considerable research on advanced shielded thermocouples would be required to assess their usefulness.

The plasma torch configuration as constructed is suited for continued high-temperature heat transfer and radiation studies directly associated with seeded simulated propellant streams and future fuel-handling experiments. Bulk exit temperatures in the range from 2000 to 16,000 R are available. Additional diagnostic tools and techniques (e.g., double-sonic orifice probes, enthalpy probes, multiple-shielded aspirating thermocouples, ablating probes, etc.) can be evaluated and calibrated using this facility as required in the future.

TABLE I

FLOW CONDITIONS FOR D-C ARC
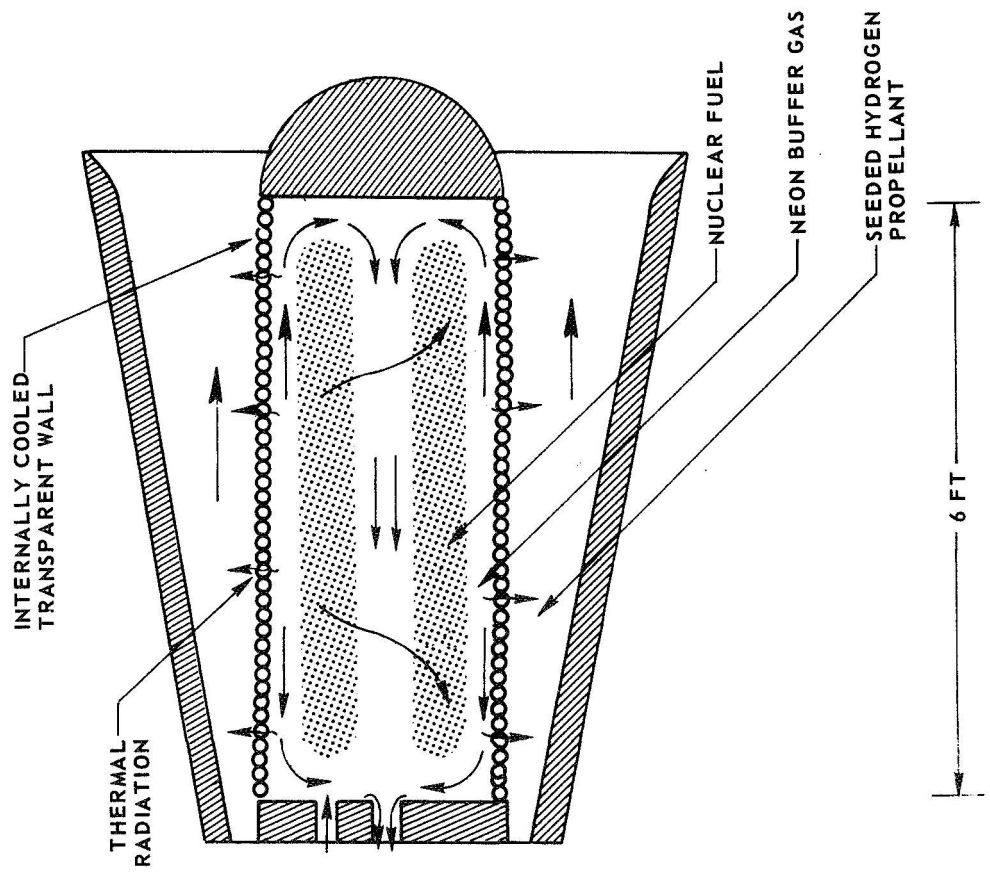PROPELLANT HEATING TESTS

Pressure In Propellant Duct	1.0 atm
Argon Weight Flow Rates	
Inner Buffer Flow	0.010 lb/sec
Outer Buffer Flow	0.016 lb/sec
Seed Carrier Flow	0.004 lb/sec
Propellant Stream Velocity	5.0 ft/sec for all three streams
Inlet Temperature	525 R
Estimated Seed Flow Rate	0.003 lb/sec
Total Simulated Propellant Flow (0.010 + 0.016 + 0.004 + 0.003)	0.033 lb/sec

TABLE II

SUMMARY OF SIMULATED PROPELLANT HEATING TEST RESULTS

Run	Incident Radiation, Q_I - kw	Absorbed Radiation, Q_A - kw	Fraction Transmitted, η_T	Bulk Exit Temperature Based On Attenuation Without Reradiation, T_E - Deg R	Bulk Exit Temperature Based On Attenuation With Reradiation, T_E - Deg R	Bulk Exit Temperature Based On Calorimetry, T_{CAL} - Deg R	Local Exit Temperature Based On Thermocouples, T_{TC} - Deg R
1	4.30	3.27	0.239	1223	1195	753	1005
2	4.33	3.82	0.118	1332	1294	996	1010
3	4.95	2.55	0.485	1077	1058	1727	2560
4	5.14	4.80	0.066	1523	1465		990
5	5.65	5.40	0.045	1637	1564		970
6	5.65	2.23	0.606	1101	995		
7	5.81	3.43	0.41	1254	1223		1620
8	5.81	2.90	0.50	1150	1126	620	1860
9	5.81	0.17	0.97	569	566	564	1670
10	5.86	3.63	0.38	1275	1261	1006	1910
11	5.90	2.48	0.58	1063	1044	774	1960
12	5.90	1.89	0.68	941	928	1088	1700
13	5.90	3.84	0.35	1335	1297	1169	1930
14	5.95	5.06	0.15	1572	1508		1270
15	5.99	4.28	0.285	1423	1376	774	2670
16	6.16	2.16	0.65	997	981	922	1710
17	6.35	2.16	0.66	997	982		
18	6.50	5.88	0.096	1729	1641	1387	
19	6.56	6.27	0.044	1804	1703	782	1614
20	6.75	2.47	0.634	1061	1043		
21	6.84	6.16	0.100	1782	1666		
22	6.84	4.61	0.326	1486	1433		
23	7.19	6.90	0.04	1923	1799		1760
24	7.24	5.73	0.208	1702	1619		
25	7.69	2.98	0.612	1165	1141		
26	7.88	7.02	0.109	1945	1817		
27	8.13	7.10	0.126	1861	1829		
28	8.21	6.82	0.169	1908	1787		
29	8.23	5.32	0.354	1622	1551		1810
30	8.53	7.34	0.139	2006	1864		
31	9.66	8.64	0.106	2248	2044		
32	9.99	6.57	0.342	1861	1750		
33	10.69	9.83	0.08	2471	2197		
34	10.69	5.12	0.521	1585	1519		
35	13.50	12.86	0.097	2904	2461		
36	19.25	18.48	0.04	4050	2970		
37	20.00	18.72	0.064	4093	2985		
38	20.00	17.00	0.15	3781	2871		

FIG. 1

NUCLEAR LIGHT BULB CONCEPT AND D-C ARC PROPELLANT HEATING CONFIGURATION

(a) SCHEMATIC OF UNIT CAVITY OF NUCLEAR LIGHT BULB ENGINE

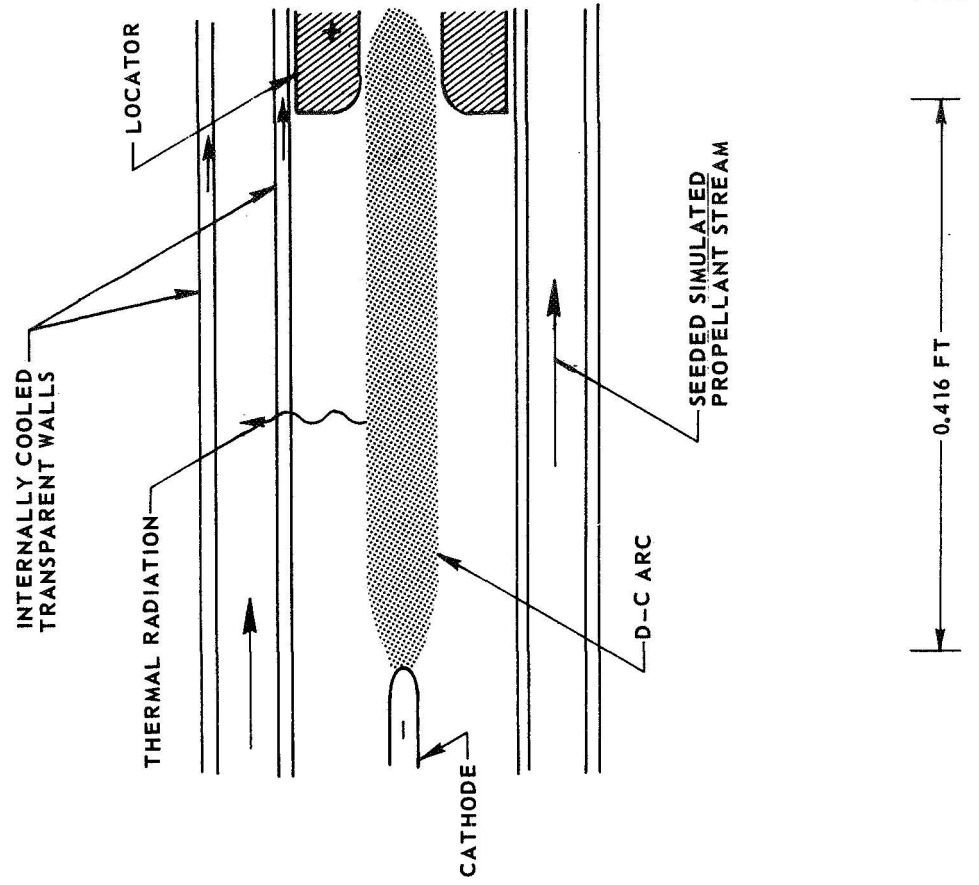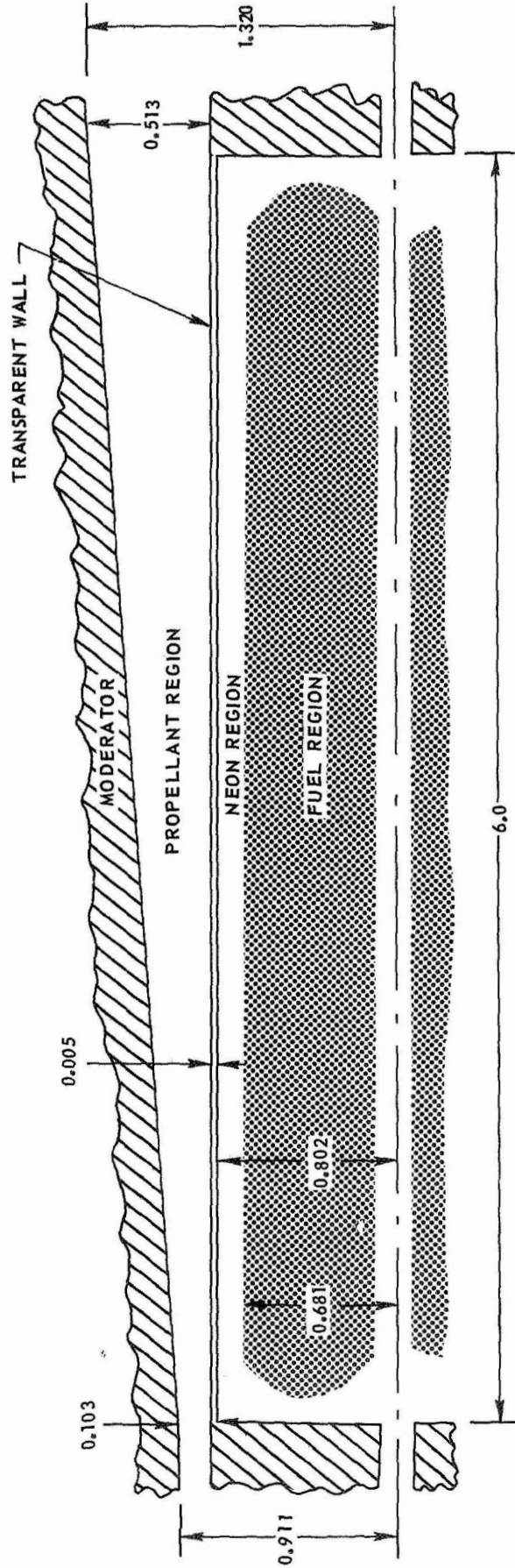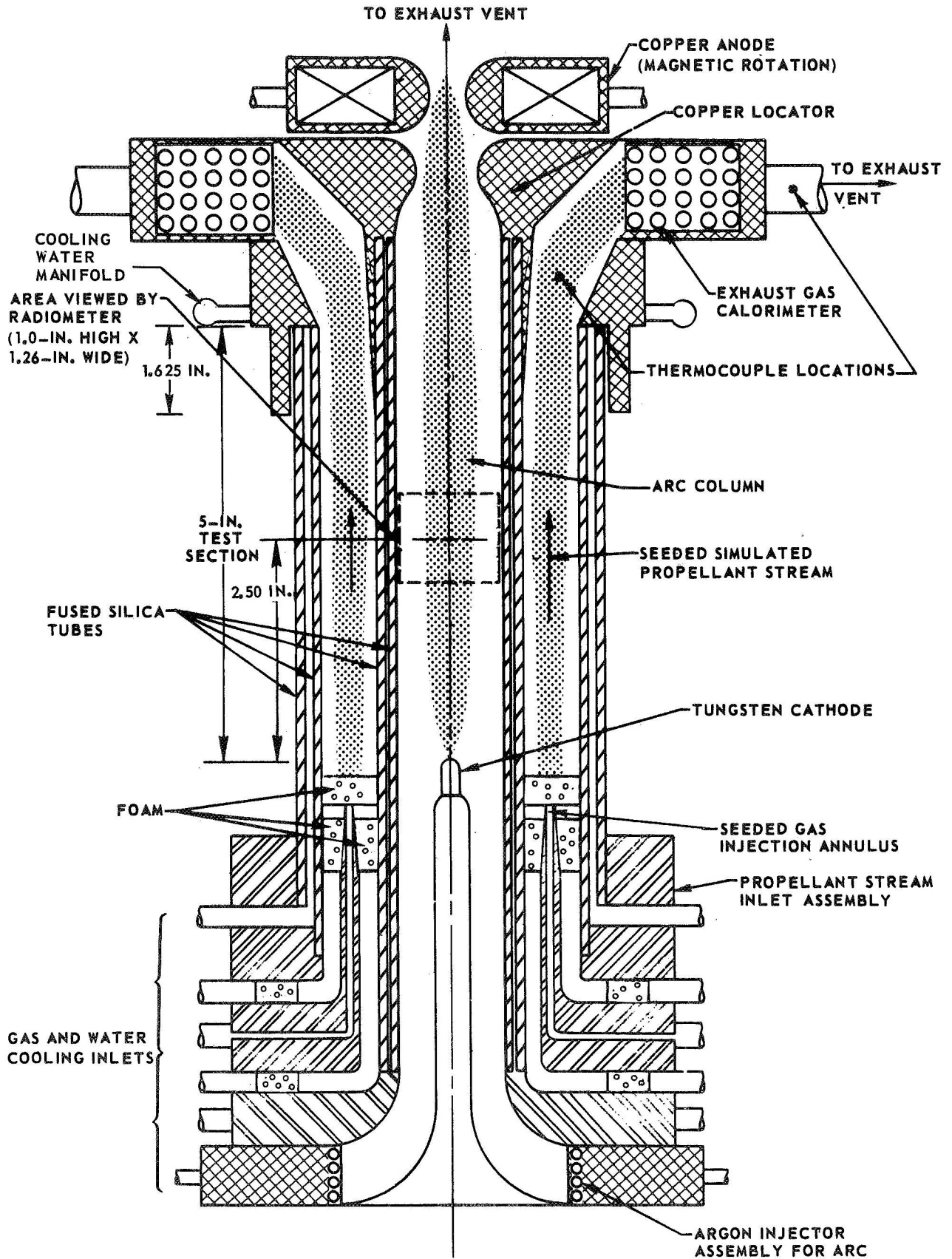(b) SCHEMATIC OF D-C ARC CONFIGURATION FOR PROPELLANT HEATING SIMULATION TESTS

FIG. 2

DIMENSIONS OF UNIT CAVITY IN REFERENCE ENGINE

ALL DIMENSIONS IN FT

COMPLETE ENGINE IS COMPOSED OF A SEVEN-UNIT-CAVITY CLUSTER

FIG. 3

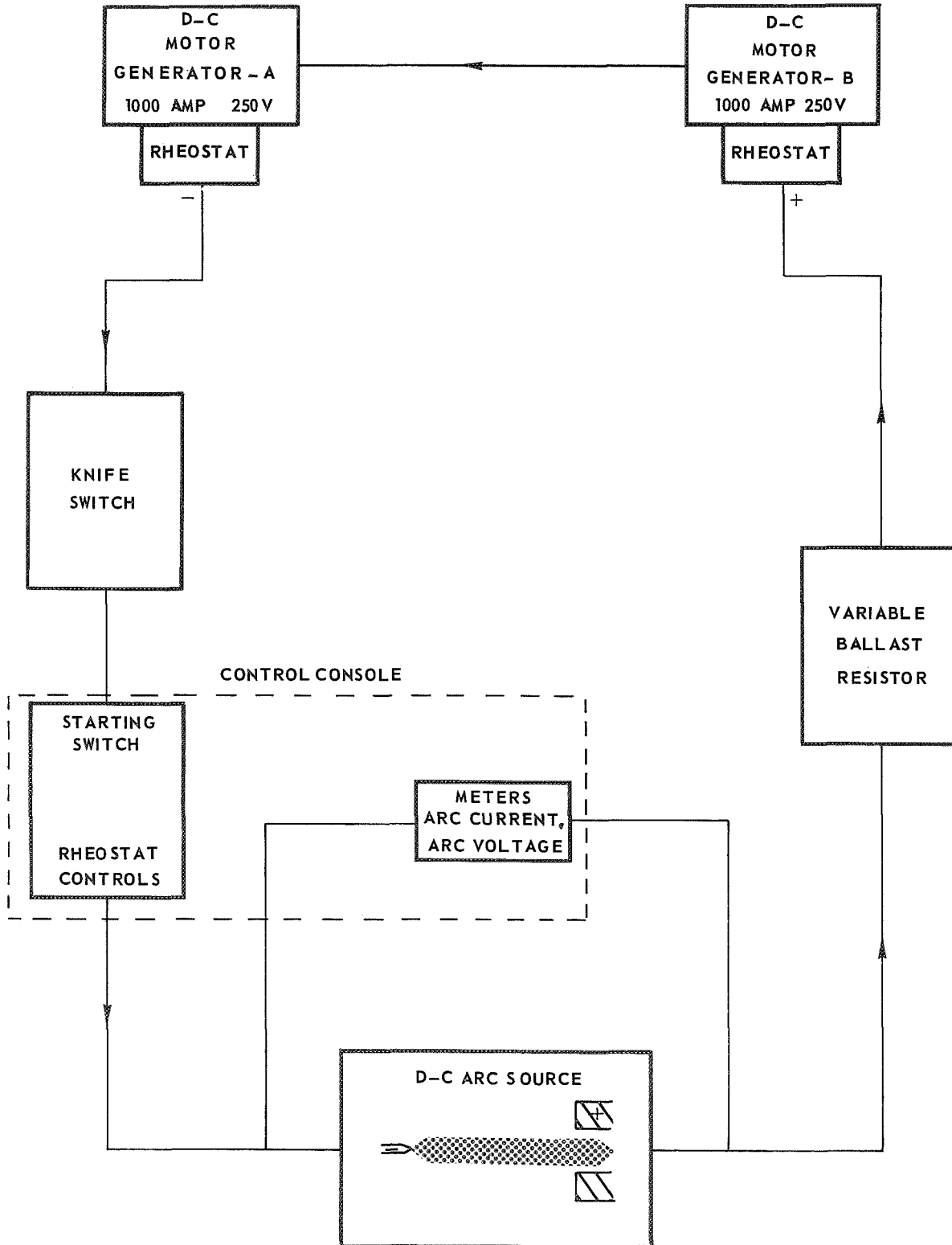# SKETCH OF BASIC D-C ARC HEATER CONFIGURATION WITH PROPELLANT HEATING ASSEMBLY

TO EXHAUST VENT

COPPER ANODE (MAGNETIC ROTATION)

COPPER LOCATOR

TO EXHAUST VENT

COOLING WATER MANIFOLD

AREA VIEWED BY RADIOMETER (1.0-IN. HIGH X 1.26-IN. WIDE)

1.625 IN.

EXHAUST GAS CALORIMETER

THERMOCOUPLE LOCATIONS

ARC COLUMN

5-IN. TEST SECTION

2.50 IN.

SEEDED SIMULATED PROPELLANT STREAM

FUSED SILICA TUBES

TUNGSTEN CATHODE

FOAM

SEEDED GAS INJECTION ANNULUS

PROPELLANT STREAM INLET ASSEMBLY

GAS AND WATER COOLING INLETS

ARGON INJECTOR ASSEMBLY FOR ARC

FIG. 4

BLOCK DIAGRAM OF ELECTRICAL COMPONENTS OF D-C ARC HEATER

ARROWS DENOTE DIRECTION OF CURRENT FLOW

FIG. 5

SCHEMATIC DIAGRAM OF D-C ARC HEATER ELECTRICAL CIRCUIT
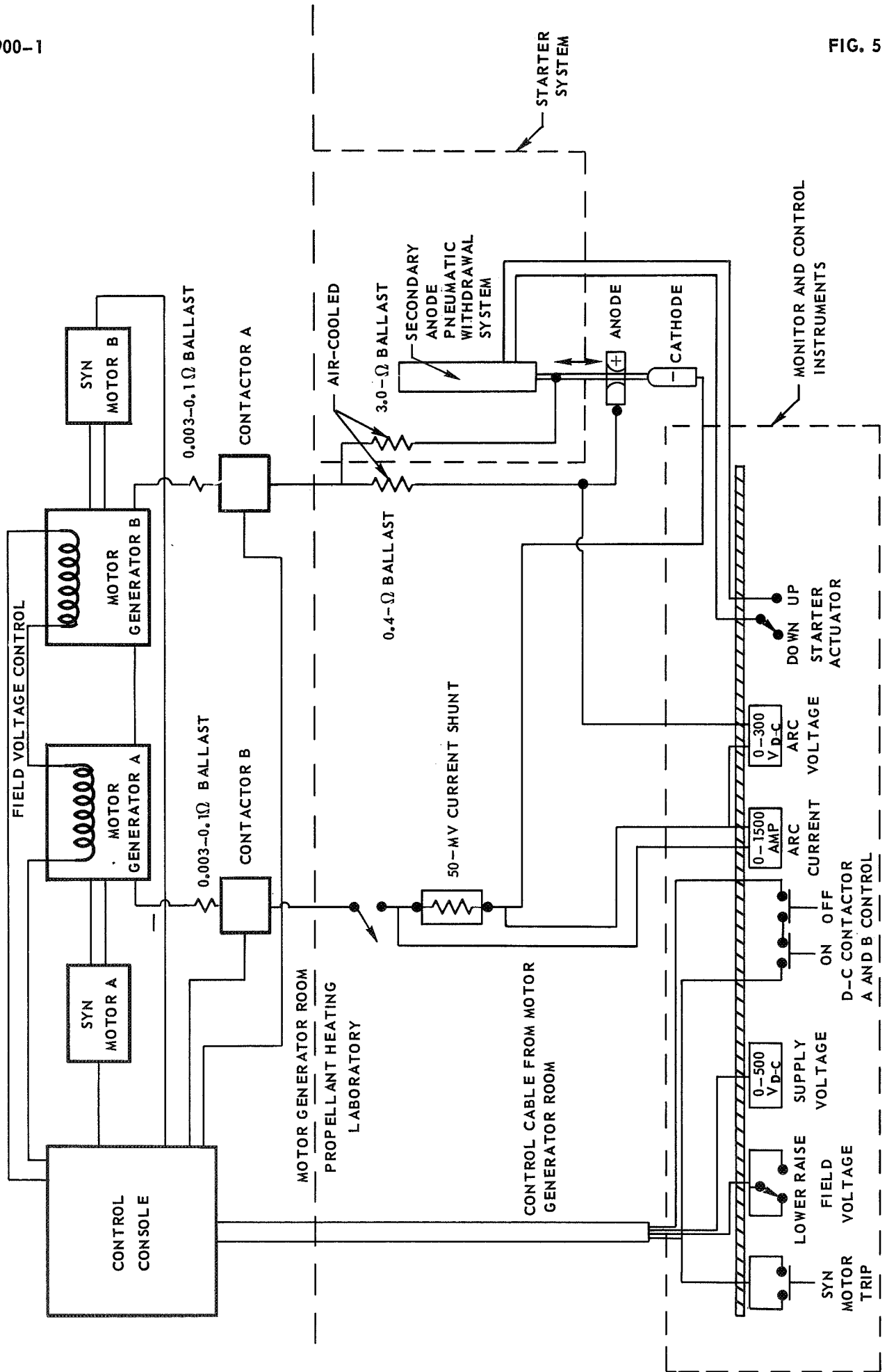
ELECTRICAL OPERATING CHARACTERISTICS OF D-C ARC HEATER USED FOR PROPELLANT HEATING TESTS

1.0 ATM PRESSURE ; ARGON ARC

SEE FIG. 3 FOR HEATER SCHEMATIC DIAGRAM

SEE FIG. 5 FOR SCHEMATIC DIAGRAM OF ELECTRICAL CIRCUIT

OPEN-CIRCUIT VOLTAGE FOR SERIES OPERATION 500 V D-C

FIG. 7
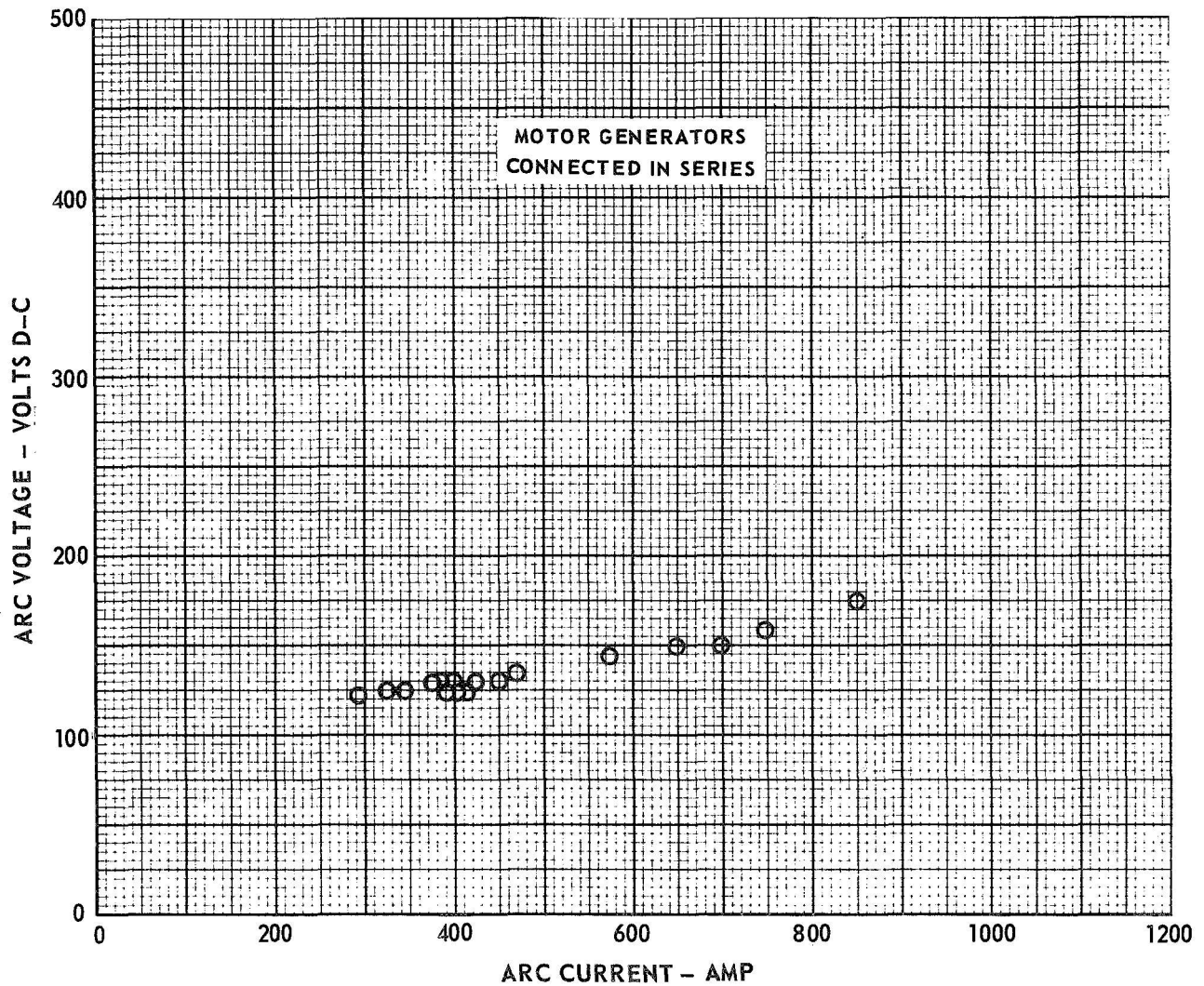
SCHEMATIC DIAGRAM OF D-C ARC HEATER GAS AND WATER FLOW SYSTEMS

ARROWS DENOTE DIRECTION OF FLOW

MAIN WATER SUPPLY

450-PSIG COOLING WATER PUMP

COOLING WATER RESERVIOR

180-PSIG COOLING WATER PUMP

ARC VORTEX ARGON SUPPLY

SIMULATED PROPELLANT ARGON SUPPLY

COOLING WATER INLET MANIFOLDS

SEED DISPERSAL SYSTEM

COOLING WATER EXHAUST

EXHAUST HOOD

ANODE

CATHODE

D-C ARC

SEEDED GAS

SHIELDED VIEWING WINDOW

ARC CONTROL PANEL
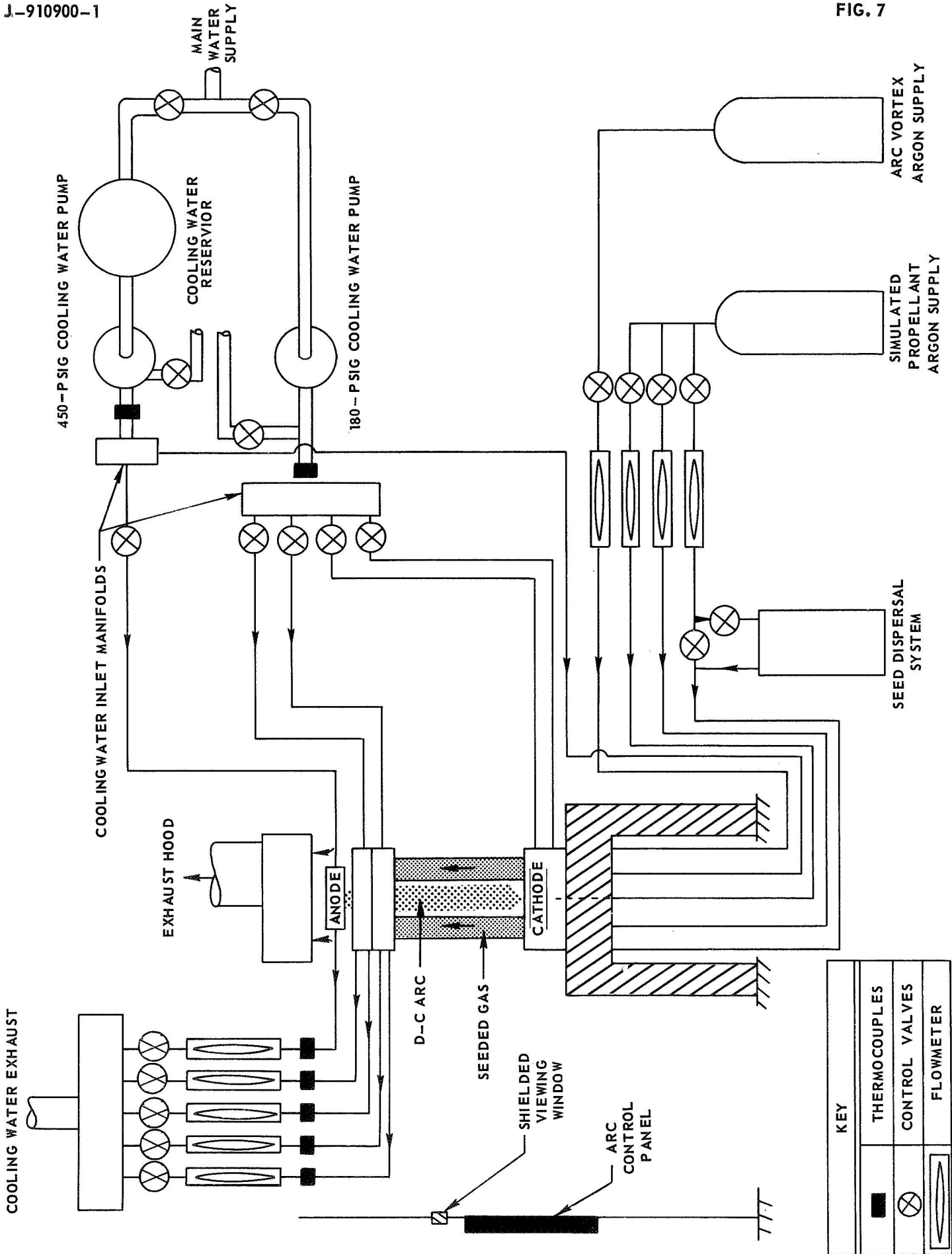
KEY

| THERMOCOUPLES |
| CONTROL VALVES |
| FLOWMETER |

64

PHOTOGRAPH OF CONFIGURATION FOR PROPELLANT HEATING TESTS USING THE D-C ARC HEATER

FIG. 9
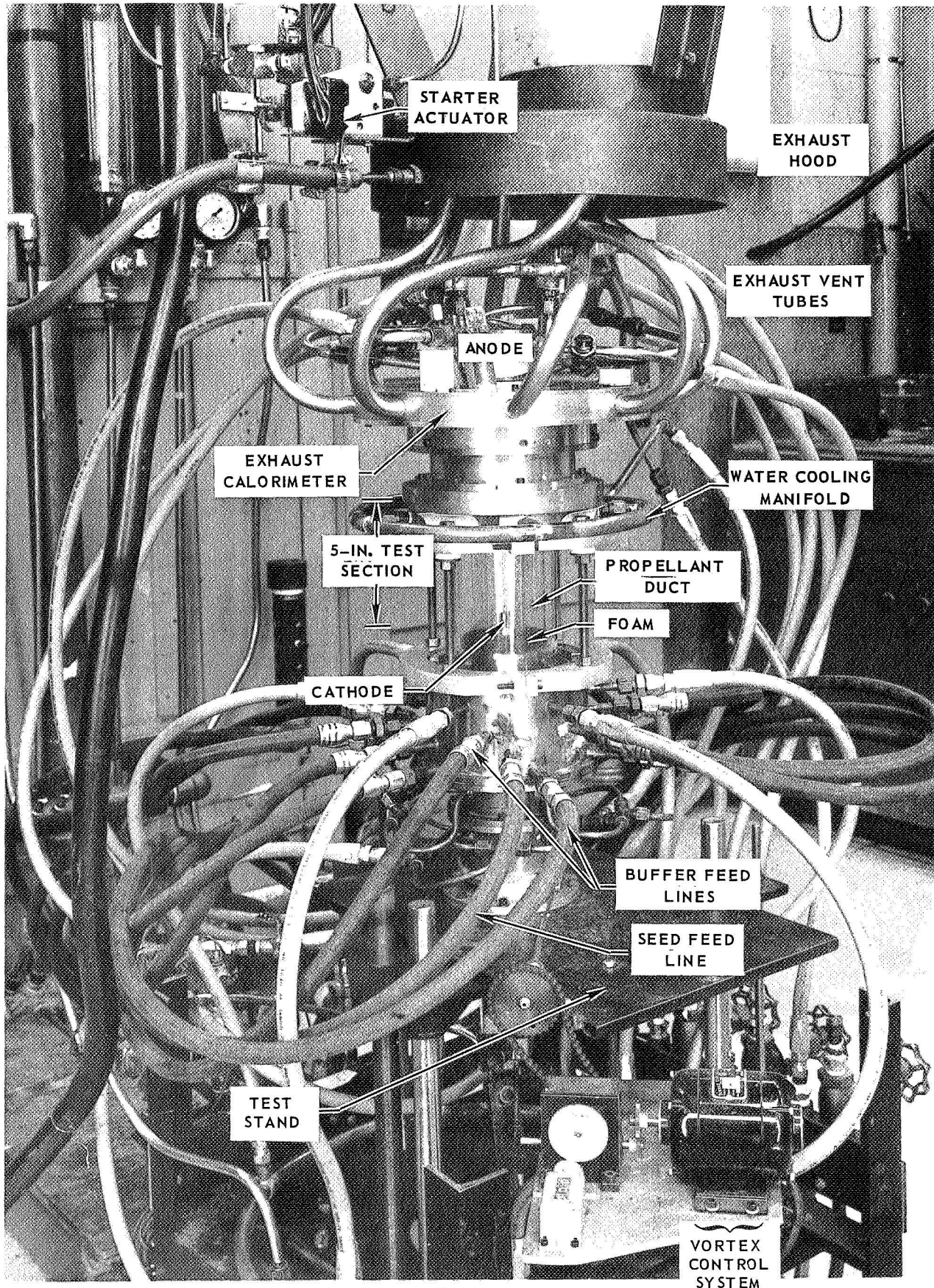
SKETCH OF RADIOMETER OPTICAL SYSTEM

SEE FIG. 3 FOR TEST SECTION DETAILS

ANODE

ARC

WATER COOLING MANIFOLD

5.0-IN. TEST SECTION

1.625 IN.

1.0 IN.

CATHODE

2.5 IN.

8.0 IN.

RADIOMETER APERTURE

0.75 IN.

39.4 IN.

0.25-IN. X 0.25-IN. SQUARE THERMOPILE DETECTOR

RADIOMETER

FIG. 10
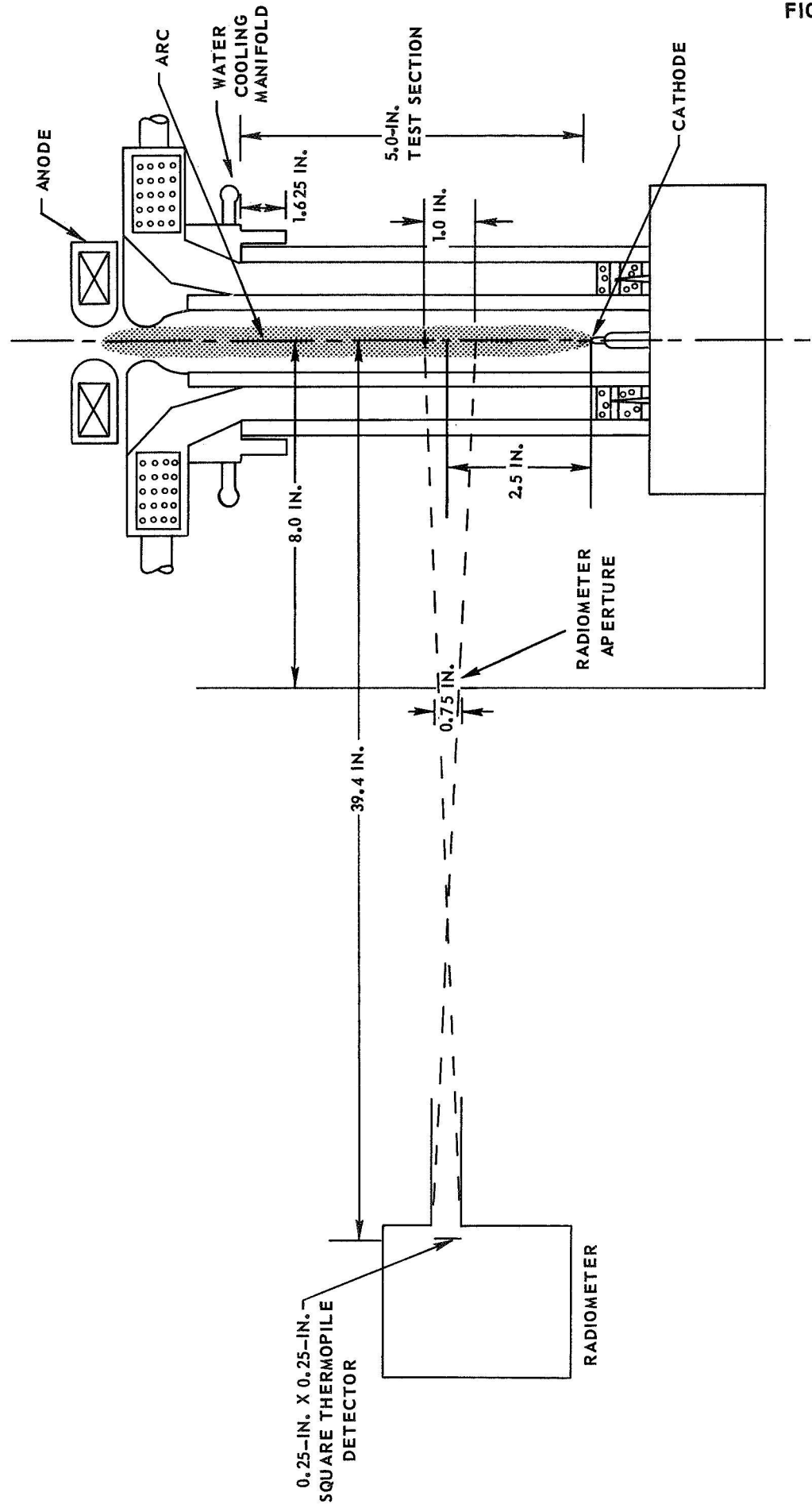
POWER RADIATED BY D–C ARC THROUGH PERIPHERAL WALL COOLANT PASSAGE IN VARIOUS WAVELENGTH RANGES

RADIATION PASSES THROUGH TWO FUSED SILICA TUBES
AND 0.099–IN.–THICK WATER LAYER

TOTAL ARC POWER, Q_T= 35 KW

PRESSURE, P = 1.0 ATM

ARGON WEIGHT FLOW, $\dot{M}_A$ = 0.018 LB/SEC

a) LENGTH VIEWED BY RADIOMETER (SEE FIG. 9)
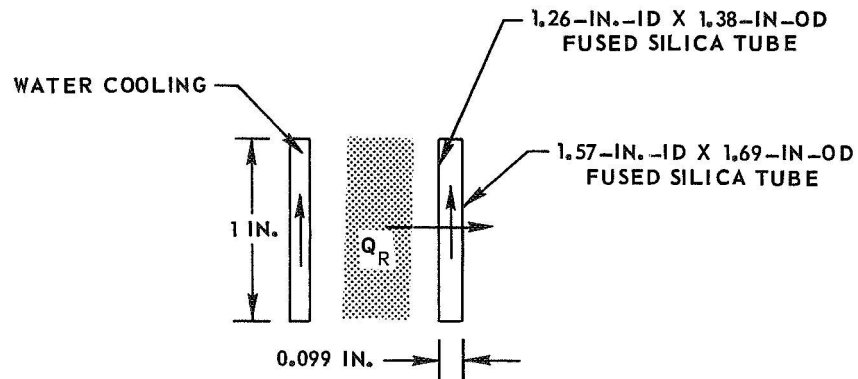
b) POWER RADIATED IN VARIOUS WAVELENGTH BANDS

FIG. 11
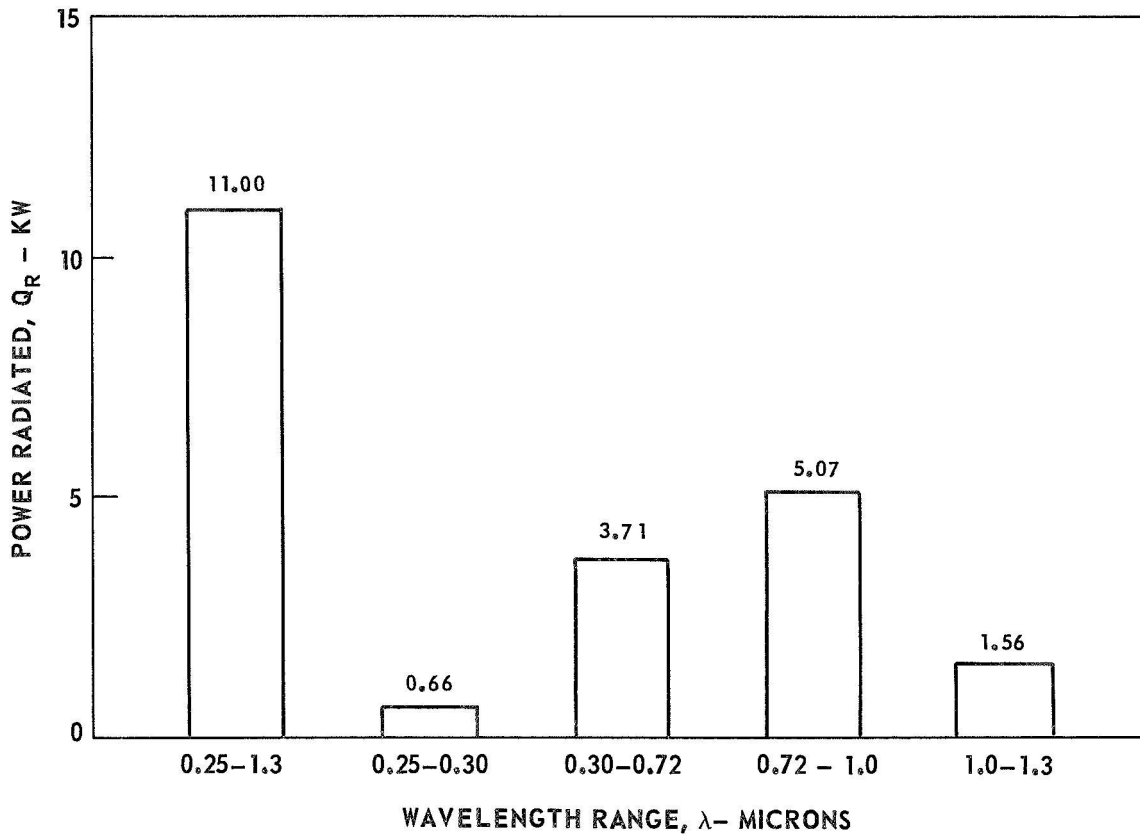
TRANSMISSION CHARACTERISTICS OF FILTERS USED FOR RADIATION MEASUREMENTS

FILTER THICKNESS – 0.079 IN.
SEE FIG. 9 FOR RADIOMETER OPTICAL SYSTEM

FILTER	MEASURED UPPER AND LOWER 50 PERCENT TRANSMISSION LEVELS, λ – MICRONS	
	LOWER CUT-OFF	UPPER CUT-OFF
BaF_2 THERMOPILE DETECTOR	0.25	– –
WG–305	0.30	2.6
RG–715	0.72	– –
RG–1000	1.00	– –
0.099-IN.-THICK LAYER OF WATER	0.18	1.27
WG–230	0.22	2.6

INTERNAL TRANSMITTANCE, $I_\lambda / I_{0,\lambda}$

WAVELENGTH, λ – MICRON

FIG. 12
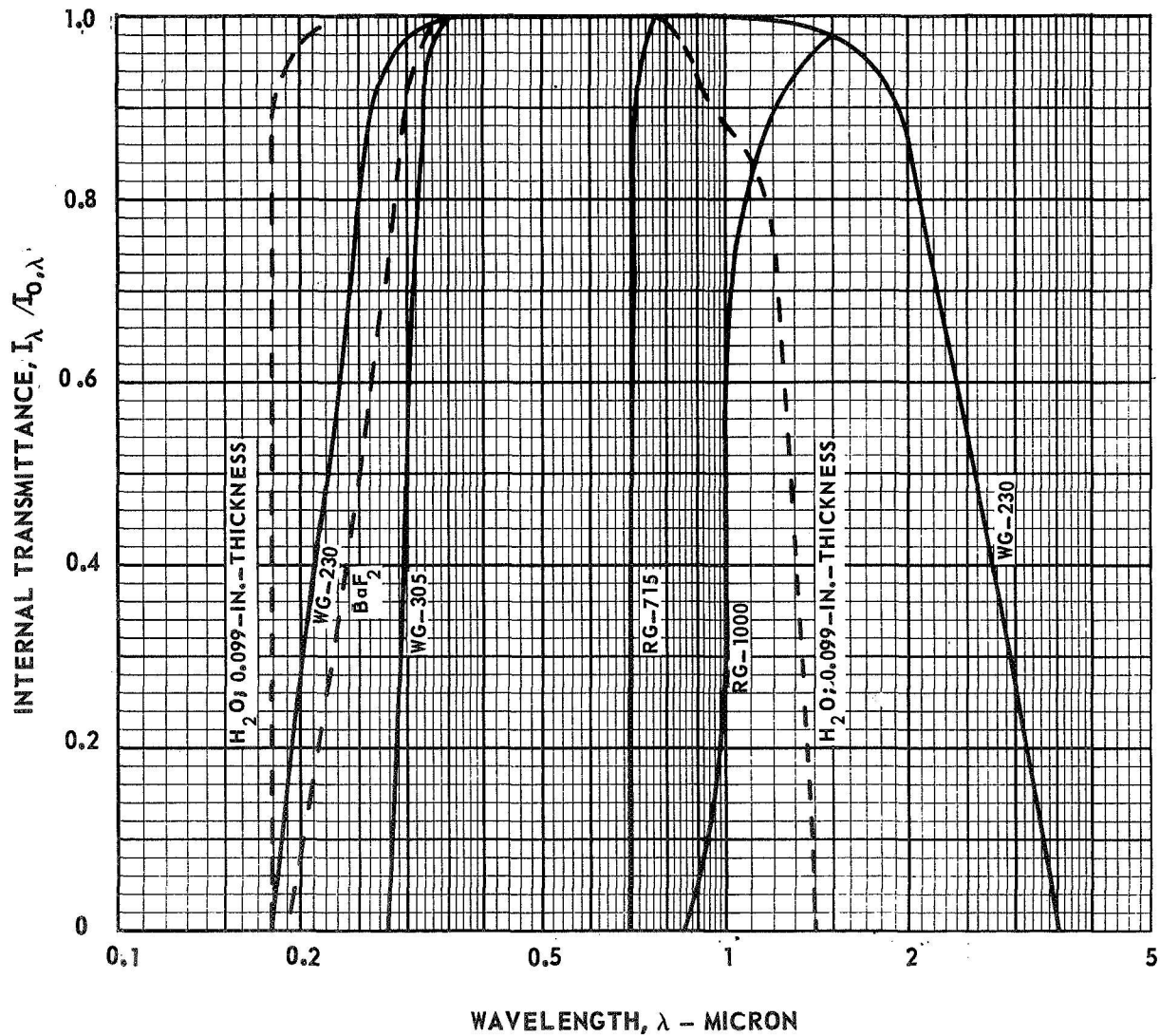
DETAILS OF EXHAUST SECTION AND CALORIMETER OF BASIC D-C ARC PROPELLANT HEATING TEST CONFIGURATION

SEE FIG. 3 FOR TEST SECTION DETAILS

ANODE

AXIAL THERMOCOUPLE LOCATION (SEE FIG. 13)

ANODE MAGNET COIL

CALORIMETER

LOCATION OF EXHAUST VENT THERMOCOUPLE

WATER-COOLED COPPER LOCATOR

TO SEED EXHAUST VENT

COPPER COOLING COILS

SHIELDED "O"-RING

PROPELLANT STREAM FLOW DIRECTION

WATER-COOLED COPPER EXHAUST SHIELD

CARBON INSERTS

RADIAL THERMOCOUPLE LOCATION (SEE FIG. 13)

EXIT PLANE OF 5-IN.-LONG TEST SECTION

LOCATION OF 4.12-IN.-OD FUSED SILICA TUBE

WATER COOLING ANNULUS

D-C ARC CENTERLINE

FUSED SILICA TUBES

1.77 IN.

FIG. 13

PHOTOGRAPH OF THERMOCOUPLES USED TO MEASURE LOCAL SIMULATED PROPELLANT EXIT TEMPERATURE

ALSO SEE FIG. 14

EXPOSED WELDED JUNCTION   ERODING JUNCTION   SHIELDED ASPERATING JUNCTION   RIGHT ANGLE JUNCTION   EXPOSED WELDED JUNCTION

FIG. 14
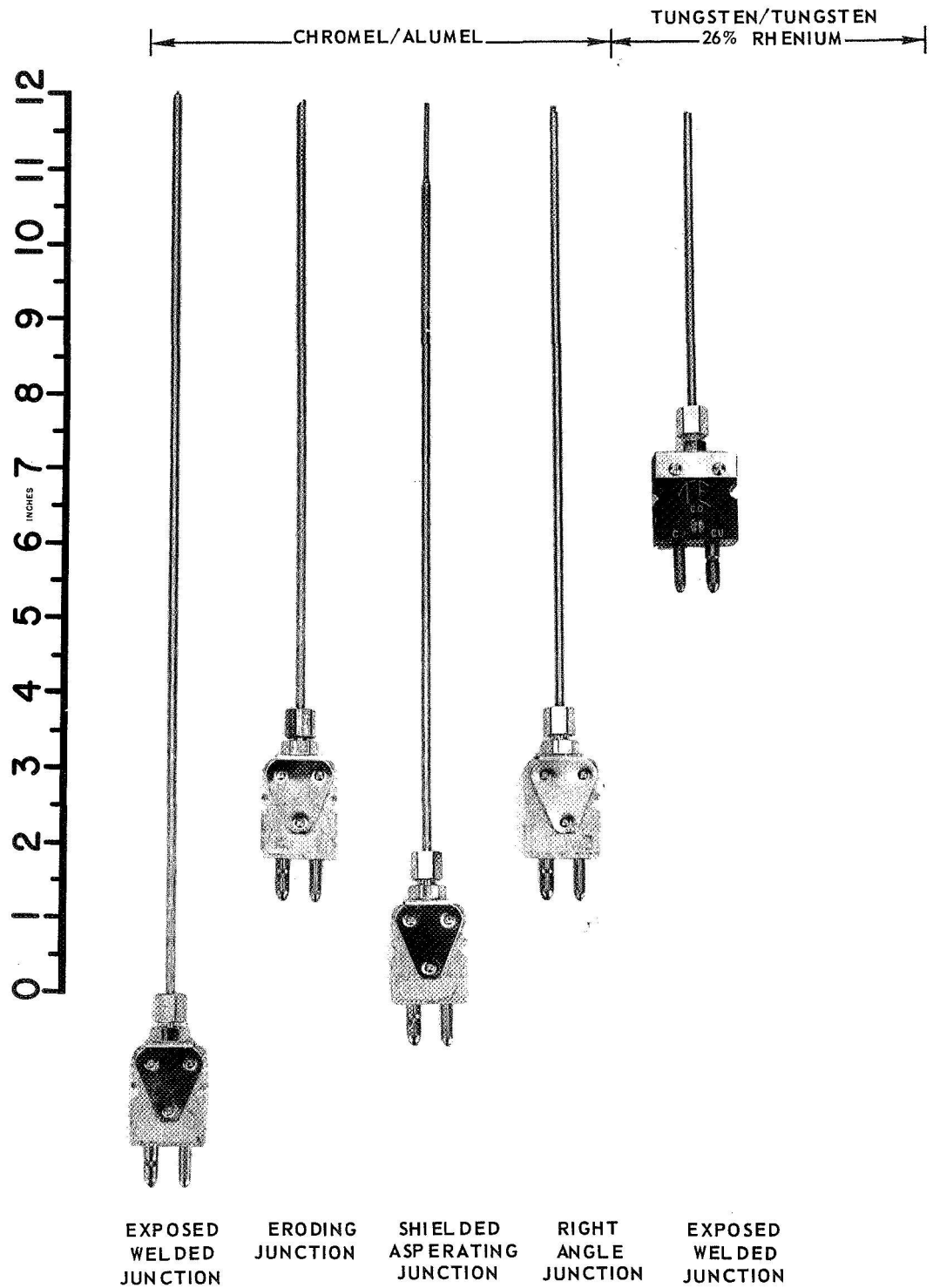
CLOSE-UP PHOTOGRAPHS OF THERMAL JUNCTIONS OF THERMOCOUPLES USED TO MEASURE
LOCAL SIMULATED PROPELLANT EXIT TEMPERATURE

ALSO SEE FIG. 13

FIG. 15

SCHEMATIC DIAGRAM OF SIMULATED PROPELLANT FLOW SYSTEM AND HIGH-PRESSURE SEED DISPERSAL SYSTEM

INNER ARGON BUFFER FLOW

OUTER ARGON BUFFER FLOW

ARGON CARRIER FLOW

BYPASS FLOW

SEEDED ARGON FLOW

VARIABLE-SPEED DRIVE MOTOR

AGITATOR BLADES

SEED SUPPLY (CARBON)

HIGH-PRESSURE CANISTER (3000 PSIG)

HIGH-PRESSURE SEED DISPERSAL SYSTEM

TO EXHAUST SYSTEM

WATER-COOLED FUSED SILICA TUBES

SEEDED ARGON FLOW

INNER ARGON BUFFER FLOW

OUTER ARGON BUFFER FLOW

LOCATION OF RADIANT ENERGY SOURCE

SEEDED SIMULATED PROPELLANT FLOW SYSTEM

KEY	
R	PRESSURE REGULATOR
⬭	FLOWMETER
⊗	CONTROL VALVE
⊘	PRESSURE GAUGE

FIG. 16

DETAILS OF INLET GEOMETRY USED IN PROPELLANT HEATING TESTS

GEOMETRY IS AXISYMMETRIC
X,Y, AND Z DENOTE LOCATIONS OF POROUS FOAM MATERIAL
①, ②, ③, AND ④ DENOTE INTERCHANGEABLE PARTS (SEE FIG. 17)
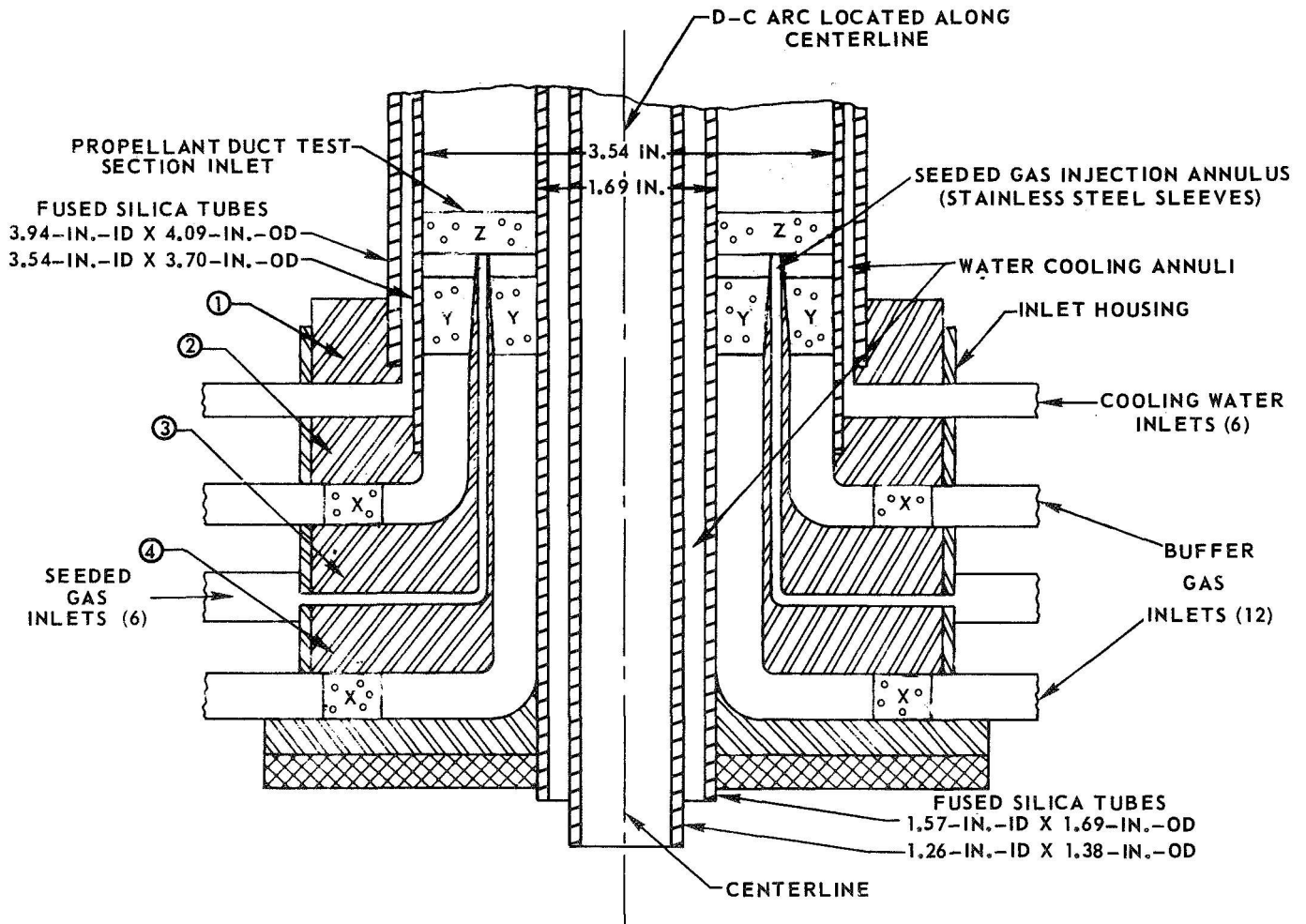
PHOTOGRAPH OF COMPONENTS OF PROPELLENT HEATING INLET

COMPONENTS DENOTED BY ①, ②, ③, AND ④ CORRESPOND TO INTERCHANGEABLE PARTS NOTED IN FIG. 16

BUFFER GAS (12), SEED GAS (6), AND COOLING WATER INLET TUBES (6)

INLET HOUSING

INNER SEED–ANNULUS INSERT ④

INNER SEAL–RING ASSEMBLY ②

CLAMP RING (NOT SHOWN IN FIG. 15)

POROUS FOAM MATERIAL

OUTER SEED–ANNULUS INSERT ③

OUTER SEAL–RING ASSEMBLY ①
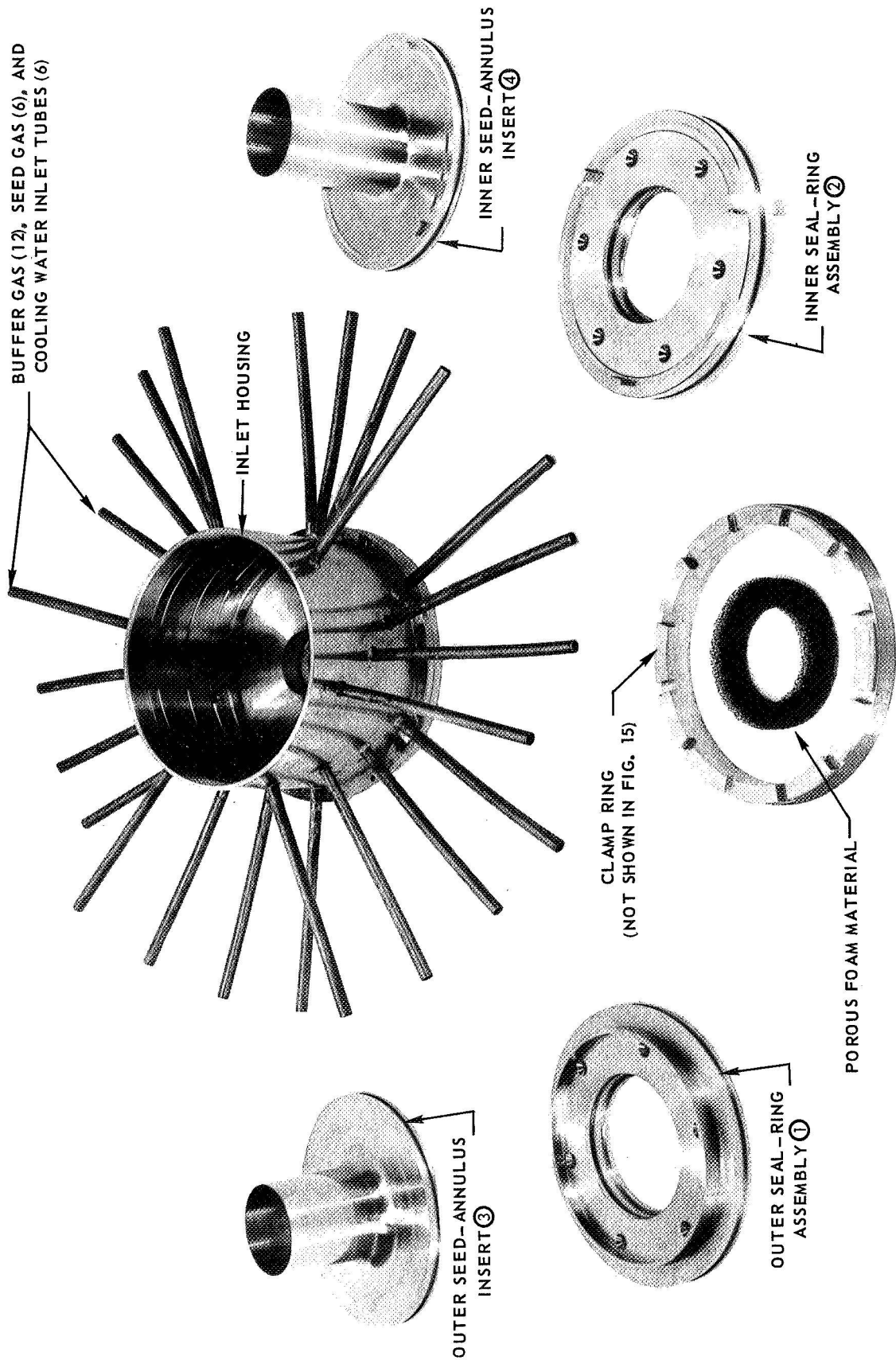
TYPICAL RESULTS OBTAINED IN COLD — FLOW SEEDED PROPELLANT STREAM TEST WITH ANNULAR PROPELLANT DUCT CONFIGURATION

PROPELLANT STREAM VELOCITY = 5.0 FT/SEC

(a) PHOTOGRAPH SHOWING STREAMERS IN SEEDED STREAM
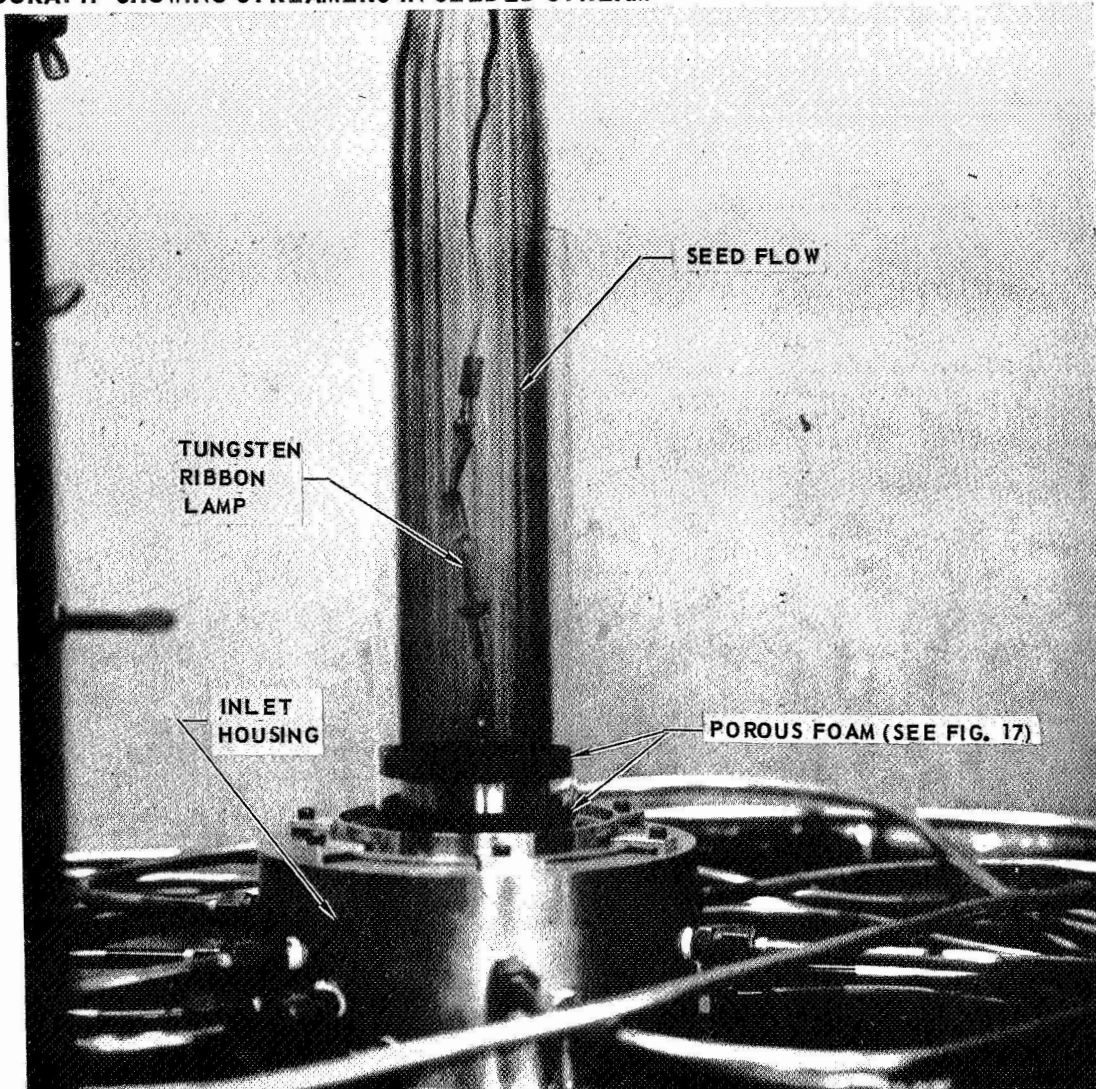
(b) TYPICAL RADIOMETER TRACE OBTAINED WITH SEEDS FLOWING
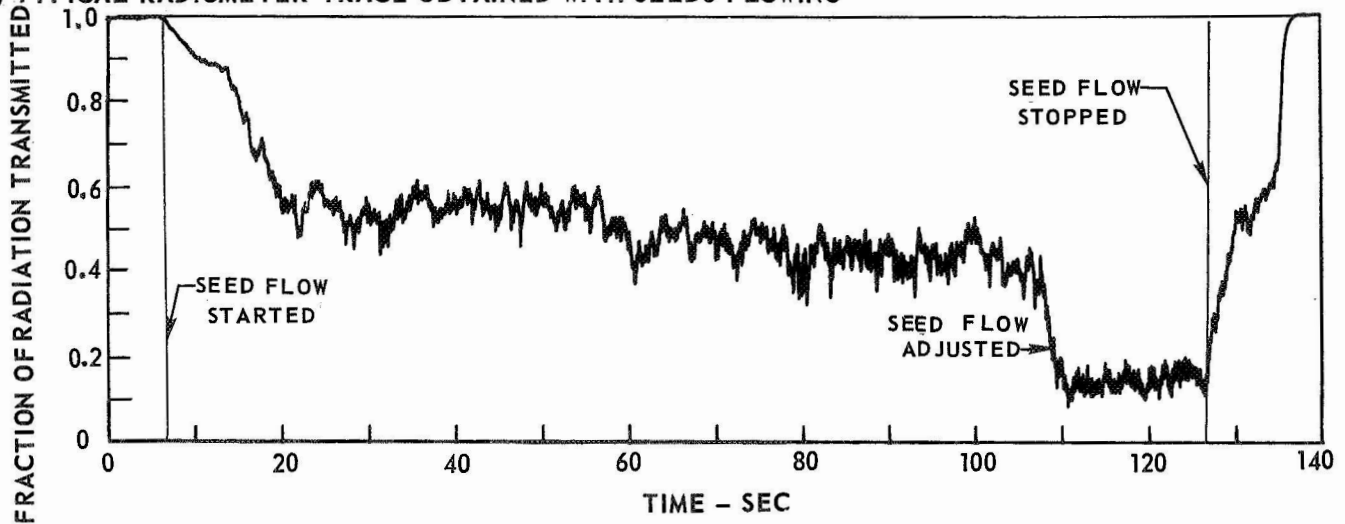
FIG. 19

SCHEMATIC DIAGRAM OF SYSTEM USED TO MEASURE MASS ATTENUATION COEFFICIENT OF DISPERSED CARBON

ARROWS DENOTE DIRECTION OF FLOW

ARGON SUPPLY

PRESSURE GAUGE

6 IN.

SEED DISPERSAL CHAMBER

SWIRL FLOW

MIXING CHAMBER

POWER SUPPLY

TUNGSTEN FILAMENT LAMP (DXW–1KW)

ORIFICE PLATE

0.125 IN.

5 IN.

EXHAUST VENT

SEEDED STEAM

SEED DUCT EXIT PLANE

COLLIMATING TUBE

0.426–IN.–ID

ORIFICE HOLDER

RADIOMETER (SEE FIG. 9)

KEY

CONTROL VALVE

FLOWMETER
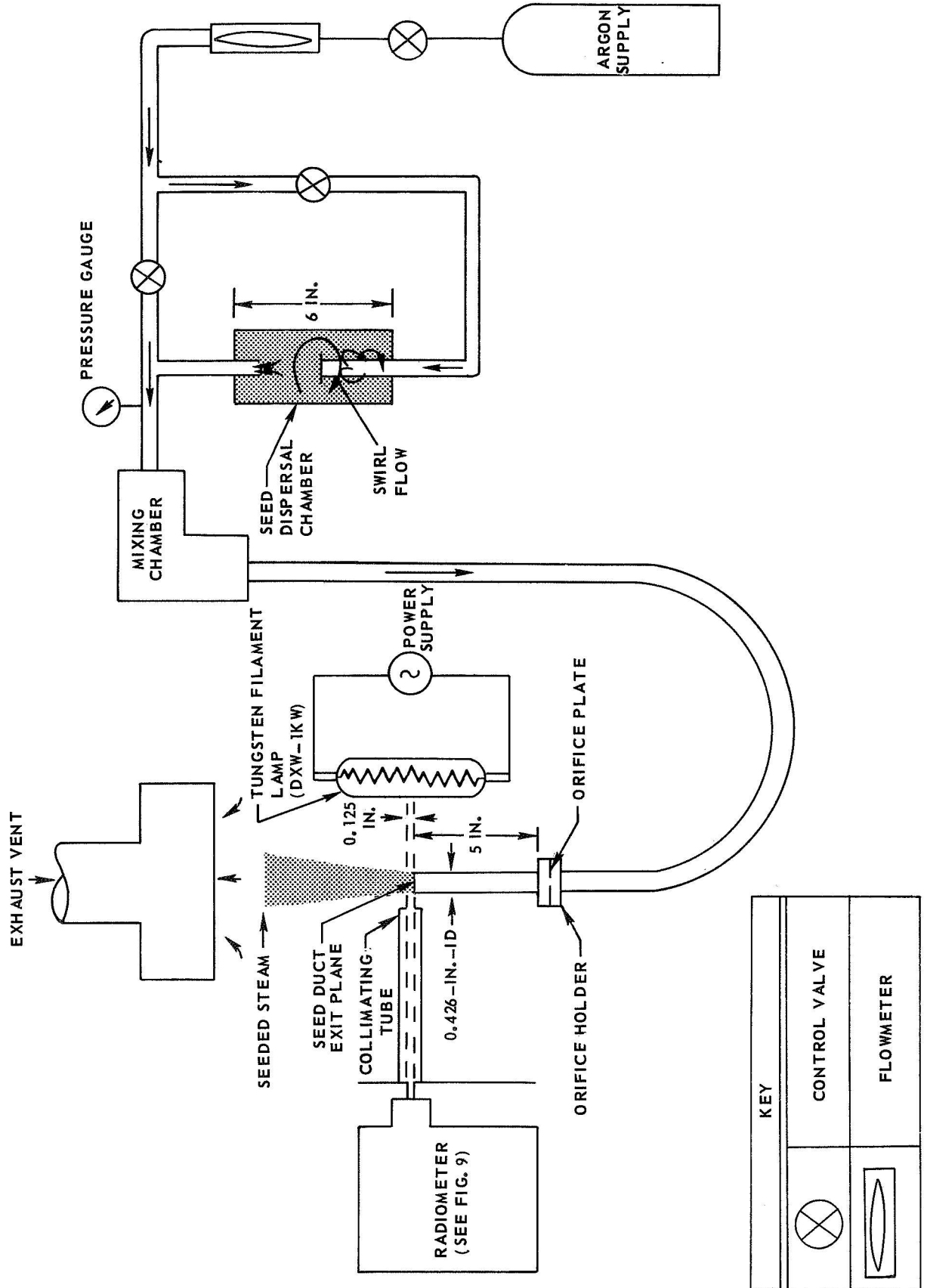
RADIOMETER TRACE AND TEST CONDITIONS FOR MASS
ATTENUATION PARAMETER EXPERIMENTS

SEE FIG. 19 FOR DIAGRAM OF TEST EQUIPMENT

(a) TEST CONDITIONS

ORIFICE DIA-IN	PRESSURE DROP - PSI	ARGON FLOW RATE - LB/SEC X 10^4
———	———	7.08-7.34
0.052	74-78	7.08-7.34
0.040	111-134	7.31-7.42
0.020	390-400	6.20-6.31

(b) RADIOMETER TRACE

FRACTION OF RADIATION TRANSMITTED, η_T

TIME, T – SEC
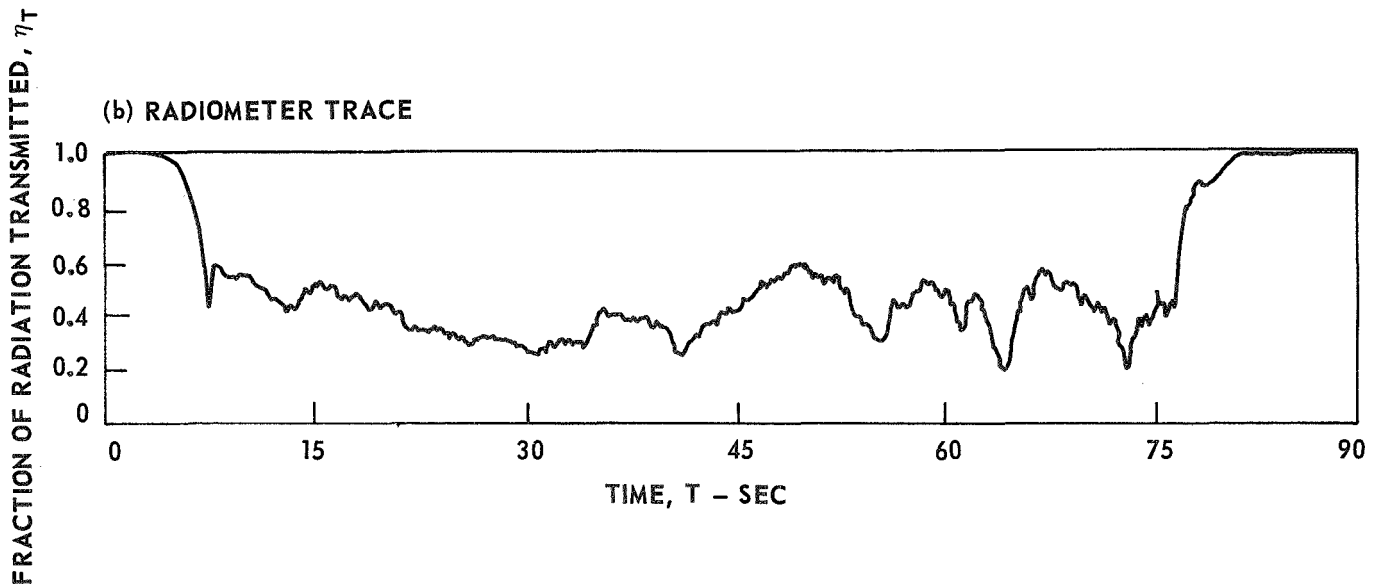
EFFECT OF ORIFICE PRESSURE DROP ON MASS ATTENUATION COEFFICIENT OF DISPERSED CARBON

SEE FIG. 20(a) FOR ORIFICE SIZES AND ARGON FLOW RATES

SEE FIG. 19 FOR DIAGRAM OF TEST EQUIPMENT
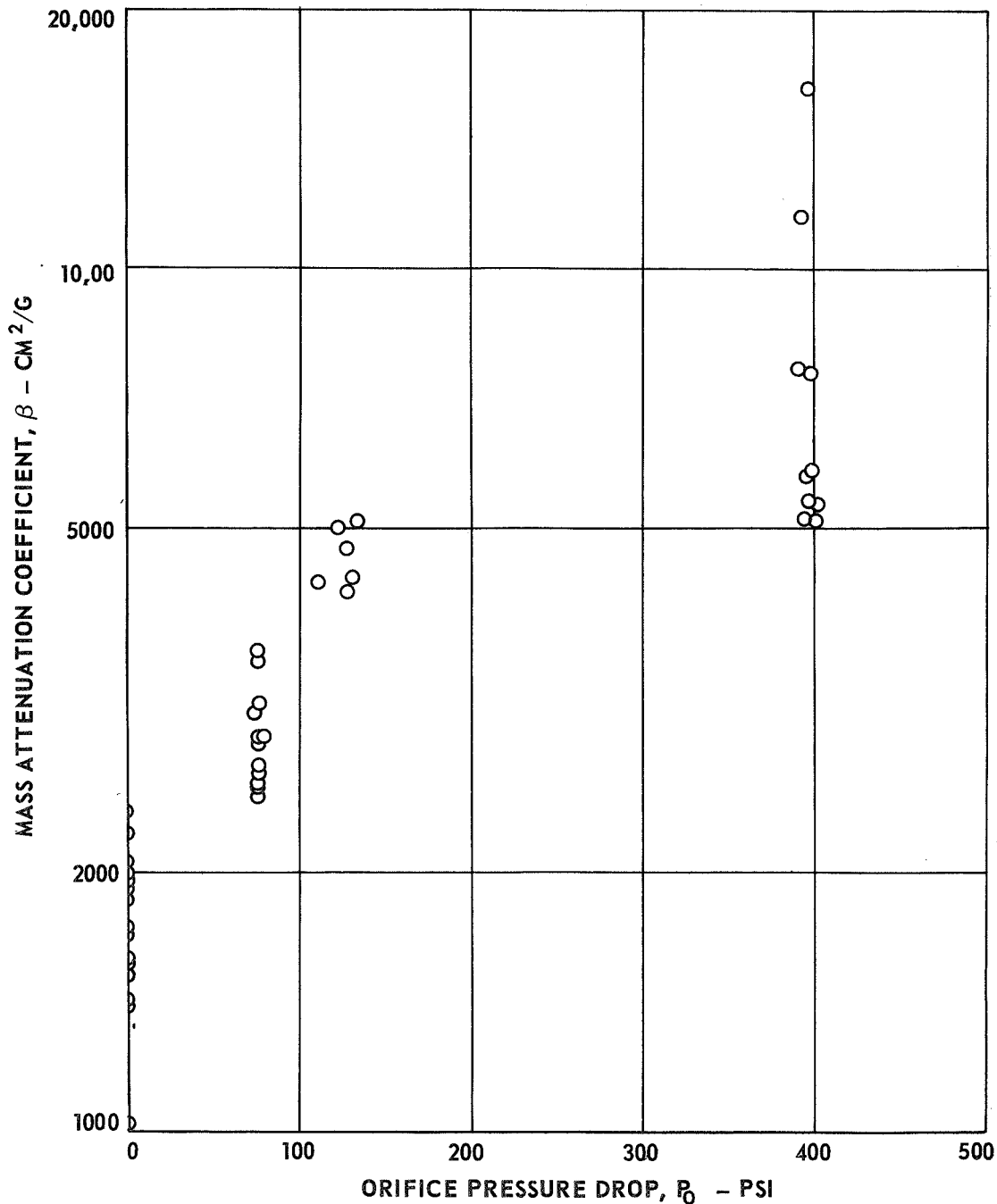
ELECTRON PHOTOMICROGRAPHS OF DISPERSED CARBON

SEE FIG. 19 FOR DIAGRAM OF TEST EQUIPMENT

SEE FIG. 21 FOR MASS ATTENUATION RESULTS

SAMPLED FROM FLOWING DISPERSION

LENGTH SCALE |←———— 1μ ————→|

(a) NO ORIFICE
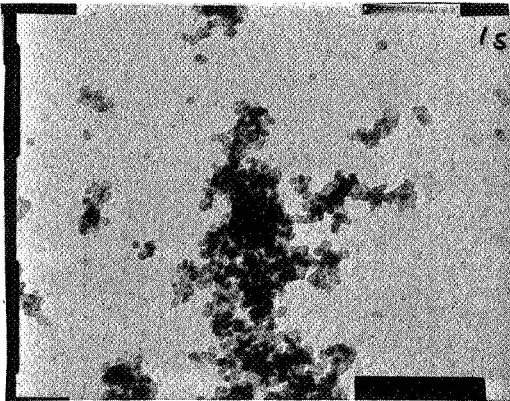
(b) ORIFICE DIA = 0.040 IN.
ORIFICE PRESSURE DROP = 130 PSI
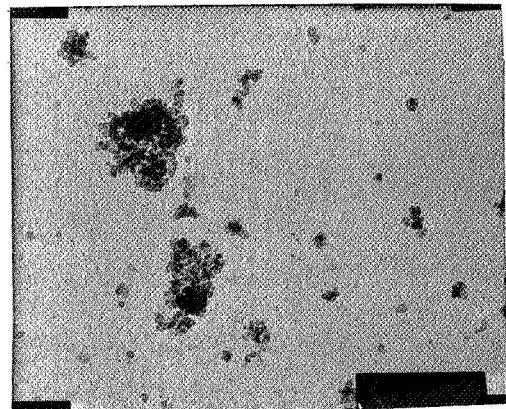
(c) ORIFICE DIA = 0.020 IN.
ORIFICE PRESSURE DROP = 396 PSI

FIG. 23
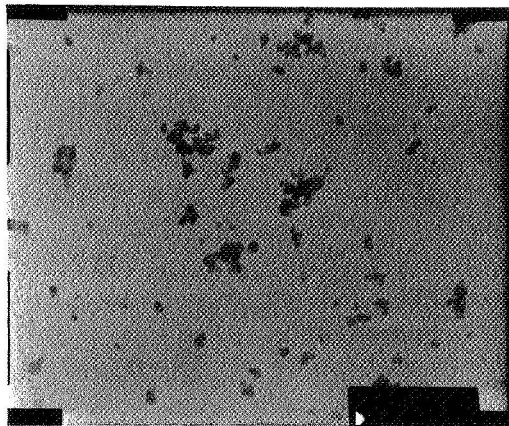
EFFECT OF PROPELLANT STREAM SEED DENSITY ON FRACTION OF RADIATION ABSORBED BY SEEDED GAS

SEE FIG. 20(a) FOR ORIFICE SIZES AND ARGON FLOW RATES

SEE FIG. 19 FOR DIAGRAM OF TEST EQUIPMENT

$$\eta_A = 1 - e^{-\rho_s \beta \ell}$$

NLB DESIGN VALUE
$\rho_s = 2.1 \times 10^{-4}$ g/CM^3
$\ell = 2.84$
$\beta = 5000$ CM^2/g

$\beta = 50,000$ CM^2/g

SEED DENSITY PARAMETER, $\rho_s \ell$ – g/CM^2

FRACTION OF RADIATION ABSORBED BY PROPELLANT STREAM, η_A

FIG. 24
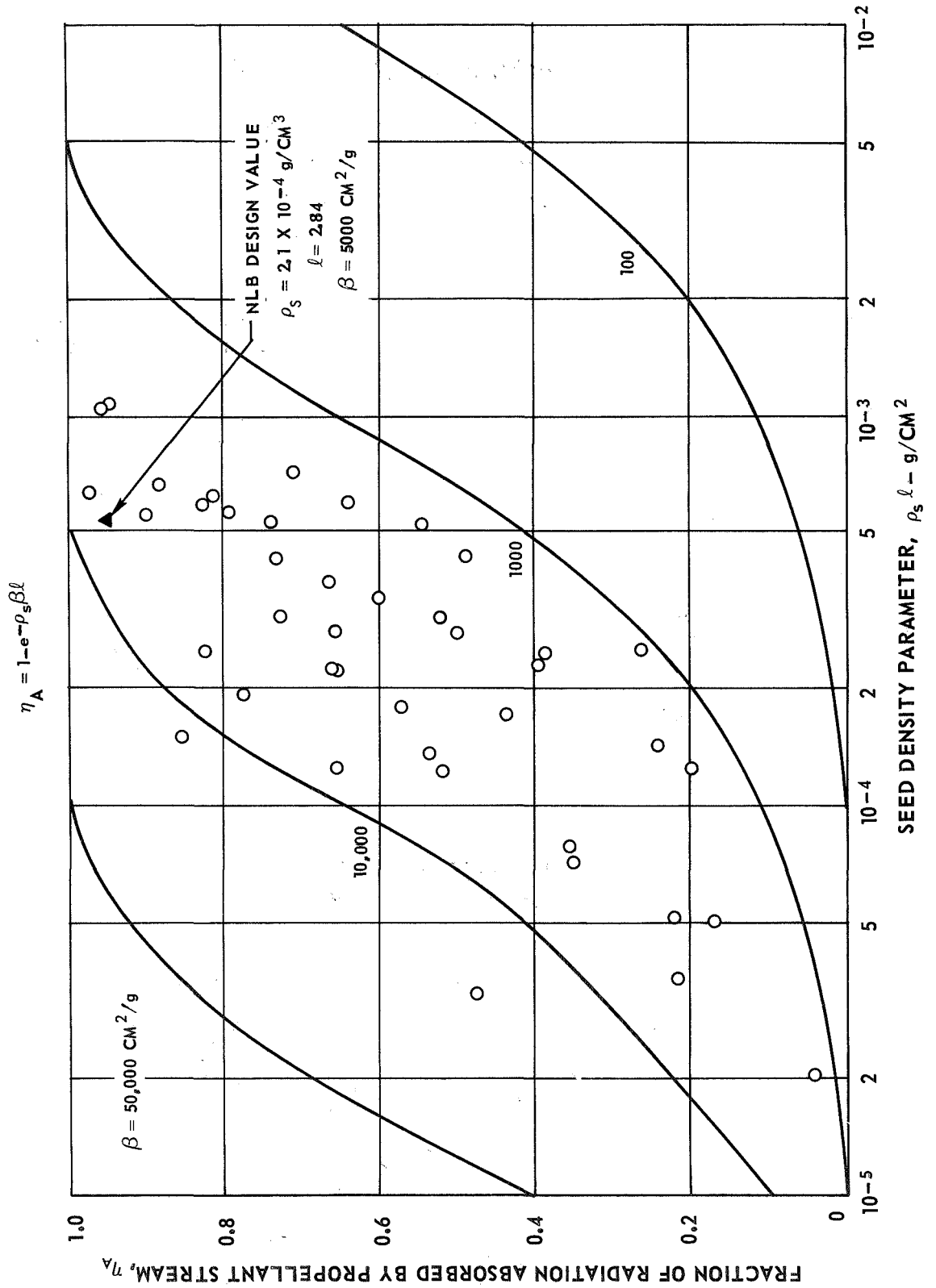
COLD — FLOW TEST OF COMPLETE D–C ARC PROPELLANT
HEATING CONFIGURATION

SEE FIG. 3 FOR DETAILS OF TEST CONFIGURATION

FIG. 25
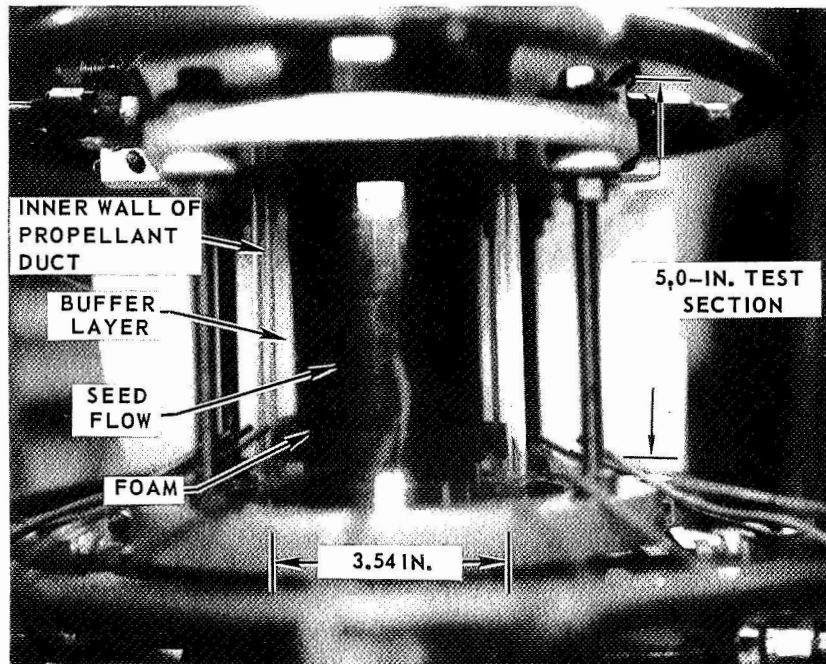
TYPICAL HOT-FLOW PROPELLANT HEATING TEST

SEE FIG. 3 FOR TEST CONFIGURATION

SEE TABLE II FOR SUMMARY OF TEST RESULTS

(a) PHOTOGRAPHS OF TEST SECTION

ARC ONLY (BEFORE)   SEEDS FLOWING (DURING)   ARC ONLY (AFTER)
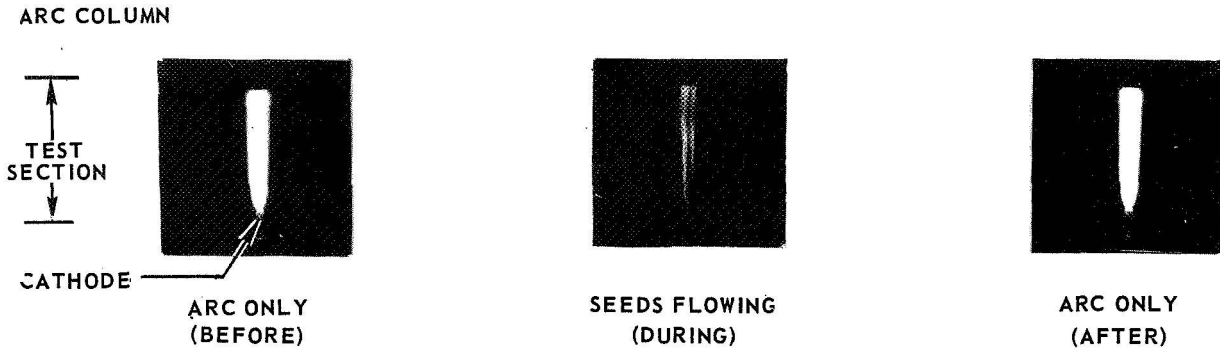
(b) RADIOMETER TRACE
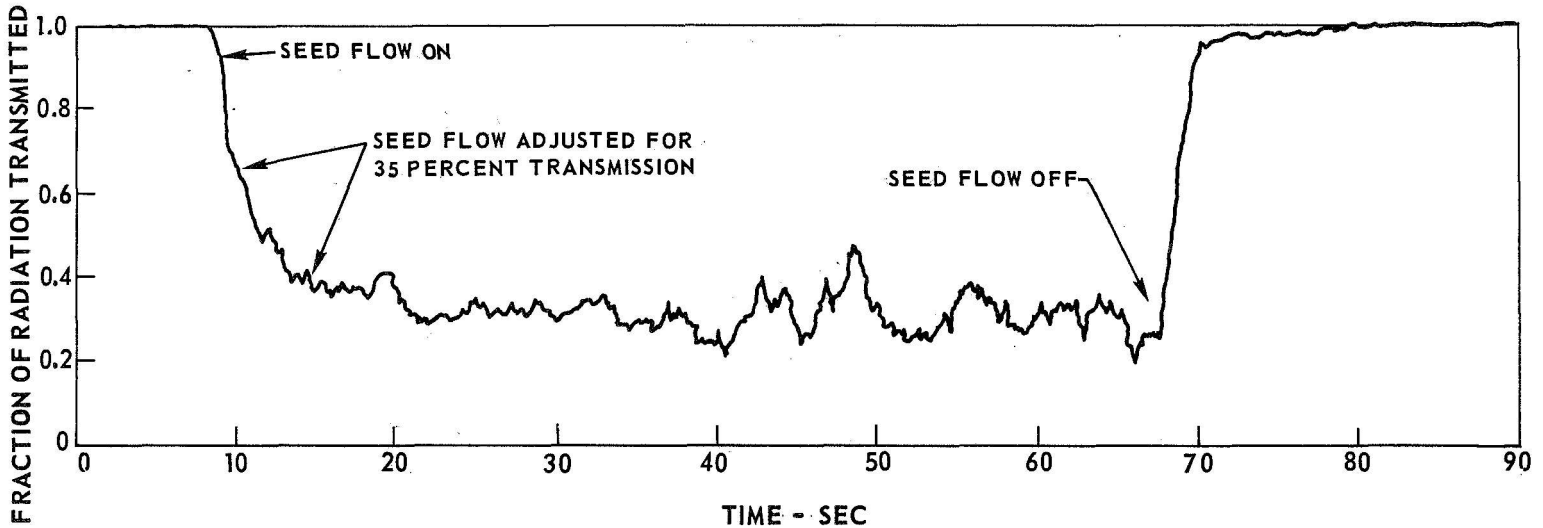
(c) CORRESPONDING TEST CONDITIONS AND MEASUREMENT RESULTS

PRESSURE IN PROPELLANT DUCT	1.0 ATM
PROPELLANT STREAM VELOCITY	5.0 FT/SEC
PROPELLANT STREAM WEIGHT FLOW RATE*	0.033 LB/SEC
PROPELLANT STREAM INLET TEMPERATURE	525 R
LOCAL TEMPERATURE MEASURED BY THERMOCOUPLE AT PROPELLANT DUCT EXIT WITH SEEDS	1930 R
AVERAGE TEMPERATURE AT PROPELLANT DUCT EXIT WITH SEEDS BASED ON CALORIMETER MEASUREMENTS	1169 R
AVERAGE TEMPERATURE AT PROPELLANT DUCT EXIT WITH SEEDS BASED ON RADIATION ATTENUATION MEASUREMENTS	1335 R

*0.030 LB/SEC ARGON AND 0.003 LB/SEC CARBON (SEE TEXT)

FIG. 26

POWER DISTRIBUTION FOR A PROPELLANT HEATING TEST AS DETERMINED BY CALORIMETRY

SEE TABLE I FOR TEST CONDITIONS
SEE TABLE II, RUN NO. 13 FOR TEMPERATURE RESULTS
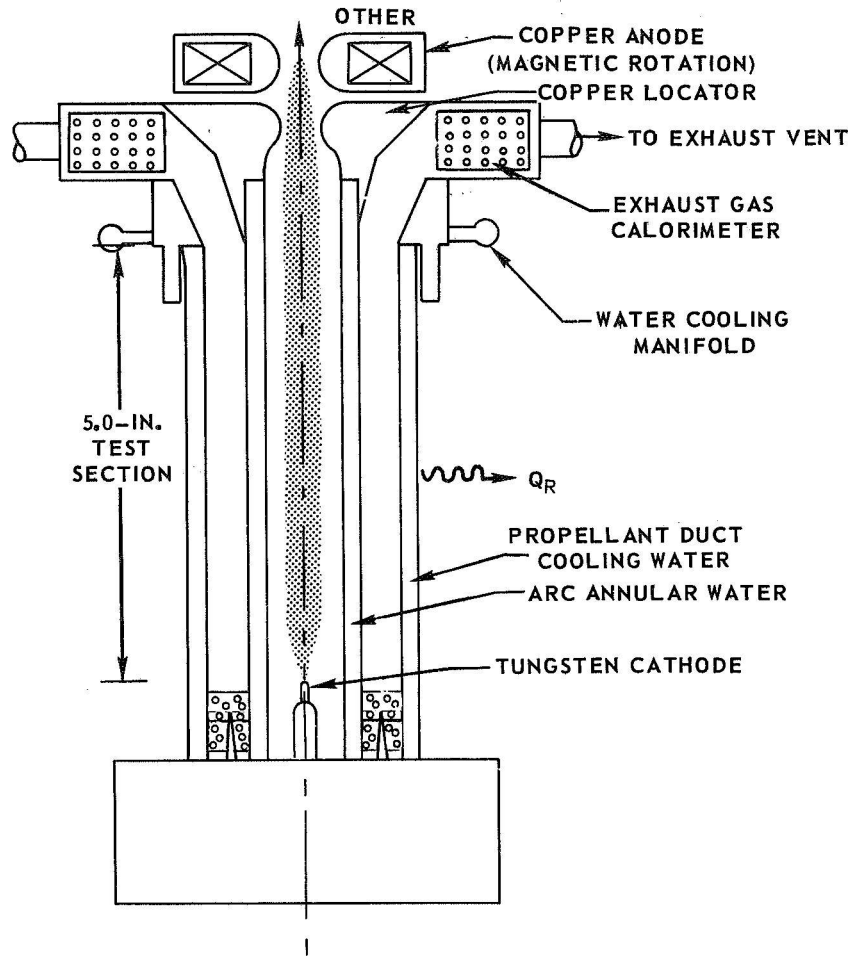
COMPONENT	ARC ONLY (BEFORE) (KW)	SEEDS FLOWING (DURING) (KW)	ARC ONLY (AFTER) (KW)	CHANGE (KW)
CATHODE	0.42	0.42	0.42	0
ANODE	10.6	10.6	10.6	0
LOCATOR	4.76	5.62	4.76	0.86
ARC ANNULAR WATER	4.5	5.3	4.6	0.8
PROPELLANT DUCT ANNULAR WATER	1.05	1.06	1.06	0.01
CALORIMETER WATER	0.34	1.30	0.34	0.96
EXHAUST VENT	0.03	0.43	0.03	0.40
RADIATION	4.72	1.64	4.70	−3.08
TOTAL	26.42	26.37	26.51	−0.05
OTHER	21.58	21.64	21.50	

FIG. 27

VARIATION OF SEEDED SIMULATED PROPELLANT BULK EXIT TEMPERATURE WITH TOTAL RADIATION INCIDENT ON PROPELLANT STREAM
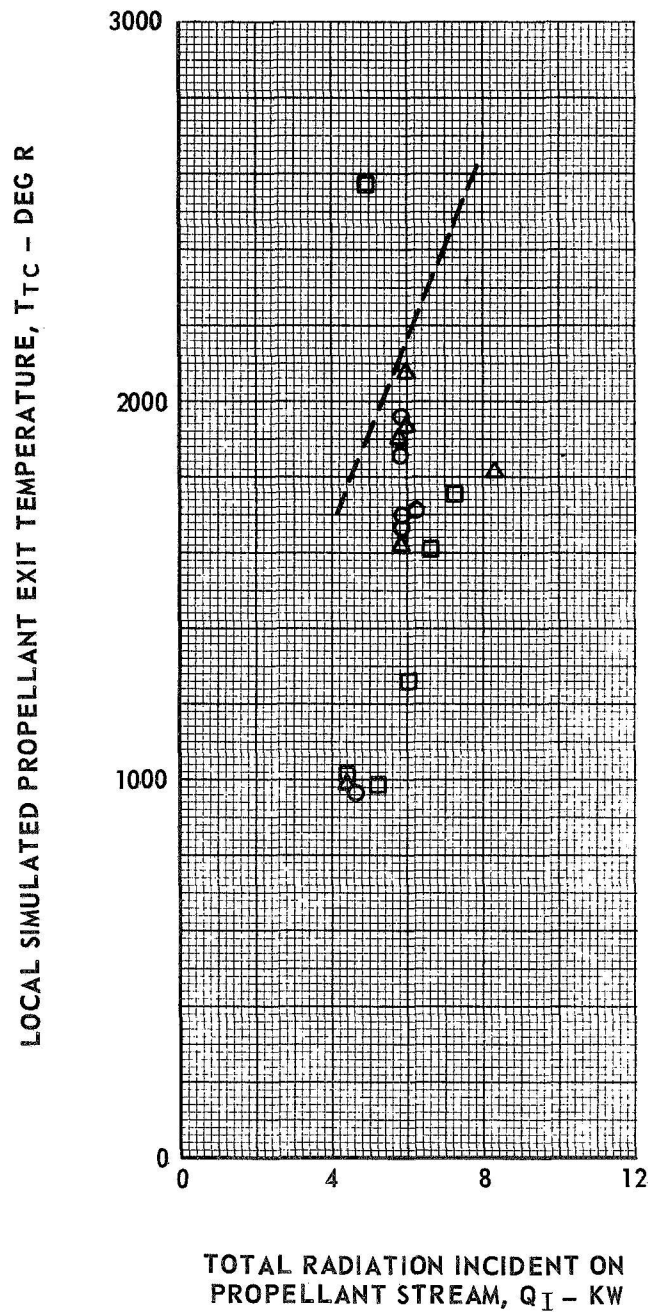
SEE TABLES I AND II FOR ADDITIONAL DETAILS

FIG.28
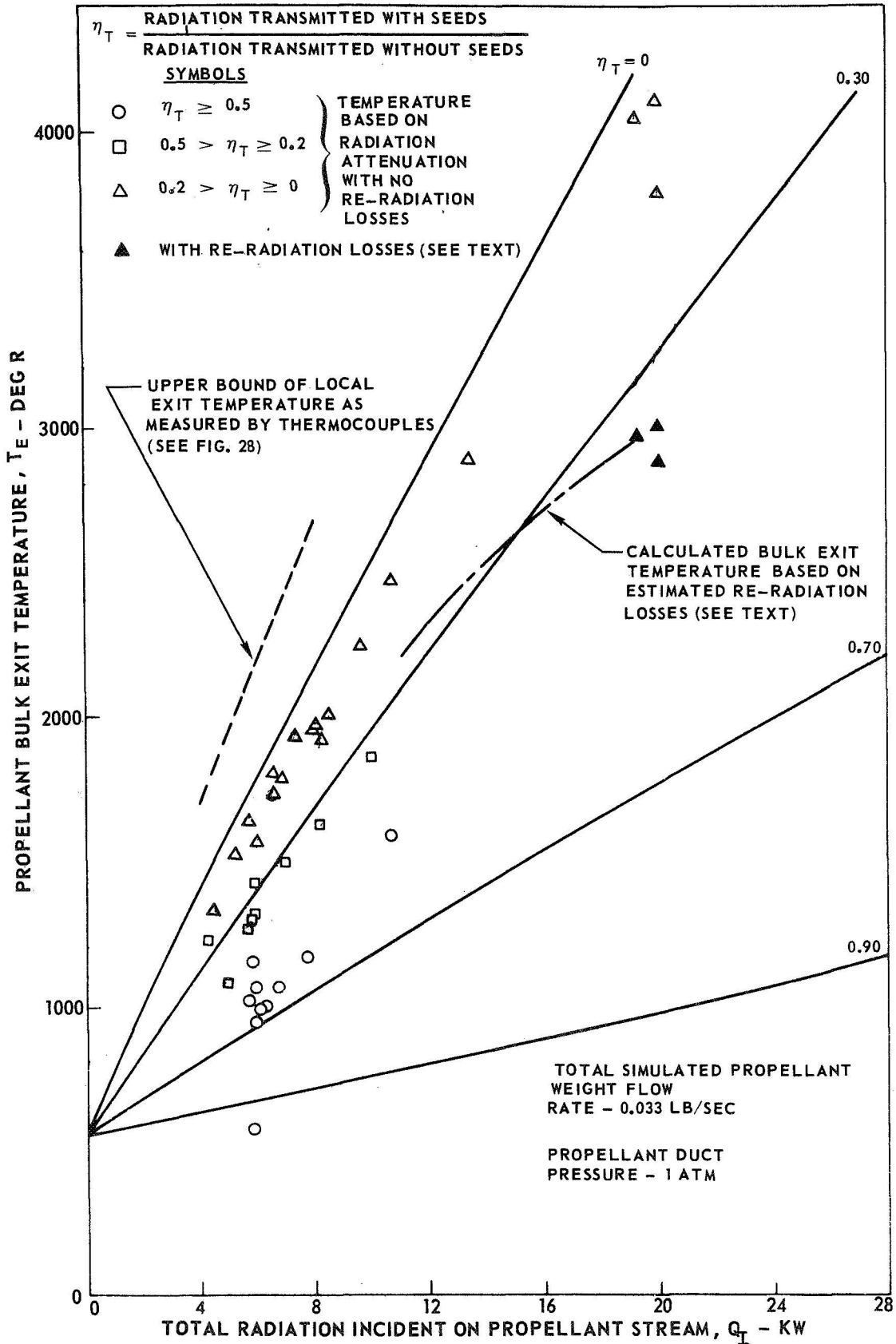
LOCAL SIMULATED PROPELLANT EXIT TEMPERATURE MEASURED BY THERMOCOUPLES VERSUS TOTAL RADIATION INCIDENT ON PROPELLANT STREAM

— — — UPPER BOUND OF LOCAL EXIT TEMPERATURE AS MEASURED BY THERMOCOUPLES (USED IN FIG. 27)

SYMBOLS

O $\eta_T \geq 0.5$

□ $0.5 > \eta_T \geq 0.2$

△ $0.2 > \eta_T \geq 0$

TOTAL RADIATION INCIDENT ON PROPELLANT STREAM, Q_I – KW

FIG. 29

LOCAL PROPELLANT EXIT TEMPERATURES MEASURED USING THERMOCOUPLES

SEE TABLES I AND II FOR TEST CONDITIONS

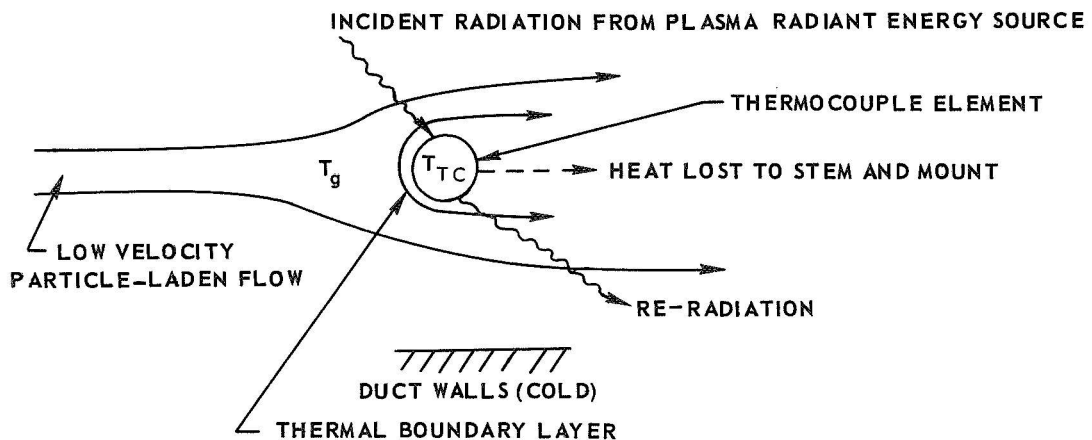## a) TEMPERATURE MEASURED USING THERMOCOUPLES

——————— CALCULATED BULK EXIT TEMPERATURE ASSUMING NO RERADIATION

SYMBOLS

○ $\eta_T \geq 0.5$

□ $0.5 > \eta_T \geq 0.2$

△ $0.2 > \eta_T \geq 0$

X-axis: TOTAL RADIATION ABSORBED BY PROPELLANT STREAM, Q_A – KW

Y-axis: SIMULATED PROPELLANT TEMPERATURE MEASURED USING THERMOCOUPLES, T_{TC} – DEG R
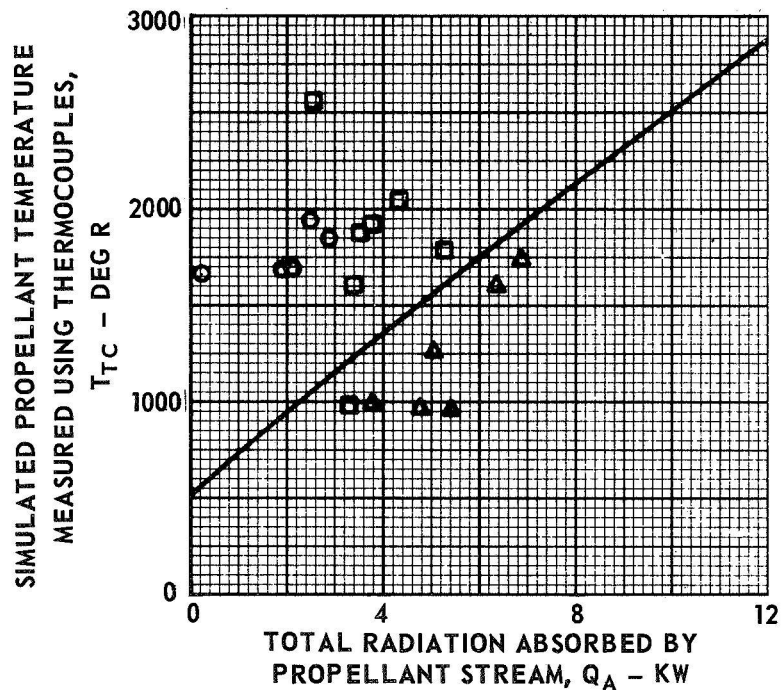
b) FACTORS AFFECTING TEMPERATURE MEASURED USING THERMOCOUPLE

INCIDENT RADIATION FROM PLASMA RADIANT ENERGY SOURCE

THERMOCOUPLE ELEMENT

T_g

T_{TC} – – – → HEAT LOST TO STEM AND MOUNT

LOW VELOCITY PARTICLE-LADEN FLOW

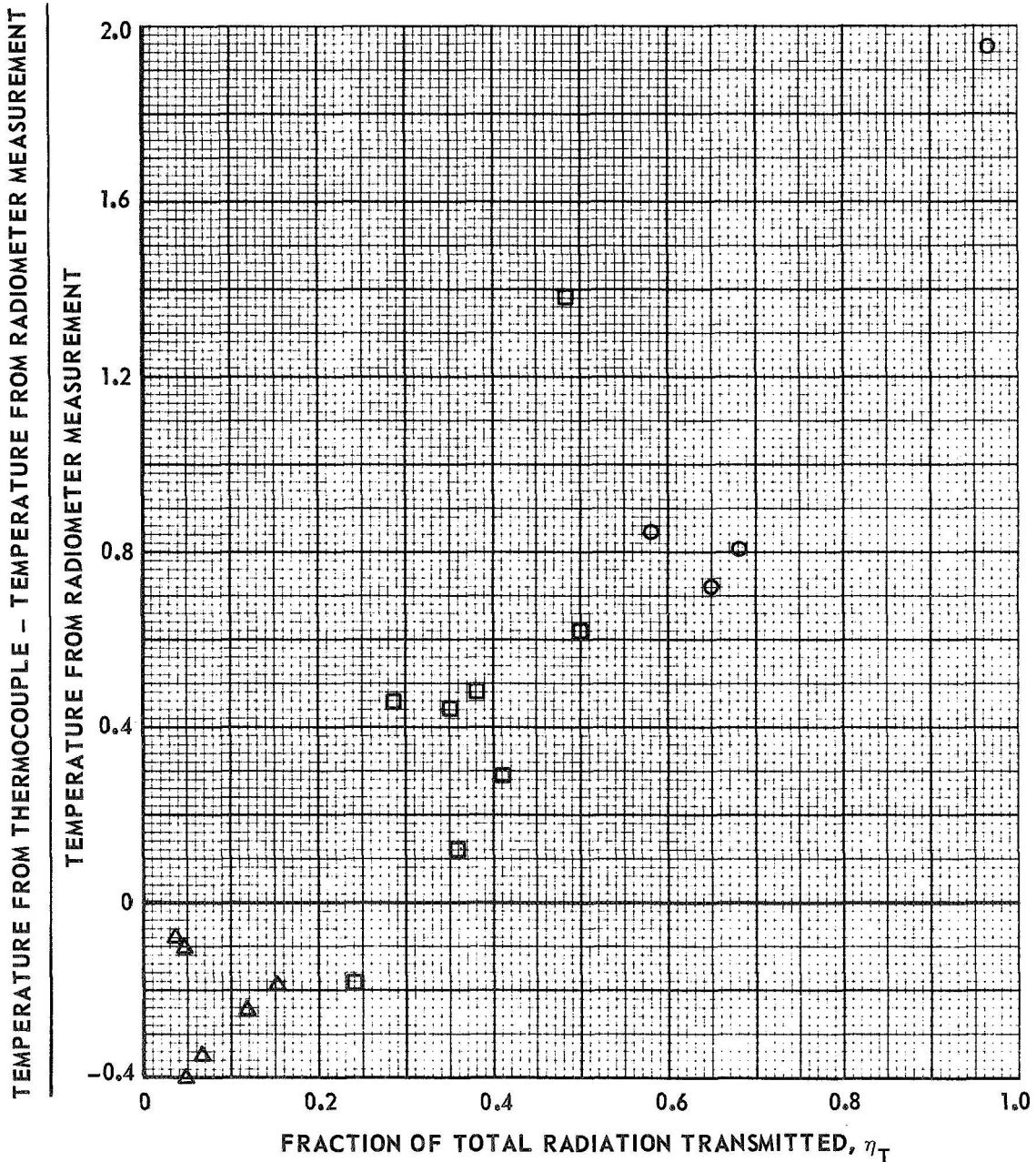RE-RADIATION

DUCT WALLS (COLD)

THERMAL BOUNDARY LAYER

EFFECT OF RADIATION TRANSMITTED BY PROPELLANT STREAM ON DIFFERENCE
BETWEEN TEMPERATURE FROM THERMOCOUPLE AND TEMPERATURE
FROM RADIATION ATTENUATION MEASUREMENT

SEE TABLES I AND II FOR TEST CONDITIONS

SEE TEXT FOR TYPES OF THERMOCOUPLES USED

SYMBOLS

○ $\eta_T \geq 0.5$

□ $0.5 > \eta_T \geq 0.2$
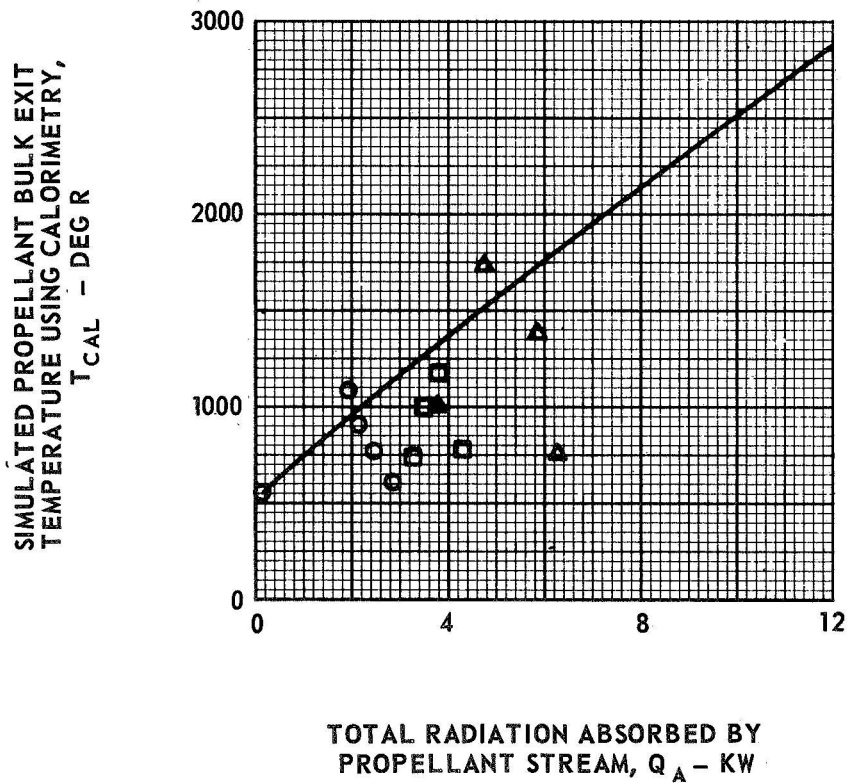
△ $0.2 > \eta_T \geq 0$

FRACTION OF TOTAL RADIATION TRANSMITTED, η_T

TEMPERATURE FROM THERMOCOUPLE – TEMPERATURE FROM RADIOMETER MEASUREMENT

TEMPERATURE FROM RADIOMETER MEASUREMENT

87

SIMULATED PROPELLANT BULK EXIT TEMPERATURE DETERMINED FROM EXHAUST CALORIMETER MEASUREMENTS

SEE TABLES I AND II FOR TEST CONDITIONS
SEE FIG. 12 FOR CALORIMETER DETAILS
Q_A DETERMINED FROM RADIOMETER MEASUREMENTS

——————— CALCULATED BULK EXIT TEMPERATURE ASSUMING NO RE—RADIATION

SYMBOLS

O	$\eta_T \geq 0.5$
□	$0.5 > \eta_T \geq 0.2$
△	$0.2 > \eta_T \geq 0$

TOTAL RADIATION ABSORBED BY PROPELLANT STREAM, Q_A – KW

FIG. 32

EFFECT OF ATTENUATION PARAMETER ON FRACTION OF RADIATION
ABSORBED BY SIMULATED PROPELLANT STREAM

η_A MEASURED BY RADIOMETER (SEE FIG. 9)

ATTENUATION PARAMETER CALCULATED FROM THE FOLLOWING RELATIONSHIP:

$$\eta_A = 1 - e^{\rho_s \beta \ell}$$
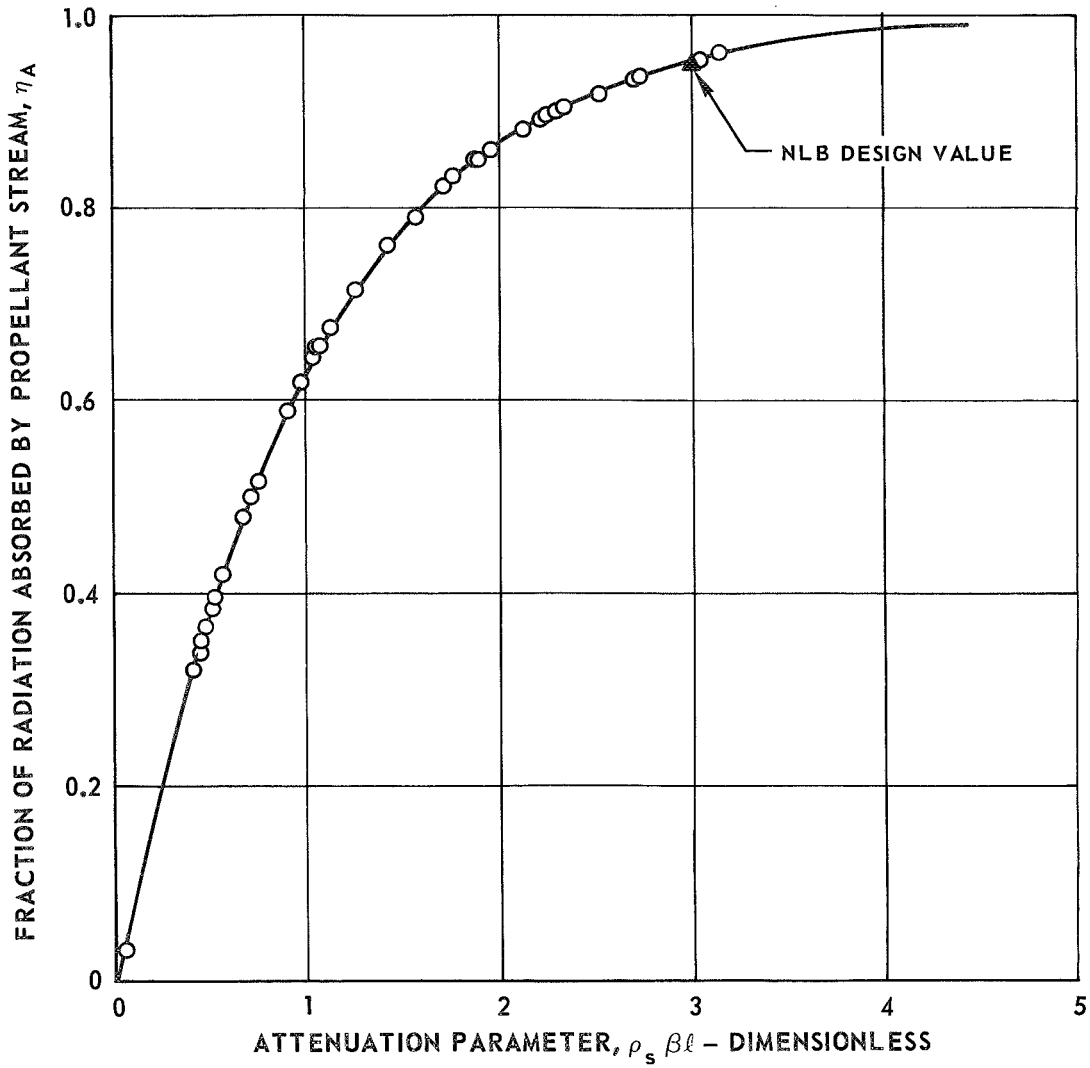
COMPARISON OF CALCULATED AXIAL TEMPERATURE DISTRIBUTION
WITH AND WITHOUT RE–RADIATION FOR DATA POINT WITH HIGHEST
EXIT TEMPERATURE

SEE TABLE II, RUN NUMBER 37

— — WITH RE–RADIATION (SEE APPENDIX B)

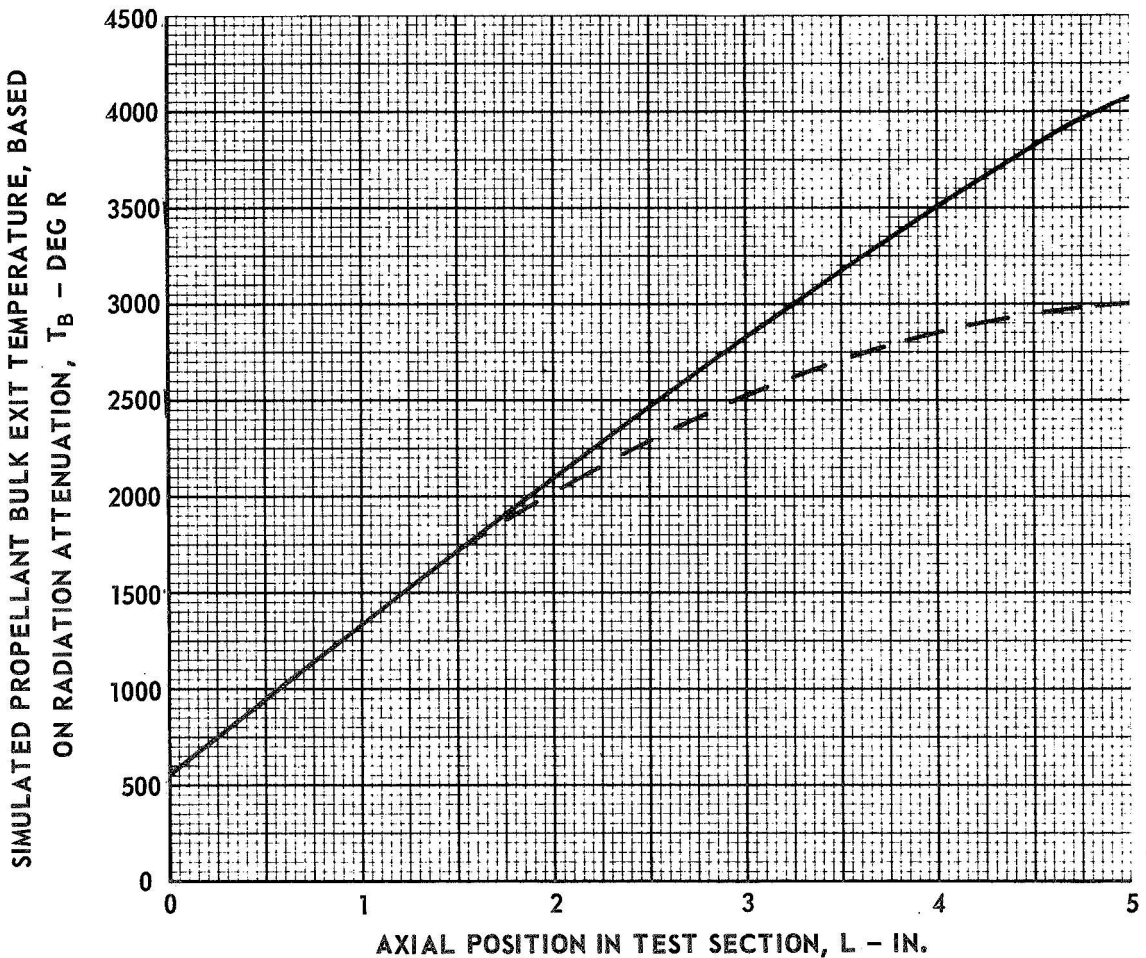———— WITHOUT RE–RADIATION

PRESSURE, 1.0 ATM

RADIATION INCIDENT ON PROPELLANT STREAM, Q_{INC} = 20.0 KW

FRACTION OF RADIATION TRANSMITTED, η_t = 0.064

RADIATION ABSORBED BY PROPELLANT STREAM = 18.72 KW
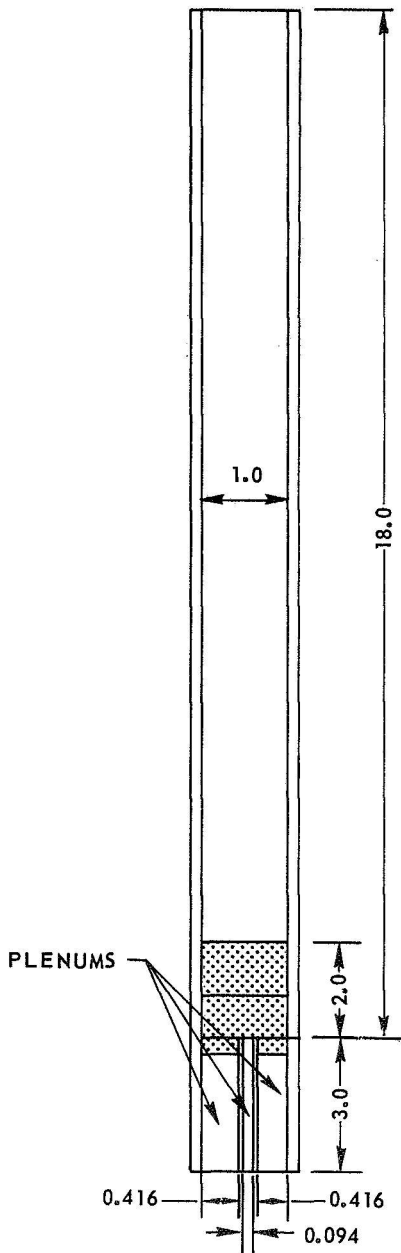
INLET VELOCITY = 5.0 FT/SEC

TOTAL PROPELLANT FLOW RATE = 0.033 LB/SEC

FIG. 34

RESULTS OF SMOKE FLOW VISUALIZATION TESTS WITH THE TWO—DIMENSIONAL PROPELLANT DUCT

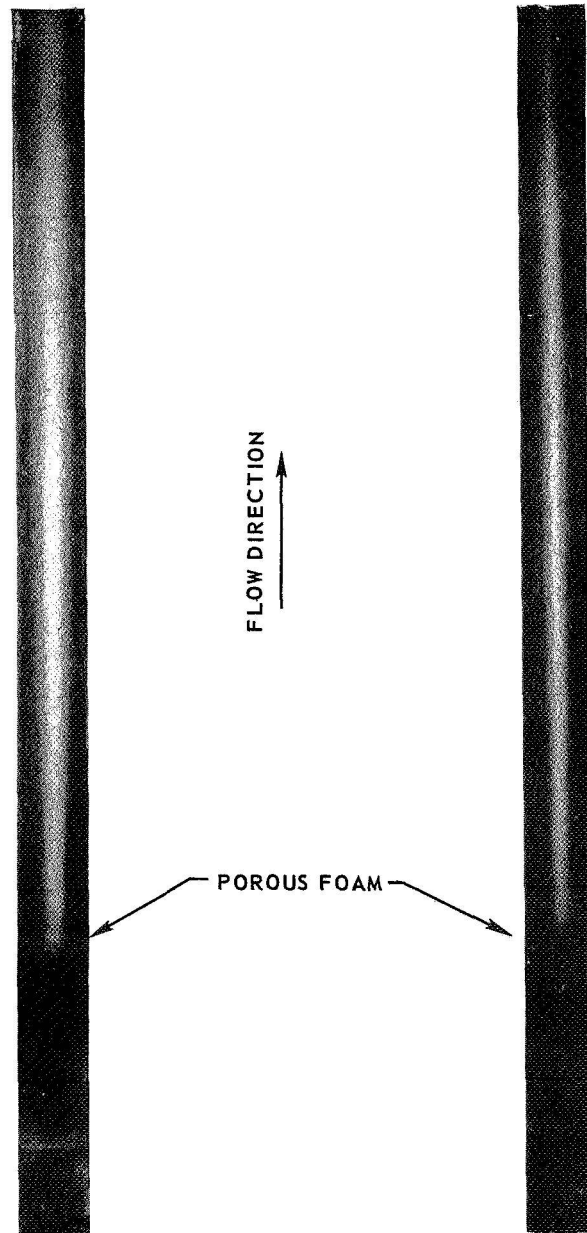ALL DIMENSIONS IN INCHES
DUCT CROSS SECTION, 1.0 IN. X 3.0 IN.

a) DUCT GEOMETRY

b) FLOW VISUALIZATION PHOTOGRAPHS

FIG. 35

CARBON DIOXIDE CONCENTRATION DISTRIBUTIONS AT VARIOUS AXIAL POSITIONS IN TWO-DIMENSIONAL PROPELLANT DUCT

LINE	LOCATION
── ─ ── ─	UPSTREAM OF FOAM
──○──	1 IN. DOWNSTREAM OF FOAM
──✕─	15 IN. DOWNSTREAM OF FOAM
──── ──	15 IN. DOWNSTREAM—THEORETICAL
── ──	60 IN. DOWNSTREAM—THEORETICAL

SEE FIG. 34(a) FOR CONFIGURATION DETAILS

OUTER STREAMS—ARGON GAS

INNER STREAM—CARBON DIOXIDE GAS

VELOCITY = 9 FT/SEC

FIG. 36
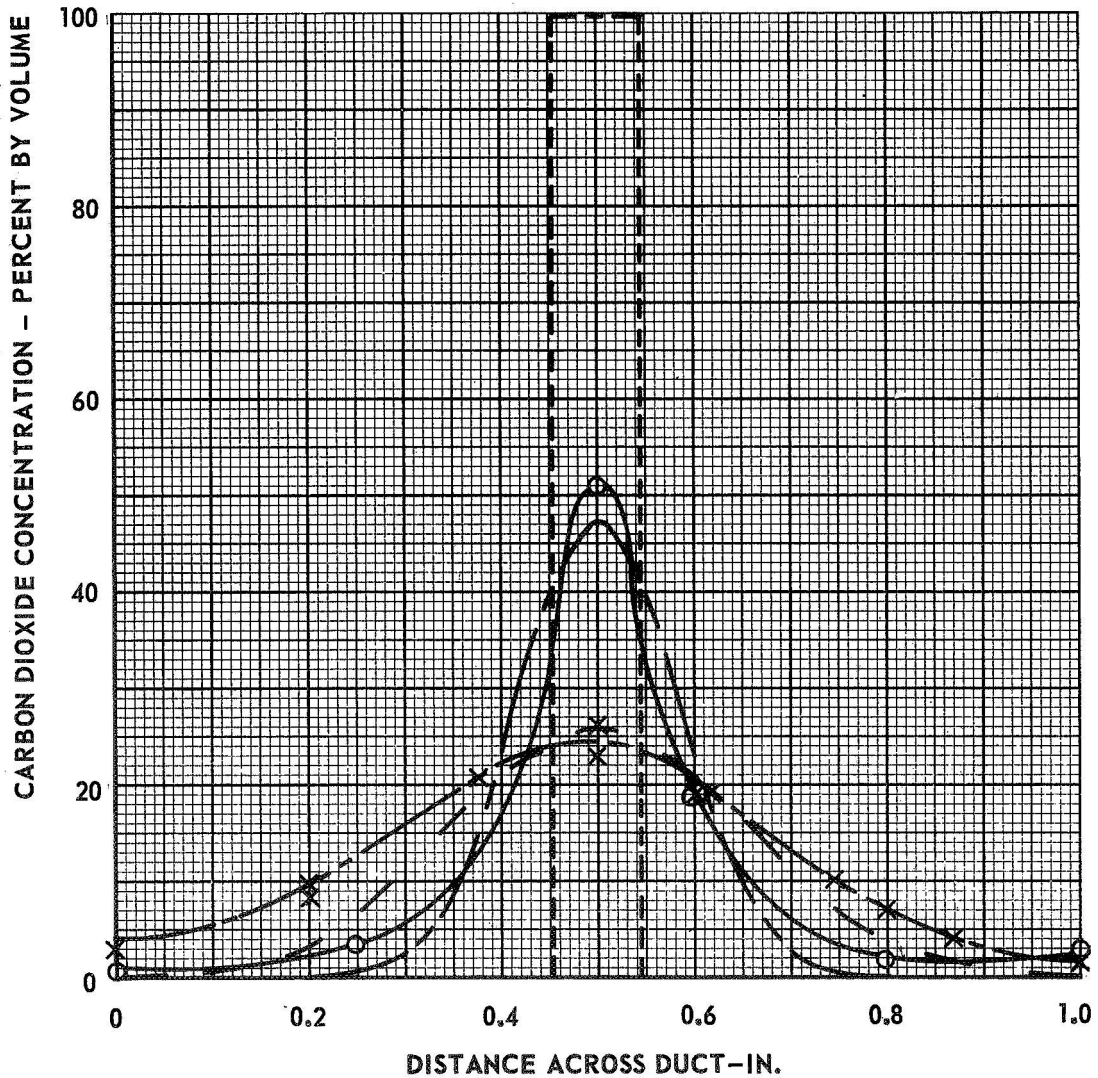
SKETCH AND PHOTOGRAPHS OF THREE-STREAM TWO-DIMENSIONAL PROPELLANT DUCT WITH POROUS FOAM DOWNSTREAM OF STREAM DIVIDERS
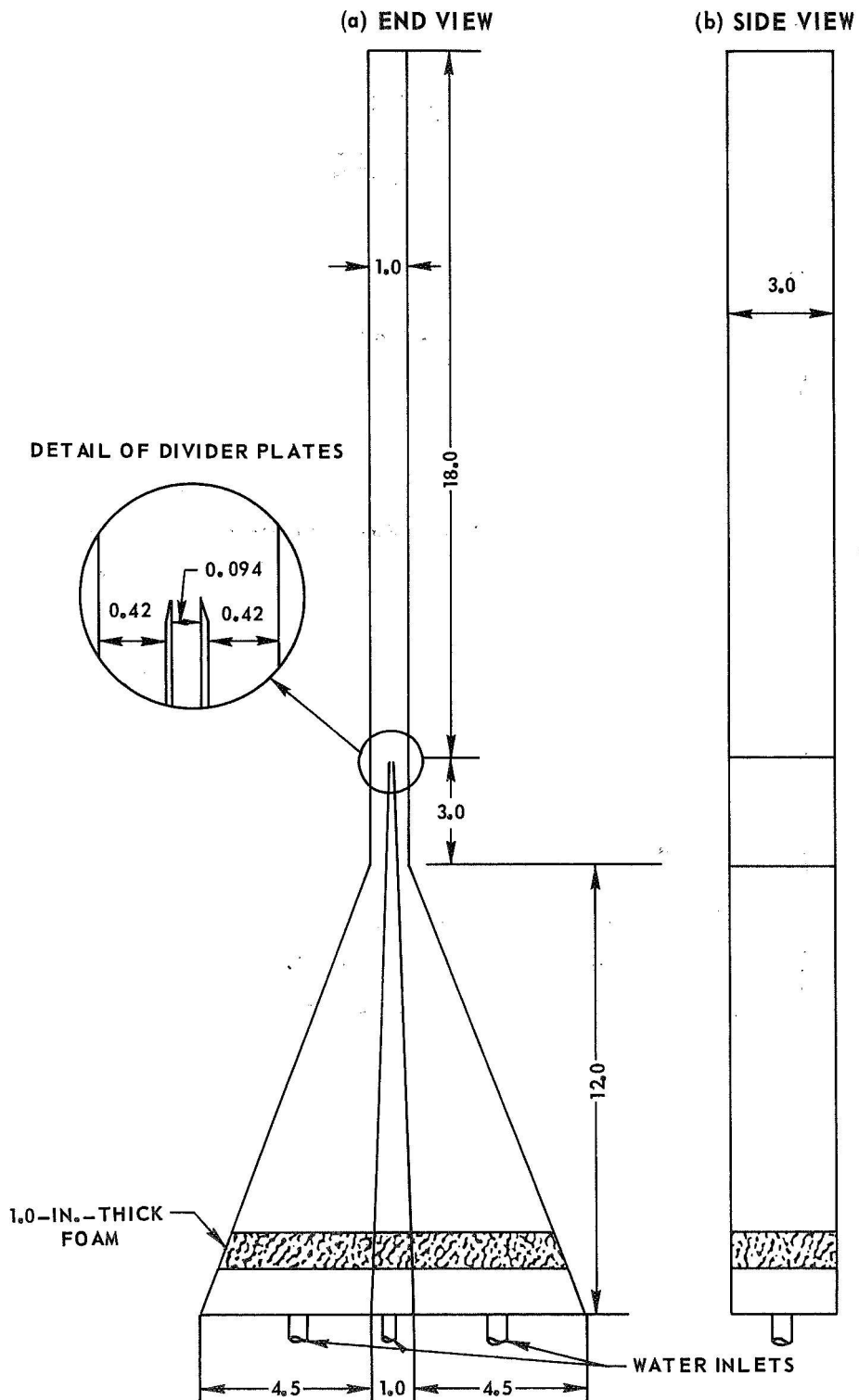
ALL DIMENSIONS IN INCHES

(a) DUCT GEOMETRY (END VIEW)

(b) FLOW VISUALIZATION PHOTOGRAPHS (WATER WITH DYE)

FLOW DIRECTION

END VIEW

SIDE VIEW

POROUS FOAM

STREAM DIVIDER PLATES

18.0

1.0

3.0

FIG. 37
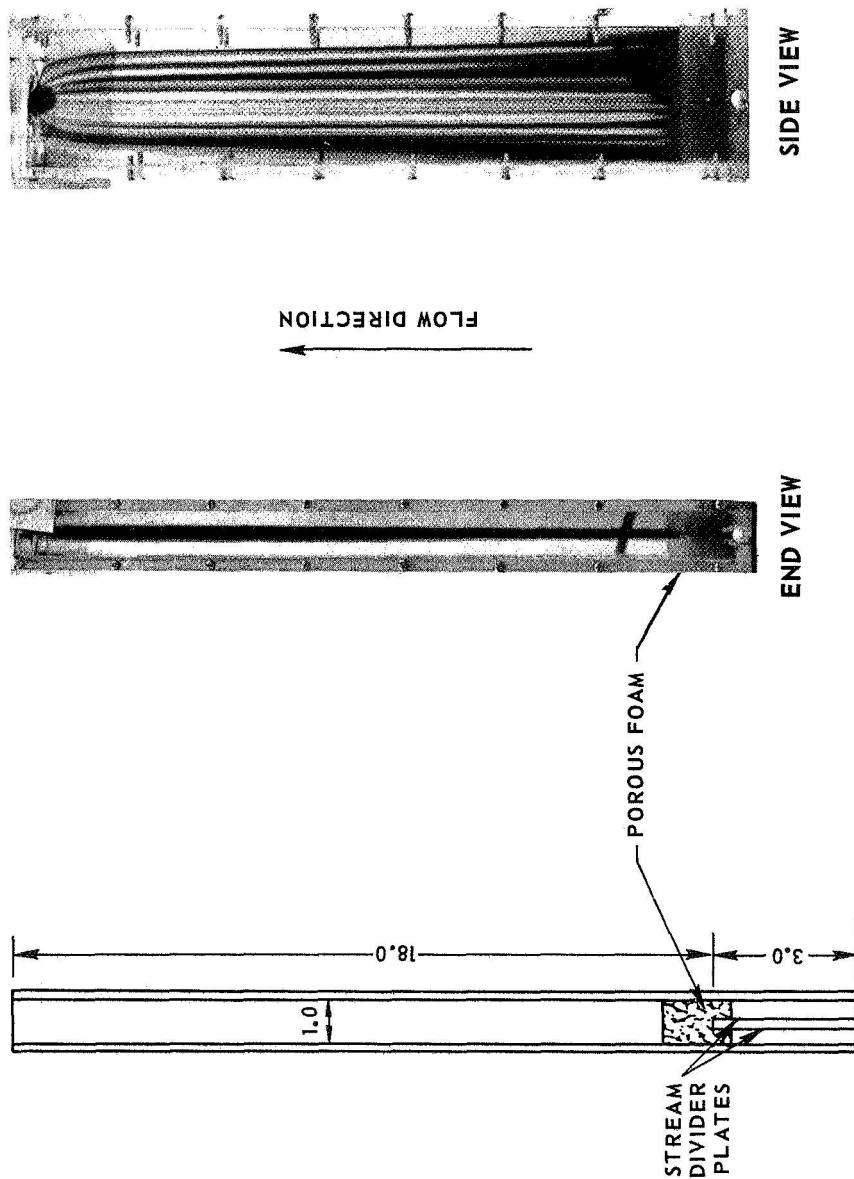
SKETCH OF TWO — DIMENSIONAL PROPELLANT DUCT
WITH CONVERGING INLET

ALL DIMENSIONS IN INCHES

(a) END VIEW

(b) SIDE VIEW

1.0

3.0

DETAIL OF DIVIDER PLATES

0.094

0.42   0.42

18.0

3.0

12.0

1.0—IN.—THICK
FOAM

WATER INLETS

4.5   1.0   4.5

FIG. 38

FLOW VISUALIZATION PHOTOGRAPHS OF TWO–DIMENSIONAL PROPELLANT DUCT AT DIFFERENT REYNOLDS NUMBERS

NO POROUS FOAM AT STREAM DIVIDER

WATER FLOW WITH CENTRAL STREAM COLORED WITH DYE

SEE FIG. 37 FOR DUCT DIMENSIONS AND CONVERGING INLET GEOMETRY
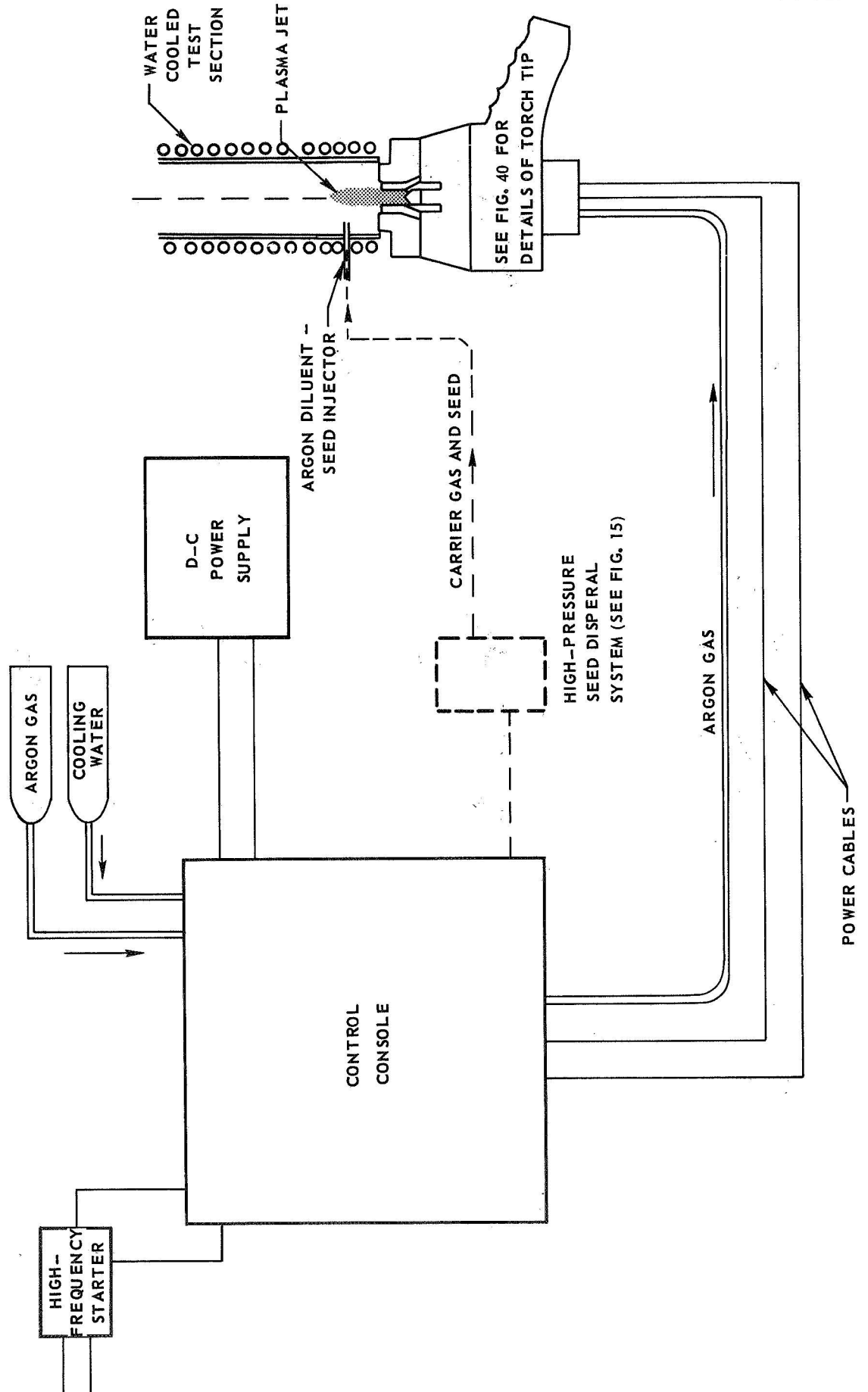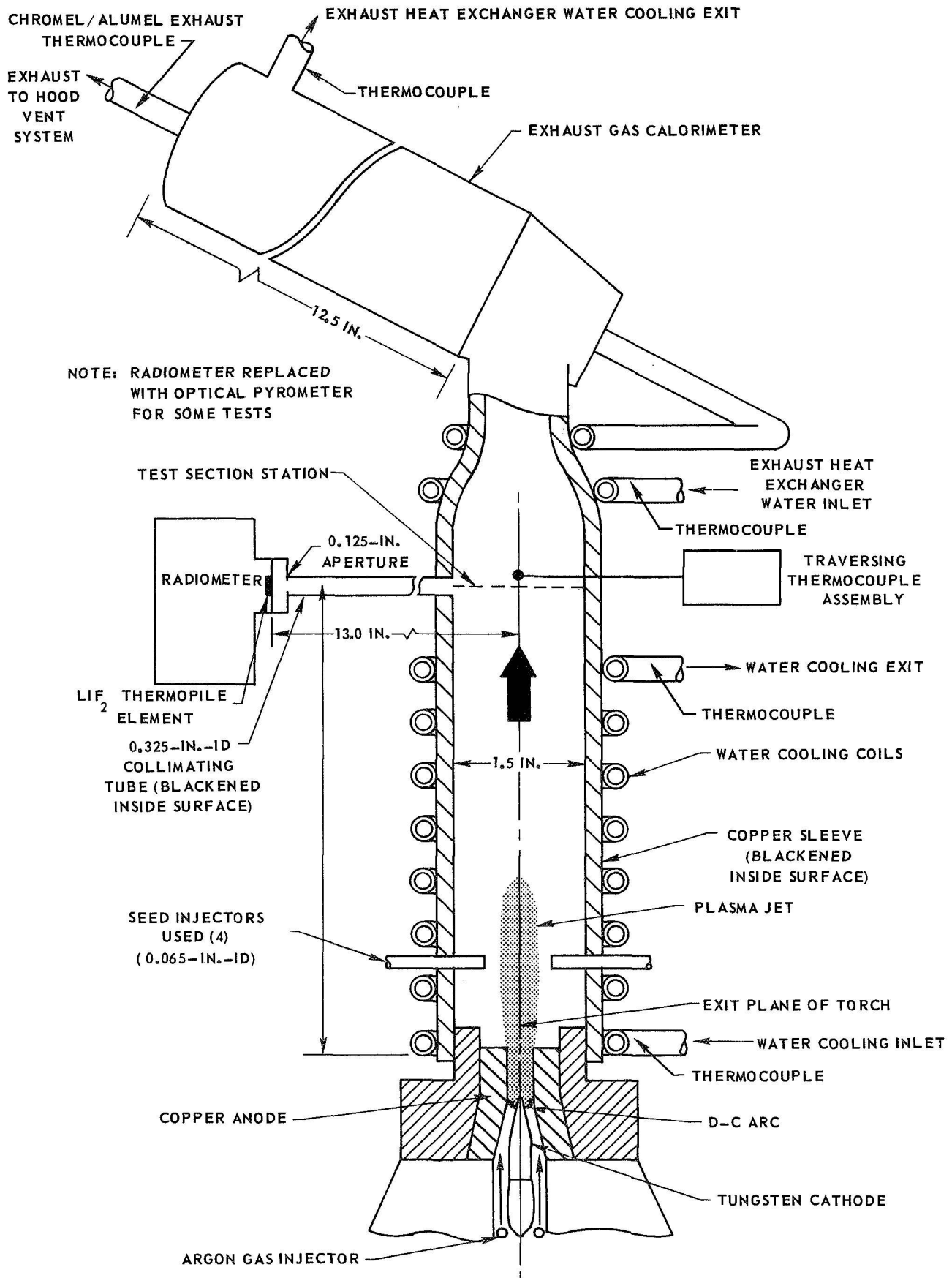

a) Re = 540

b) Re = 1350

c) Re = 1810

FLOW DIRECTION

SIDE VIEW   END VIEW   SIDE VIEW   END VIEW   SIDE VIEW   END VIEW

FIG. 39
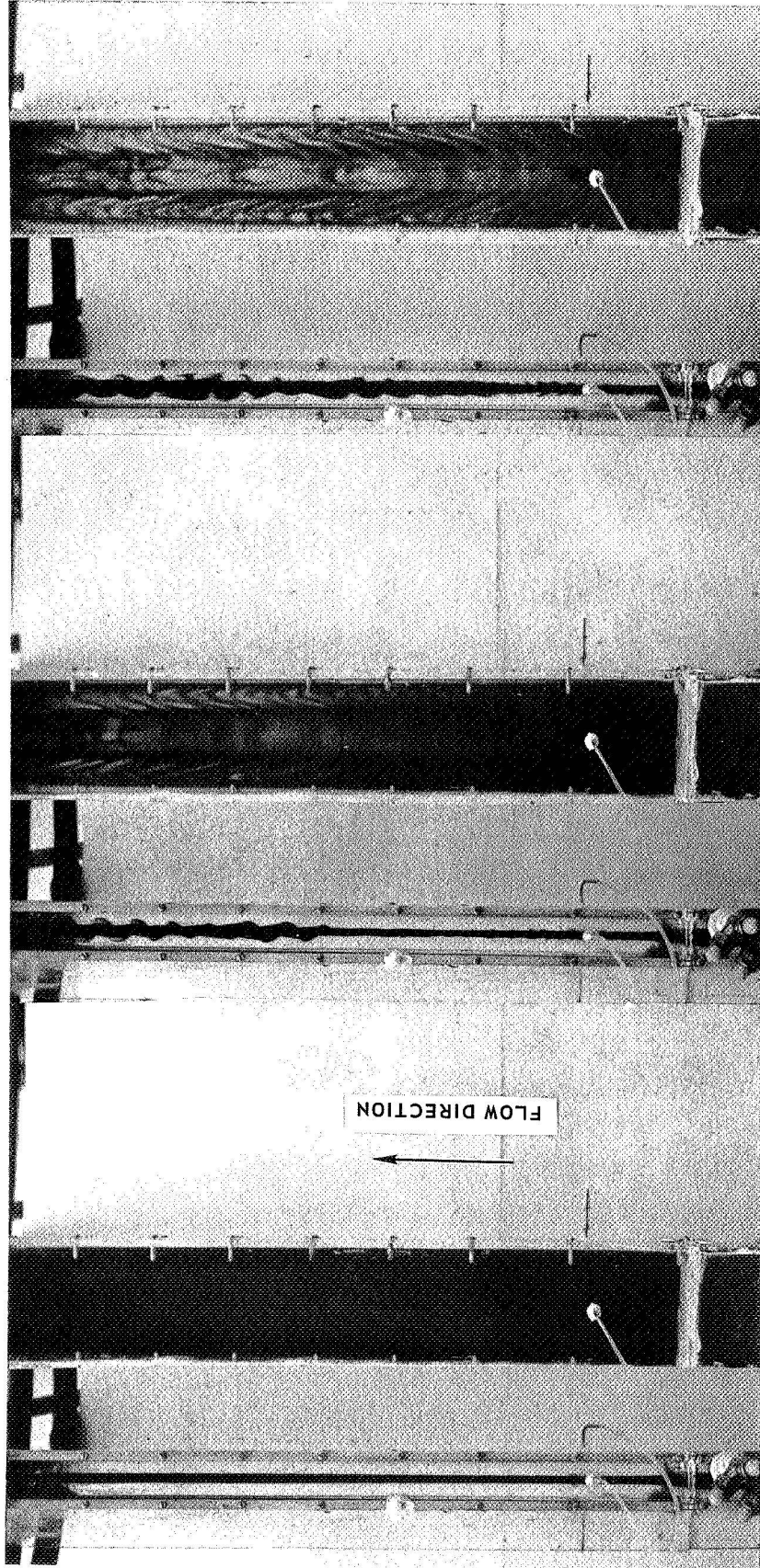
SCHEMATIC DIAGRAM OF PLASMA TORCH SYSTEM USED FOR SPECIAL INSTRUMENTATION TESTS

FIG. 40

SKETCH OF TORCH—CALORIMETER CONFIGURATION USED TO MEASURE TEMPERATURE AND RE—RADIATION AT TEST SECTION STATION

CHROMEL/ALUMEL EXHAUST THERMOCOUPLE

EXHAUST HEAT EXCHANGER WATER COOLING EXIT

EXHAUST TO HOOD VENT SYSTEM

THERMOCOUPLE

EXHAUST GAS CALORIMETER

12.5 IN.

NOTE: RADIOMETER REPLACED WITH OPTICAL PYROMETER FOR SOME TESTS

TEST SECTION STATION

EXHAUST HEAT EXCHANGER WATER INLET

THERMOCOUPLE

0.125—IN. APERTURE

RADIOMETER

TRAVERSING THERMOCOUPLE ASSEMBLY

13.0 IN.

WATER COOLING EXIT

THERMOCOUPLE

LIF$_2$ THERMOPILE ELEMENT

1.5 IN.

WATER COOLING COILS

0.325—IN.—ID COLLIMATING TUBE (BLACKENED INSIDE SURFACE)

COPPER SLEEVE (BLACKENED INSIDE SURFACE)

PLASMA JET

SEED INJECTORS USED (4) (0.065—IN.—ID)

EXIT PLANE OF TORCH

WATER COOLING INLET

THERMOCOUPLE

COPPER ANODE

D—C ARC

TUNGSTEN CATHODE

ARGON GAS INJECTOR

97

FIG. 41

ARGON GAS ENERGY CONTENT VERSUS CALCULATED BULK STREAM TEMPERATURE

PRESSURE = 1.0 ATM

SEE FIG. 40 FOR DETAILS OF TEST CONFIGURATION

TEST CHAMBER SEED INJECTORS AND DIAGNOSTIC PORTS AT
TEST SECTION STATION NOT PRESENT IN THESE TESTS

FIG. 42
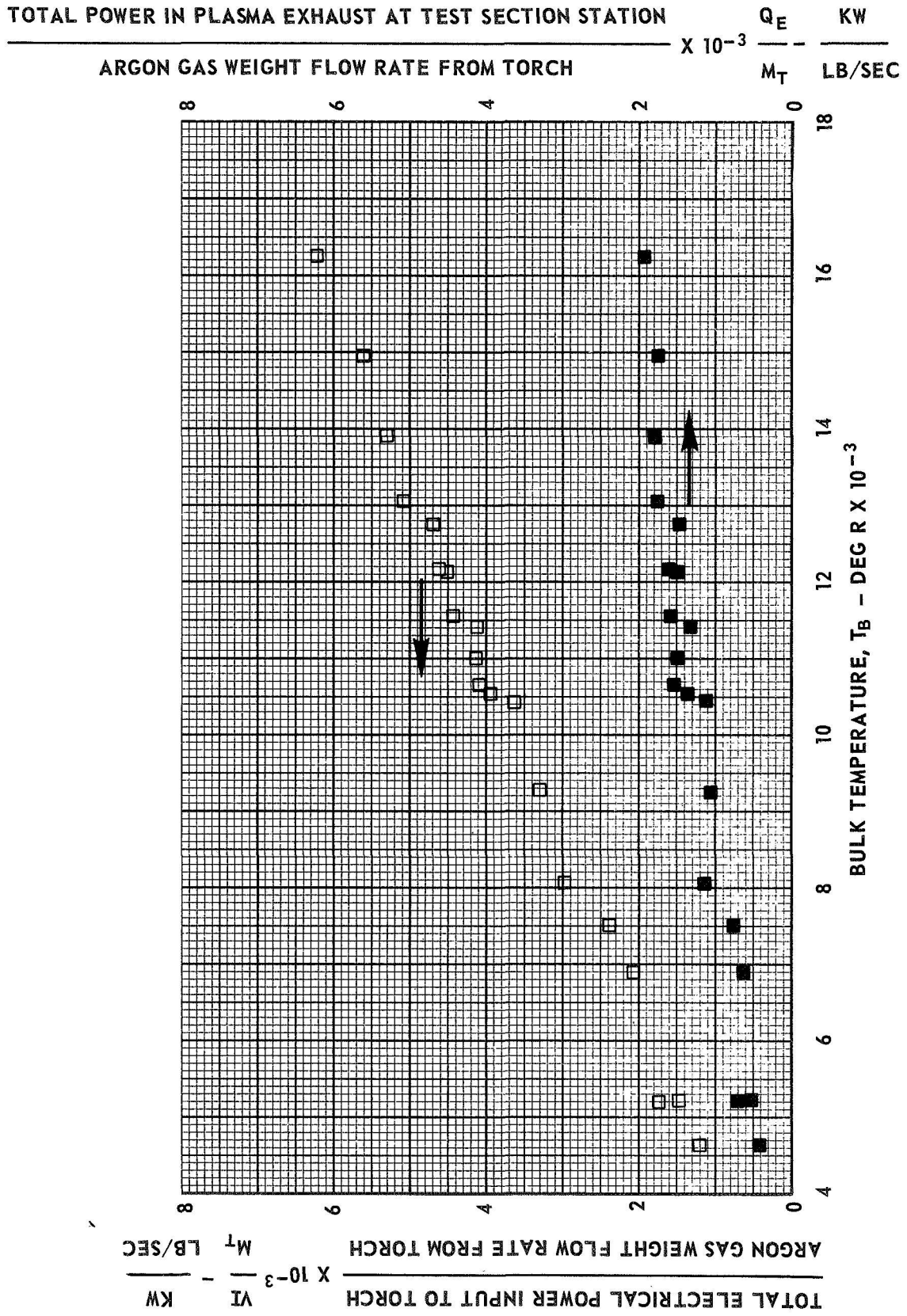
RESULTS OF THERMOCOUPLE LOCAL TEMPERATURE MEASUREMENTS, RERADIATION MEASUREMENTS AND OPTICAL PYROMETER MEASUREMENTS IN PLASMA JET TORCH TESTS WITH AND WITHOUT CARBON SEEDS

ARGON GAS – 1.0 ATM

SEE FIG. 40 FOR DETAILS OF TEST CONFIGURATION

ALL DATA SHOWN FOR CONDITIONS AT TEST SECTION STATION AND THE OPERATING CONDITIONS SHOWN BELOW

ARC CURRENT = 500A   ARC VOLTAGE = 29.5 V D-C

TOTAL BASE ARGON WEIGHT FLOW RATE = 2.65 X 10⁻³ LB/SEC

DILUENT–SEED CARRIER ARGON WEIGHT FLOW RATE = 6.2 X 10⁻³ LB/SEC

LIGHT CARBON SEED WEIGHT FLOW RATE = 0.8 X 10⁻³ LB/SEC (ESTIMATED)

HEAVY CARBON SEED WEIGHT FLOW RATE = 2.0 X 10⁻³ LB/SEC (ESTIMATED)

99

UNITED AIRCRAFT CORPORATION